Doctoral Dissertations   Dissertations and Theses

Fall November 2014

PRIMARY AND SECONDARY REACTIONS OF CELLULOSE MELT PYROLYSIS

Alex D. Paulsen
Chemical Engineering

Follow this and additional works at: https://scholarworks.umass.edu/dissertations_2

Part of the Catalysis and Reaction Engineering Commons

PRIMARY AND SECONDARY REACTIONS
OF CELLULOSE MELT PYROLYSIS

A Dissertation Presented

by

ALEX D. PAULSEN

Submitted to the Graduate School of the
University of Massachusetts Amherst in partial fulfillment
of the requirements for the degree of

DOCTOR OF PHILOSOPHY

September 2014

Department of Chemical Engineering

PRIMARY AND SECONDARY REACTIONS
OF CELLULOSE MELT PYROLYSIS

A Dissertation Presented

by

ALEX D. PAULSEN

Approved as to style and content by:

_____

Paul J. Dauenhauer, Chair

_____

Wei Fan, Member

_____

Scott M. Auerbach, Member

_____

T. J. Mountziaris, Department Head
Chemical Engineering

ACKNOWLEDGMENTS

ABSTRACT

PRIMARY AND SECONDARY REACTIONS OF CELLULOSE MELT PYROLYSIS

SEPTEMBER 2014

ALEX D. PAULSEN, B.A., UNIVERSITY OF MINNESOTA

Ph.D., UNIVERSITY OF MASSACHUSETTS AMHERST

Directed by: Professor Paul J. Dauenhauer

Fast pyrolysis of biomass is a next-generation biofuels production process that is capable of converting solid lignocellulosic materials (in their raw form) to a transportable liquid (bio-oil) which can be catalytically hydrogenated to fuels and chemicals. Pyrolysis reactors depolymerize solid biomass by heating the feedstock (in the absence of oxygen) up to high temperatures (400 – 600 °C) to produce a short-lived intermediate liquid phase (only a few seconds), which ultimately breaks down to form small (1-6 carbon) oxygenates. These vapor-products can then be condensed at room temperature to produce liquid bio-oil. While biomass fast pyrolysis has enormous potential to produce renewable fuels, an understanding of the fundamental chemistry and transport processes of biomass pyrolysis to produce bio-oil is not available in the literature.

This work utilizes co-pyrolysis and isotopic labeling to study the liquid-phase secondary reactions of levoglucosan to form anhydrosugars, pyrans, and light oxygenates. Isotopic labeling studies also reveal that hydrogen exchange is a critical component of levoglucosan deoxygenation. Next, the effects of pyrolysis reaction temperature and sample length scale are discussed. These studies revealed that the yield of total furan rings (i.e., all products containing a five-membered furan ring) does not change significantly with increased reaction temperature compared to other pyrolysis products, such as light oxygenates and anhydrosugars. However, the functional groups bound to the furan ring (e.g., alcohols and aldehydes) are easily cleaved to produce smaller furans. This chemistry was targeted by impregnating cellulose with palladium on

carbon to selectively decarbonylate oxygenated furans within liquid intermediate cellulose to form deoxygenated furans resulting in a more stable bio-oil.

The last part of this thesis, a new experimental technique, Spatiotemporally-Resolved Diffuse Reflectance in situ Spectroscopy of Particles (STR-DRiSP), which is capable of measuring biomass composition during fast pyrolysis with high spatial (ten micron) and temporal (one millisecond) resolution is developed. Compositional data were compared with a comprehensive two-dimensional single particle model. The STR-DRiSP technique can be used to determine the transport-limited kinetic parameters of biomass decomposition for a wide variety of biomass feedstocks.

TABLE OF CONTENTS

Page

LIST OF TABLES

LIST OF FIGURES

CHAPTER 1

INTRODUCTION

1.1 Global Energy Reserves and Consumption

Fossil fuels including oil, coal, and natural gas are the dominant forms of energy globally, accounting for approximately 95% of the world's energy consumption.[1] It is agreed upon that these sources of energy will eventually run out, whether this will take place within the next 50 years[2, 3] or much further in the future[1] will not change the ultimate outcome. Sooner or later fossil fuels will need to be replaced by alternative sources of energy. In addition to finite fossil fuel reserves, global energy consumption continues to increase. This increase is currently being driven by developing countries outside the Organization for Economic Cooperation and Development (OECD) as can be seen in figure 1.1.[4] This will stress the current energy supply chain and require either alternative sources of energy or an increase in supply. The effect of carbon dioxide produced from fossil fuels on global climate[5] and oceans[6, 7] has also increased the demand for clean and renewable fuels. However, making alternative sources of energy competitive with the existing fossil fuel supply chain will require significant investment in research and development and is a strong motivator for this thesis.
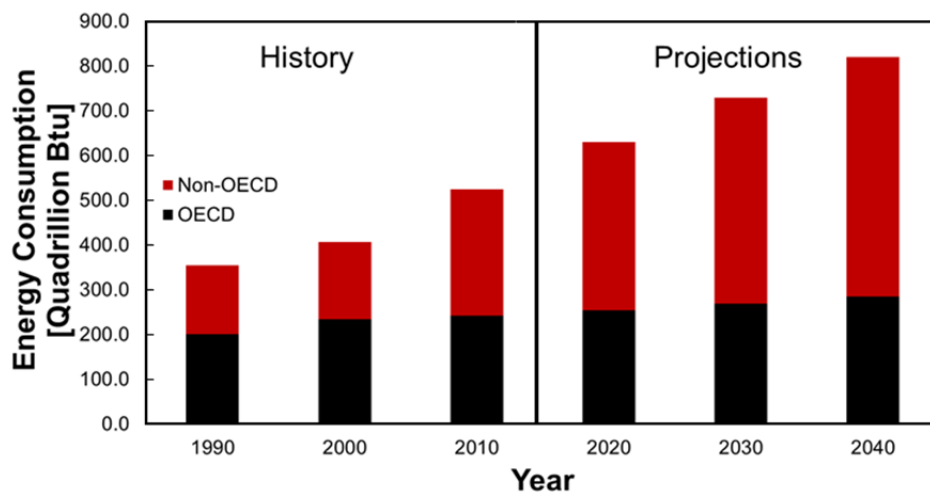
Figure 1.1Past, present, and predicted global energy consumption. Adapted from [4]

1.2 Renewable Energy for Transportation

The key for widespread renewable energy adoption is economic competitiveness with existing fossil fuels. In addition to cost, renewable fuels will have to match the distribution efficiency and fuel performance of fossil fuels, which includes fuel stability during transportation, easy accessibility for refueling purposes, and matching vehicle performance (horsepower, efficiency, etc…). The current transportation is entrenched in gasoline powered combustion engines. Potential alternatives to the current infrastructure include electric cars and hydrogen fuel cell which would each necessitate a major overhaul of the current transportation energy distribution network. Additionally, electrically powered vehicles are hindered by short operation ranges (200 miles) and long refueling times compared to internal combustion engines.[8] Hydrogen and electricity production would each require fossil fuels initially, but could eventually be produce via hydroelectric, nuclear, wind, solar, or geothermal sources. Each of these sources has environmental or social cost that limits viability. Hydroelectric power has nearly reached saturation and dramatically alters aquatic habitats, while nuclear power faces strong opposition over waste disposal.[1] Similarly wind, solar, and geothermal have their own environmental concerns, are limited to certain geographic locations (windy planes, sunny equator, volcanic regions), and are only active intermittently (which requires practical energy storage). These drawbacks make it desirable to maintain the current fueling infrastructure while replacing the fossil fuel source with equivalent renewable fuels (green gasoline).

Lignocellulosic biomass, including fast-growing trees and grasses, has been identified as major source of sustainable carbon capable of generating renewable fuels and chemicals.[9, 10] With over one billion dry tons of lignocellulosic biomass available in the United States,[11, 12] the U.S. Department of Energy has made it a goal to replace 30% of all transportation fuels with biofuels.[9]

Converting biomass to a useable liquid fuel to replace gasoline presents many difficulties; in particular, the high oxygen content of biomass in comparison to gasoline or diesel.

1.3 Enzymatic Biofuel Pathways

Biomass conversion to fuels has typically been dominated by the production of ethanol from the conversion of simple sugars via enzymatic pathways.[13] The most common source of ethanol fuel in the U.S. is from the conversion of corn, where the starch (~70% of the corn kernel) is converted to glucose which is fermented to ethanol.[13] Upwards of 10% of the corn crop produced in the U.S. is used to produce ethanol fuel.[13] However, ethanol production competes directly with human food supplies making it unlikely that corn-to-ethanol can ever replace transportation fossil fuel.[10, 14]

Cellulosic ethanol has more recently been proposed as a better source for ethanol conversion since it will not compete directly with the food supply.[10] However, cellulose is not directly fermentable by yeast and must be converted to glucose either through hydrolysis (using acids, peroxides and ammonia) or enzymatically (using cellulose)[15, 16] and this pretreatment process can be quite expensive.[10] Cellulosic ethanol also only utilizes part of the biomass as the lignin and hemicellulose content (≥40%) are considered byproducts during hydrolysis and are often burned for energy.[17]

Fermentation also typically requires long reaction times (days) which necessitates large reactors with high capital costs. Such high costs for building an economical ethanol plant limits the limits the widespread distribution of processing plants which could make biomass conversion more cost efficient (since solid biomass transportation costs are significant).[18] Despite the high selectivity of enzymatic derived biofuels the many barriers to economic production point to the need for processes with higher conversion and shorter reaction time. Thermocatalytic routes offer a way to overcome many of these challenges and may be a better option.

1.4 Thermochemical Biofuel Pathways

Thermochemical pathways have much shorter reaction time scales than enzymatic pathways. Thermochemical routes can also utilize energy contained in the non-edible portion (lignose and hemicellulose) of plants.[9, 10] There are three major thermochemical reactions used to convert biomass: combustion, gasification, and fast pyrolysis. Combustion utilizes high temperatures (800 – 1100 °C) to convert biomass to CO, CO_2, and H_2O.[19, 20] The heat generated is then converted to electricity to be used in the electric grid or stored. Biomass gasification operates at more moderate temperatures (500 – 1000 °C) to convert biomass to syngas (CO and H_2).[21-24] Syngas can then be upgraded via the Fischer-Tropsch process to produce methanol or transportation fuels.[25] Fast pyrolysis reactors operate at lower temperatures (400 – 600 °C) than combustion or gasification.[26-29] Fast pyrolysis also produces higher molecular weight products which can be used as heavy heating oils[30] or catalytically upgraded to produce transportation fuels.[31, 32]

Each of these technologies differs in regards to economics, logistics, and products. However, each pathway is initiated through condensed-phase pyrolysis chemistry where biomass breaks down to form C1 to C6 oxygenates. These products then vaporize under reaction conditions and are condensed in pyrolysis or oxidized to C1 species (CO and CO_2) in combustion/gasification. Therefore, it is important to understand the liquid-phase chemistry of pyrolysis in order to predict performance of combustion, gasification, or fast pyrolysis. The work in this thesis will consequently be applicable to combustion, gasification, or pyrolysis processes, but is motivated by the design of economical biomass fast pyrolysis reactors.

1.5 Biofuels via Fast Pyrolysis

Fast pyrolysis offers a promising route to convert lignocellulosic biomass to fuels and chemicals. [31, 33, 34] Some of the obstacles for solid biomass utilization is the high transportation costs,[31, 35-37] as well as the highly oxygenated nature of the feedstock.[31, 38] Fast pyrolysis of

biomass provides a solution to both issues since this process is capable of converting the raw feedstock to low molecular weight products (which are liquid at room temperature) that can be transported to central processing sites for catalytic upgrading to fuels and chemicals.[39-41] Pyrolysis reactors depolymerize solid biomass biopolymers (20,000 to 400,000 a.m.u.) by heating the feedstock (in the absence of oxygen) up to high temperatures (400 – 600 °C). This produces a short-lived intermediate liquid phase[42-44], which produces form small (1-6 carbon) oxygenates.[42, 44-49] These vapor-products can then be condensed at room temperature to produce liquid bio-oil. In order to maximize overall yield and selectivity to energy-dense products in pyrolysis reactors, a detailed understanding of the reactions that depolymerize solid biomass is needed.[28]

Despite the advantages of biomass pyrolysis, widespread adoption will depend on optimizing the process to meet high global demand for fuels and to compete economically with existing fossil fuels. At such large scales, any small change in yield or selectivity can greatly affect the process economics. Therefore optimizing reaction conditions to target deoxygenated species (furan, dimethylfuran) and eliminate acidic and reactive species (furfural, HMF) can improve pyrolysis economics. Target these goals will require knowledge of the fundamental reactions that take place within liquid intermediate cellulose, which is the goal of this thesis.

1.6 Thesis Objectives

The objective of this thesis is to probe the fundamental chemistries of biomass pyrolysis. By understanding these fundamentals, it will be possible in the future to develop predictive models for biomass pyrolysis which can be used to improve pyrolysis economics. Biomass is a complex feedstock made up of biopolymers (cellulose, hemicellulose, and lignin) and containing naturally occurring metal salts. This thesis begins by simplifying the feedstock by examining the chemistry of pure cellulose. Cellulose pyrolysis chemistry is further decoupled from transport limitations using thin-film pyrolysis, while primary and secondary reactions are decoupled using

co-pyrolysis and isotopic labeling studies. In addition to understanding the chemistry of cellulose pyrolysis, this thesis also uses heterogeneous catalysis to tune pyrolysis reactions to improve the properties of bio-oil. Finally, STR-DRiSP was developed to making compositional monitoring of biomass fast pyrolysis possible. Such a technique makes it possible to obtain highly precise fast pyrolysis data that can be used to improve the current models in the literature.

1.7 Thesis Approach

Several experimental techniques are used in this thesis to probe the chemistry of cellulose and biomass pyrolysis including: thin-film pyrolysis, co-pyrolysis, isotopic labeling, and catalyst-impregnated pyrolysis. These techniques were coupled with well-established experimental systems such as thermo-gravimetric analysis (TGA), gas chromatography mass spectroscopy (GCMS), liquid chromatography (LC), UV-vis diffuse reflectance spectroscopy, and scanning electron microscopy (SEM). A computational fluid dynamics (CFD) model was also used to provide insight.

1.8 Thesis Scope

Chapter two describes the transport limitations present in industrially relevant pyrolysis reactors. These limitations can be eliminated by using the thin-film pyrolysis technique in which a 3 – 10 micron film of cellulose is deposited in a crucible cup. By reducing the sample length scale by two to three orders of magnitude in comparison to powder pyrolysis (one millimeter), the reaction becomes kinetically-limited allowing study of the intrinsic pyrolysis kinetics.

Chapter three uses co-pyrolysis and isotopic labeling studies to examine the secondary reactions of levoglucosan within liquid intermediate cellulose. These techniques revealed that the levoglucosan breaks down to form pyrans, anhydrosugars, and light oxygenates. It was also shown that hydrogen plays a key role in these secondary reactions.

Chapter four examines the effect of temperature and length scale on the product distribution of cellulose pyrolysis. Thin-film pyrolysis is used to reveal the stability of 5-membered furan rings and the relative ease at which functional groups bonded to these rings are cleaved. Additionally, it is proposed that formaldehyde and CO are formed as co-products of the same mechanism and that formic acid is an intermediate in the formation of CO_2.

Chapter five demonstrates a possible way to improve bio-oil stability by impregnating cellulose with supported metal catalysts. Supported palladium catalysts are shown to be very effective at cleaving aldehyde groups to produce a partially deoxygenated bio-oil, while maintaining the overall bio-oil yield. By eliminating aldehyde groups in the final product, polymerization during storage and transportation is reduced, which makes the bio-oil more stable.

Chapter six develops a new analytical technique called Spatiotemporally-Resolved Diffuse Reflectance in situ Spectroscopy of Particles (STR-DRiSP). STR-DRiSP is capable of monitoring the carbohydrate content of a pyrolyzing biomass particle both spatially (10 μm) and temporally (1 ms). The technique is then validated with a robust wood fiber pyrolysis model.

Chapter seven summarizes the work presented in this thesis and discusses the future directions of pyrolysis research.

CHAPTER 2

TRANSPORT LIMITATIONS OF CELLULOSE PYROLYSIS

2.1 Introduction

Isothermal and well-mixed pyrolysis for the study of intrinsic pyrolysis chemistry at high temperatures (>400 °C) requires sample length scales two to three orders of magnitude smaller than millimeter-scale samples that have been utilized in the literature.[27, 32] In order to achieve isothermal conditions, a thin-film deposition technique was developed that produces a micron-scale film which allows for extremely high temperature changes (greater than 1,000,000 °C/min).[27] This temperature increase is much faster than previous pyrolysis techniques, such as powder pyrolysis (1000 °C/min) and thermogravimetric analysis (1-150 °C/min).[50] In addition to rapid heating of biomass samples, thin films also decrease the timescale of product diffusion (< 1 ms) through the intermediate liquid by two to four orders of magnitude relative to powder pyrolysis.[27]

2.2 Thin-Film Pyrolysis Length Scales

We determined the maximum temperature at which thin-film pyrolysis remains kinetically limited (i.e. temperature change is fast relative to pyrolysis reaction rates) by comparing pyrolysis reaction kinetics with conductive and convective heat transfer using the dimensionless Pyrolysis (Py) and Biot (Bi) numbers. Py^I is the ratio of reaction and conduction time scales, Py^{II} is the ratio of reaction and convection time scales, and Bi is the ratio of conduction and convection time scales.

$$Py^I = \frac{\lambda}{\rho C_p L^2 k} \tag{2.1}$$

$$Py^{II} = \frac{h}{\rho C_p L k} \tag{2.2}$$

$$Bi = \frac{hL}{\lambda} \tag{2.3}$$

Here we used the work of Dauenhauer et al.[42] and Papadikis and Bridgwater[51] to estimate a value of h (heat transfer coefficient between the hot surface and the biomass sample) of 2000 W m^{-2} K^{-1}, which is an intermediate value between the h calculated by Dauenhauer et al. (h = 10^4 – 10^5 W m^{-2} K^{-1}) using an ablative reactor and that calculated by Papadikis and Bridgwater (h = 500 W m^{-2} K^{-1}) using a fluidized bed reactor. The thermal conductivity, density, and heat capacity of cellulose are represented by λ, ρ, and C_p, respectively.[52] The characteristic length scale is represented with L, the heat transfer coefficient between the biomass sample and the ambient with h,[42, 51] and the reaction rate constant for cellulose pyrolysis with k.[53] However, it is important to note that since the reaction rate constant is taken from experiments below 370 °C (higher temperature values were unavailable) our calculations are approximate and not exact. Plotting the Pyrolysis numbers versus the Biot number for different temperatures in Figure 2.1 results in four unique pyrolysis zones: an isothermal and kinetically limited region (where the entire particle is one uniform temperature), a conduction-limited region, a convection-limited region, and a kinetically limited but non-isothermal region (where the particle reaches reaction temperature quickly, but does so with large temperature gradients throughout the particle).

By plotting different temperatures in Figure 2.1 (ranging from 350 – 750 °C in increments of 50 °C), we determined that the maximum temperature should not exceed 550 ° in order for pyrolysis of cellulose thin-films (3 μm) to remain isothermal and kinetically limited (i.e., region I). Interestingly, Figure 2.1 also reveals a stark contrast between thin-film (3 μm), in which thermal convection is much slower than conduction, and powder (780 μm) in which conduction is much slower than thermal convection.

9
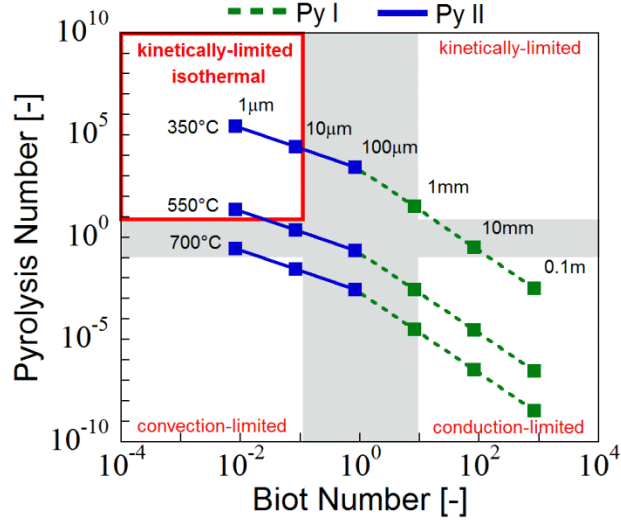
Figure 2.1 Reaction-transport map for cellulose pyrolysis. The Pyrolysis and Biot numbers (eqn 1-3) are used to compare heat transfer and reaction time scales for three furnace temperatures; 350, 550, and 700 °C. Four pyrolysis regimes are identified; isothermal and kinetically limited, kinetically limited, conduction limited, and convection limited.

To check the temperature ramping capabilities of our experimental setup (and confirm the conclusions from the aforementioned dimensionless analysis), we calculate the temperature throughout a cellulose thin-film and cellulose powder shown in Figure 2.2 by solving the one-dimensional heat transfer equation 2.4 with initial and boundary conditions (equations 2.5 –2.7).

$$\frac{\partial T}{\partial t} = \frac{\lambda}{\rho C_p}\left(\frac{\partial^2 T}{\partial x^2}\right) + \frac{R\Delta H_{rxn}}{\rho C_p} \tag{2.4}$$

$$T(x, t{=}0) = 25 \ °C \tag{2.5}$$

$$\frac{\partial T}{\partial x}(x{=}L, t) = \frac{h_a(T{-}T_a)}{\lambda} \tag{2.6}$$

$$\frac{\partial T}{\partial x}(x{=}0, t) = \frac{h_s(T{-}T_s)}{\lambda} \tag{2.7}$$

Here the heat transfer equation contains a transient term, a conduction term, and an energy generation term (from the heat of reaction). Physical properties for cellulose are taken from Di Blasi[52] (λ, C_P, ΔH_{rxn} and ρ), the reaction rates (R) are calculated from Bradbury et al.[54], and the heat transfer coefficient between the hot surface and the cellulose (h_s) is estimated to be 2000 W m^{-2} K^{-1} (as described in the dimensionless analysis above). The heat transfer coefficient between the cellulose and the gas-phase (h_a) is assumed to be 20 W m^{-2} K^{-1}, which is similar to previous values used in computational fluid dynamics simulations that account for convection across solid-gas interfaces in microscale systems.[55] The characteristic length of the thin-film sample is taken to be 3 μm (as evidenced by the SEM in Figure 2.3A) while the powder sample is treated as a closely packed mass of cellulose particles with a cumulative (i.e., sum of all particles in the powder stack) characteristic length of 780 μm (as observed in Figure 2.3F).

We see in Figure 2.2A that the cellulose thin-film heats up to near the reaction temperature of 550 °C within 5 milliseconds and that the temperature of the cellulose thin-film remains uniform throughout the thickness of the sample, confirming the findings of our dimensionless analysis that minimal thermal gradients exist in our thin-film cellulose sample (i.e., thin-film pyrolysis is isothermal). In contrast, the temperature profile of the 780 μm thick cellulose powder in Figure 2.2B shows that even after 5 seconds the sample is unable to attain the 550 °C reaction temperature and remains non-isothermal throughout the 5 second reaction time, despite the fact that the same sample parameters are used (i.e., physical properties, heat transfer coefficients, transport parameters). The powder sample does not reach the temperature of the reactor wall due to the heat transfer barrier at the wall-sample interface (which is quantified by the non-zero heat transfer coefficient). Additionally, significant temperature gradients are present across (x-direction) the powder sample, since heat cannot be transported across the biomass sample before it is transferred to the ambient. These thermal profiles show that conventional powder pyrolysis experiments are not isothermal and that this technique cannot be used to perform kinetically-limited experiments.
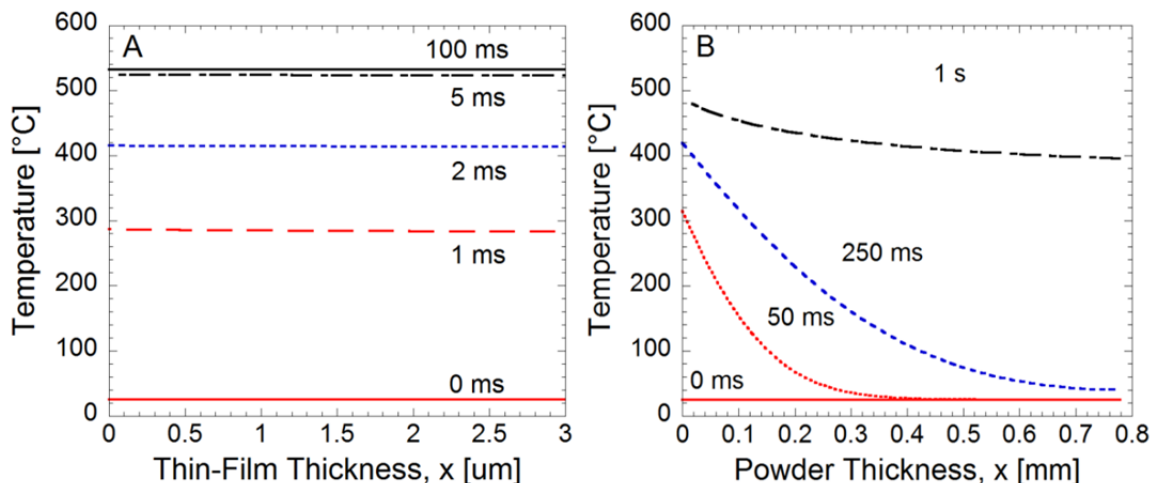
Figure 2.2 Transient temperature profiles for cellulose thin-film and powder pyrolysis with surface temperatures of 550 °C. One dimensional MATLAB simulations indicate that the cellulose thin-film is heated up to reaction temperature in approximately 5 milliseconds isothermally (A) while the cellulose powder has not reached reaction temperature after 1 second and is non-isothermal (B). In these calculations an intermediate heat transfer coefficient is assumed (2000 W/m^2-K). Cellulose physical properties are taken from previous work,[52] the thin-film thickness is assumed to be 3 μm as determined via SEM imaging (Figure 2.3A), and powder thickness is assumed to be 780 μm as determined via photography (Figure 2.3F).

2.3 Thin-Film and Powder Preparation.

Powder samples were prepared by depositing 1 to 2 mg of microcrystalline cellulose directly into the crucible using a five point balance. Thin-film samples were prepared by first suspending microcrystalline cellulose powder (purchased from Alfa Aesar; Part Number: A17730) in water. Then 25 μL of the suspension (1 wt% cellulose) was transferred to a 4 mm x 8 mm (diameter x height) cylindrical pyrolysis crucible. The water was removed by evaporation at room temperature under 25 in Hg vacuum leaving behind a micron-scale film of cellulose on the inner wall of the crucible. In order to confirm the micron-scale nature of this cellulose thin-film, scanning electron microscope (SEM) imagery was utilized. The SEM image in Figure 2.3A shows the thickness of the cellulose thin-film to be approximately 3 μm (which places it within the kinetically limited regime). In contrast to the thin-film, powder samples (Figure 2.3C-D) have sample dimensions (290 – 780 μm) that fall outside of the kinetically limited regime. Despite using powder loadings (240 μg) similar to the thin-film loading (250 μg), the powder sample is

still unable to achieve the length scales (10 μm) necessary for kinetically limited experiments (Figure 2.3C). This is because powder samples stack at the base of the cup, while the thin-film sample is able to coat the inside of the cup and thus cover a larger surface area.
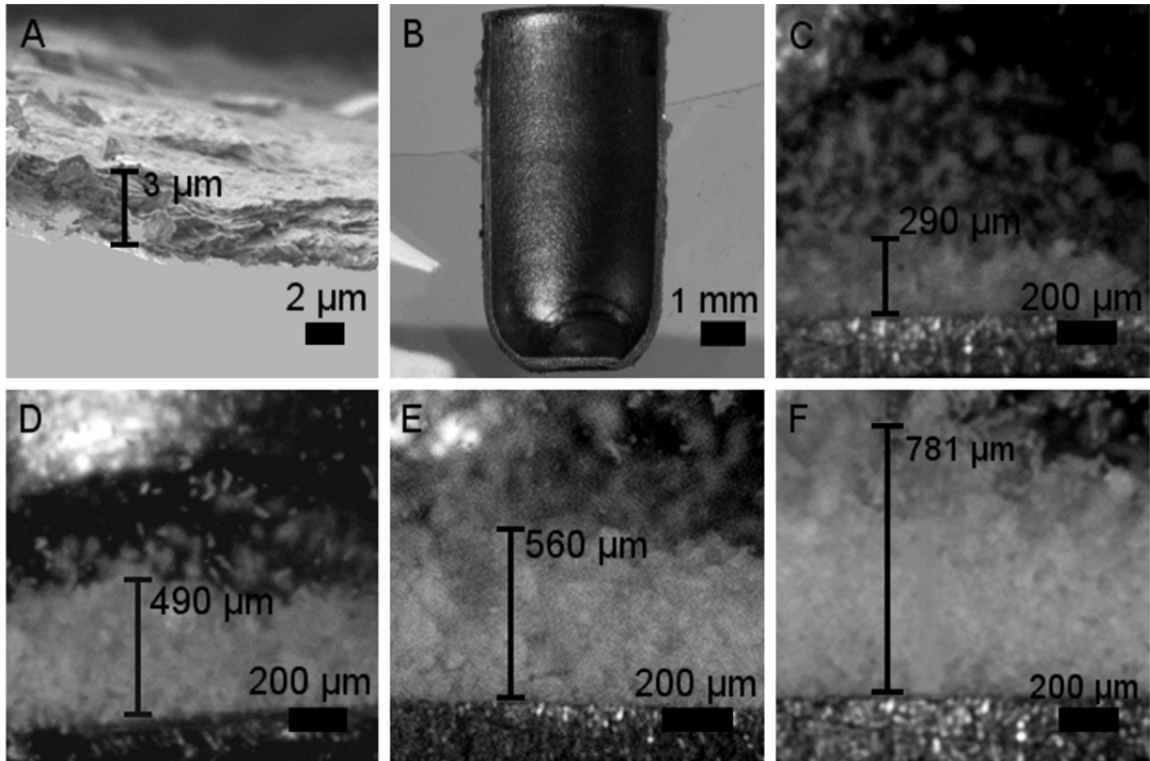
Figure 2.3 Sample Loading Dimensions. (A) SEM image of a 250 μg cellulose thin film, (B) Empty pyrolysis crucible, (C) photograph of a 240 μg sample loading, (D) photograph of a 460 μg sample loading, (E) photograph of a 1020 μg sample loading, and (F) photograph of a 1540 μg sample loading.

CHAPTER 3

SECONDARY REACTIONS WITHIN LIQUID INTERMEDIATE CELLULOSE

3.1 Introduction

Despite the advantages of pyrolysis technology, broad industrial adoption hinges on process optimization because of the massive production scale required to meet fuel demand (global gasoline consumption is more than 1 billion gallons per day).[56] For such large scale processes, small changes in yield or selectivity can have a significant impact on the overall economics. In biomass pyrolysis, optimized operating conditions could promote specific reactions which convert highly oxygenated compounds, such as levoglucosan (LGA), to more energy dense products, such as pyrans or furans.[27, 48, 53, 57-60] To achieve this, molecular-level mechanisms capable of predicting reaction rates over a range of operating conditions are necessary but are currently lacking.

Developing detailed models for pyrolysis is challenging because of the complexity of the high temperature chemistry. Previous efforts to construct predictive models have focused on global kinetic expressions that lump products and intermediates according to phase and molecular weight (e.g., vapors, permanent gases, char).[53, 54, 61, 62] While these models can describe macroscopic phenomena, such as biomass volatilization rate, they are unable to make molecular-level predictions which could ultimately be used to tune the product distribution in real world reactors. Additionally, these models cannot describe the multiphase nature of pyrolysis where solid biomass decomposes through an intermediate liquid.[42-44] More recently, we have used experimentally-guided first principles simulations to show how primary pyrolysis products, such as furans and light oxygenates, form from cellulose.[27] While this approach identifies primary reactions, an equally important endeavor is to understand how these initial products break down to form secondary products which are major constituents of bio-oil.

Secondary pyrolysis is the thermal decomposition of primary volatiles, such as LGA (60% yield from cellulose), which can occur in the gas-phase[63] or within the short-lived intermediate liquid forming during pyrolysis.[64, 65] Secondary reactions have been postulated to be responsible for converting major cellulose pyrolysis products, such as LGA, to furans, light oxygenates, char and permanent gases.[50] In agreement with previous work,[32] we have found that LGA does not break down when pyrolyzed alone (no co-reactants). This indicates that LGA is relatively stable and may be an end point on the pyrolysis reaction network. Here, we assess LGA stability within molten biomass using co-pyrolysis experiments.

3.2 Secondary Reactions of Levoglucosan

In our co-pyrolysis technique, the LGA and fructose (FCT) powder and thin-film mixtures are co-pyrolyzed in a flash pyrolysis reactor (at 500 °C) to produce volatile products and char.[27] FCT was selected as the co-reactant to simulate the intermediate liquid environment for several reasons: simple sugars have been found to pyrolyze through an intermediate liquid similar to cellulose;[43] FCT has a similar elemental composition (e.g., C/O ratio) and functional groups (e.g., hydroxyl groups) to cellulose (implying that liquid-phase intermediates have a similar effect on secondary reactions); FCT does not generate LGA during pyrolysis which facilitates product quantification; and FCT is structurally similar to reactive intermediates identified in our previous work in the pathway to furan formation.[27] Co-pyrolysis experiments were conducted by pyrolyzing either mixtures of fine LGA and FCT powders or micrometer thick thin-films (see supporting information for details). The initial composition in co-pyrolysis experiments is defined by the LGA ratio (R_{LGA}).

$$R_{LGA} = \frac{m_{LGA}}{m_{LGA} + m_{FCT}} \tag{3.1}$$

In equation 3.2, m_{LGA} and m_{FCT} are the initial masses of LGA and FCT, respectively. Three categories of co-pyrolysis products are formed (Table 1): FCT-derived (permanent gases, char,

light oxygenates, furans), LGA-derived (i.e., LGA only), and a number of interaction species

(caused by secondary reactions).

Table 3.1 Single component and co-pyrolysis products. List of all compounds (26, including char) identified in powder pyrolysis experiments and their yield (in percent of initial carbon). The yield ratio (γ) is shown for co-pyrolysis experiments (for a mixture of 50/50 levoglucosan/fructose). Average values are shown for thin-film pyrolysis at 500 °C with 90% mean confidence intervals.

Compound	Fructose only			Fructose / Levoglucosan 50 / 50			γ [-]	Levoglucosan only		
	Yield [%C]			Yield [%C]				Yield [%C]		
Anhydrosugars										
Levoglucosan	0	±	-	39.0	±	5	0.8	101	±	4
1,6 anhydroglucofuranose*	0	±	-	1.0	±	0.1	∞	0	±	-
dianhydroglucopyranose*	0	±	-	0.6	±	0.1	∞	0	±	-
Pyrans										
ADGH*	0	±	-	0.8	±	0.09	∞	0	±	-
DHDHMP*	1.1	±	0.08	0.7	±	0.1	1.2	<0.1	±	<0.01
DHMP*	0.2	±	0.02	0.9	±	0.06	7.6	0	±	-
Furans										
hydroxymethylfurfural	19	±	2	8.0	±	1	0.8	0	±	-
Furfural	10	±	0.5	3.4	±	0.6	0.6	0.1	±	0.01
5-methyl furfural	0.9	±	0.2	0.6	±	0.3	1.2	0	±	-
2-furanmethanol	0.3	±	0.05	0.4	±	0.01	2.0	0	±	-
2,5 dimethyl Furan	0.5	±	0.06	0.5	±	0.1	1.7	0	±	-
2-methyl furan	0.5	±	0.06	0.3	±	0.06	1.1	<0.1	±	<0.01
Furan	0.3	±	0.02	0.2	±	0.04	1.6	<0.1	±	<0.01
DMHF*	0.5	±	0.05	0.5	±	0.06	2.2	0.1	±	<0.01
Light Oxygenates										
methyl glyoxal	3.8	±	0.5	3.9	±	0.4	2.0	0.6	±	0.01
glycolaldehyde	2.6	±	0.06	2.4	±	0.2	2.8	0	±	-
formaldehyde	0.8	±	0.2	0.3	±	0.03	0.7	<0.1	±	0.02
hydroxyacetone	0.6	±	0.09	0.9	±	0.09	2.9	0.2	±	0.08
acetic acid	0.8	±	0.1	0.7	±	0.09	1.8	0	±	-
2,3 butanedione	0.2	±	0.03	0.3	±	0.02	2.2	<0.1	±	0.01
glyoxal	0.2	±	0.04	0.2	±	0.04	1.7	0.1	±	0.02
Permanent Gases										
carbon monoxide	1.5	±	0.2	0.9	±	0.1	1.1	0.2	±	<0.01
carbon dioxide	3.3	±	0.6	2.2	±	0.3	1.2	0.4	±	0.03
Other										
HMCP*	<0.1	±	0.01	0.1	±	0.01	2.7	<0.1	±	0.01
1,2-cyclopentanedione*	0.3	±	0.04	0.2	±	0.06	1.7	<0.1	±	<0.01
char	24	±	2	12.0	±	0.3	-	0	±	-
Total	72	±	1	82	±	4	-	103	±	4

* Confirmed by mass spectra only; pure standard unavailable. Abbreviations: ADGH – 1,5-anhydro-4-deoxy-D-glycero-hex-1-en-3-ulose [48]; DHDHMP – 2,3-dihydro-3,5-dihydroxy-6-methyl-4H-pyran-4-one; DHMP – 3,5-dihydroxy-2-methyl-4H-pyran-4-one; DMHF – 2,5-dimethyl-4-hydroxy-3(2H)-furanone, HMCP –2-hydroxy-3-methyl-2-cyclopenten-1-one.

Secondary break down of LGA, as well as formation of secondary products, was

quantified during thin-film and powder co-pyrolysis experiments using the yield ratio γ_i.

$$\gamma_i = \frac{Y_{CoPy}^i}{x_{LGA} Y_{LGA}^i + x_{FCT} Y_{FCT}^i} \tag{3.2}$$

In equation 3.2, Y_{CoPy} is the experimental co-pyrolysis yield (from either thin-film or powder experiments) while Y^i_{LGA} and Y^i_{FCT} are the yields from single component pyrolysis of LGA and FCT, respectively. x_{LGA} and x_{FCT} are the initial mole fractions. The yield ratio quantifies the effect of co-pyrolysis on the yield of individual products. A γ_i value of 1 for product i indicates that its production is not affected by co-pyrolysis while values less or greater than 1 depict product inhibition or promotion, respectively.

Figure 3.1A shows that for powder experiments, LGA does not break down when pyrolyzed alone ($R_{LGA}=1$ but does break down over a range of LGA mixture ratios ($R_{LGA}=0.25$-0.75). To determine if secondary pyrolysis of LGA is affected by residence time within the intermediate liquid, thin-film co-pyrolysis experiments were conducted where microscale samples enable several orders of magnitude faster mass transport compared to powder co-pyrolysis (see supporting information for details).[27] Figure 3.1A shows that in contrast to powder co-pyrolysis (squares), LGA does not break down in the thin-film (circles). This indicates that LGA can evaporate faster than it reacts within the thin-film intermediate liquid, and the extent of secondary LGA reactions can be controlled by varying small sample length scales.
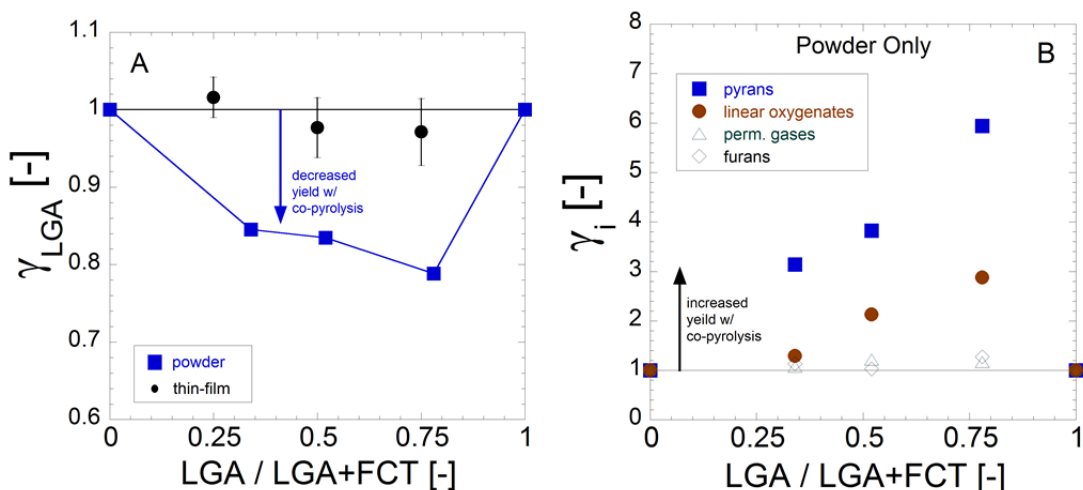
Figure 3.1 Yield ratio for products of co-pyrolysis vs. mixture composition. Levoglucosan (LGA) and fructose (FCT) are co-pyrolyzed in order to evaluate L breakdown to form secondary products within the intermediate liquid. In (A), the effect of residence time in the intermediate liquid is evaluated by comparing L breakdown in powder and thin-film co-pyrolysis. In (B), interaction products produced in powder co-pyrolysis are quantified using the yield ratio (γ_i) defined in (2). The reaction temperature was 500 °C. Error bars indicate 90% confidence intervals. LGA / LGA+FCT is equivalent to R_{LGA} in (1).

Co-pyrolysis experiments were conducted with powder and thin-film mixtures of levoglucosan and fructose to reveal secondary pyrolysis pathways. Powder co-pyrolysis samples were prepared by weighing 0.5-1 mg of levoglucosan and fructose and then mixing them within a cylindrical pyrolysis crucible. Thin-films were prepared by co-precipitating levoglucosan and fructose from aqueous solutions. Figure 3.2 shows that levoglucosan and fructose thin-films form in the same region of the pyrolysis crucible. Co-pyrolysis samples (powder and thin-film) were pyrolyzed in the Frontier 2020 Micropyrolyzer at 500 °C (typical pyrolysis reaction temperature).[27, 32, 66] Volatile products were then swept out of the micropyrolyzer furnace and into an Agilent 7890 GCMS which is kept at sub-ambient temperatures to inhibit product degradation. The multidimensional GCMS was then used to identify and quantify 26 products (including char and permanent gases such as CO and CO_2). Char residue was quantified by injecting oxygen into the micropyrolyzer furnace and quantifying the resulting CO and CO_2.
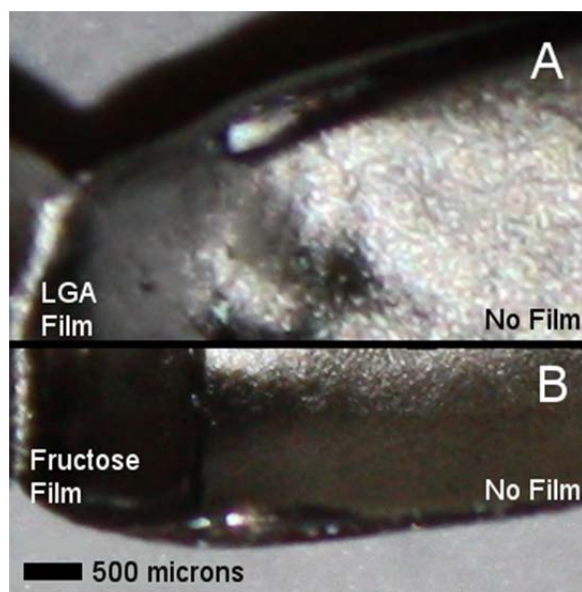
Figure 3.2 Photos of levoglucosan (A) and fructose (B) thin-films within the pyrolysis crucible. Areas with no reflection indicate the presence of a thin-film (far left) while regions with light reflectance indicate no thin-film (far right).

Figure 3.1B shows that specific types of products are promoted in powder co-pyrolysis. Pyrans can increase by a factor of six during co-pyrolysis while the yield of light oxygenates increases up to three-fold (see Table 1 for details). Such high yield ratios for both pyrans and light oxygenates at intermediate LGA ratios (R_{LGA}=0.25-0.75) reveal that LGA degradation is correlated with an increase of these products. On the other hand, the yield of furans and permanent gases are relatively unchanged by co-pyrolysis. The increase in pyrans is interesting since these compounds retain all carbon-carbon bonds and have higher energy value (via reduced oxygen content), i.e., pyrans are more suitable for biofuels. Figure 3.3 shows (partial) chromatograms from FCT-only pyrolysis, LGA-only pyrolysis, co-pyrolysis (FCT and LGA) and cellulose pyrolysis. These chromatograms reveal that four six-carbon products (DHMP, ADGH, DAGP and AGF) are generated during co-pyrolysis and do not appear in either FCT-only or LGA-only pyrolysis. Additionally, a comparison of the co-pyrolysis and cellulose chromatograms reveals that these six-carbon products are also generated in cellulose pyrolysis. These results

indicate that secondary pyrolysis is likely abundant in conventional (i.e., powder) pyrolysis

reactors.
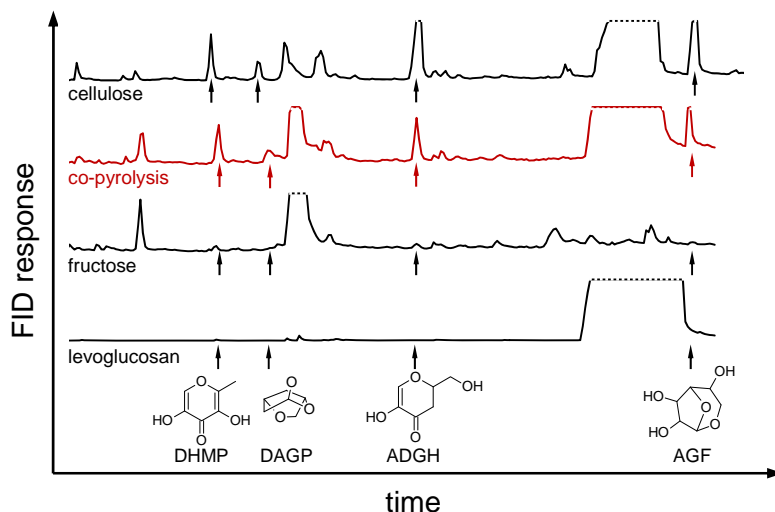
Figure 3.3 New products in powder co-pyrolysis. Levoglucosan-only, fructose-only, co-pyrolysis (50/50 wt. levoglucosan/fructose mixture), and cellulose powder pyrolysis gas chromatograms are shown. To illustrate the four new products produced during co-pyrolysis, only the pyran/anhydrosugar regions of the chromatogram are shown. The reaction temperature was 500 °C.

3.3 Carbon-13 Labeling Studies

To confirm that secondary six-carbon products are produced from LGA (and not FCT), co-pyrolysis experiments were repeated using ^{13}C-labeled FCT (all six carbons) and unlabeled (^{12}C) LGA.[67-69] Figure 3.4A shows that all four secondary products (DHMP, DAGP, ADGH and AGF) are derived almost entirely from LGA (rather than FCT). It is important to note that although we focus on the effect of co-pyrolysis on LGA break down, there is also a minor effect on FCT pyrolysis chemistry. Different from LGA, no new FCT-derived products are observed during co-pyrolysis and product distributions for FCT-derived products change only slightly.
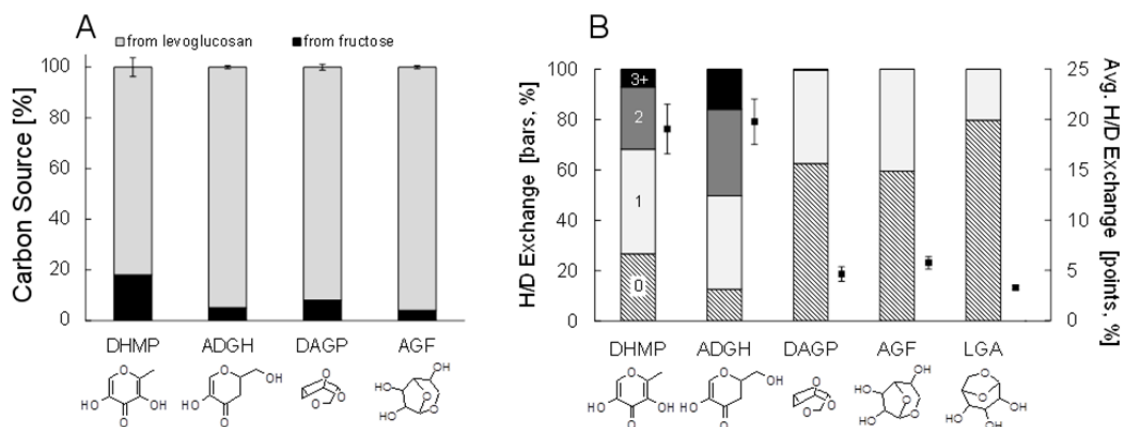
Figure 3.4 Isotopic co-pyrolysis. Co-pyrolysis experiments with powder mixtures of levoglucosan and C13-labeled fructose (A), and levoglucosan and deuterated (all 12 positions) glucose (B). In (A), the percentage of each product (on a carbon basis) that originates from levoglucosan (gray) and C13-labeled fructose (black) is shown. In (B), the percent of each product with 0, 1, 2, or 3+ hydrogens exchanged with deuterated glucose is shown. Points in (B) show the average percent hydrogens exchanged (average number of hydrogens exchanged divided by total number of hydrogens in the molecule) for each product. The reaction temperature was 500 °C. Error bars indicate 90% confidence intervals.

Figure 3.4A of the main paper uses C[13]-labeled fructose in conjunction with mass spectrometry to identify the origin of carbon atoms within several products. C[13]-labeled fructose was obtained from Cambridge Isotope Laboratory with ≥ 98% chemical purity (CP) and 99% isotopic purity (IP) and was used as received.

In order to quantify signals from the mass spectrometer (MS), individual peaks representing a given mass-to-charge ratio (m/z) are benchmarked against the sum of all peaks within the parent ion region (PIR),[67-69] which is illustrated from the raw mass spectra shown in Figure 3.5. PIR is defined by the molecular weight of the selected product, which is confirmed by comparing analyte and pure standard retention times.
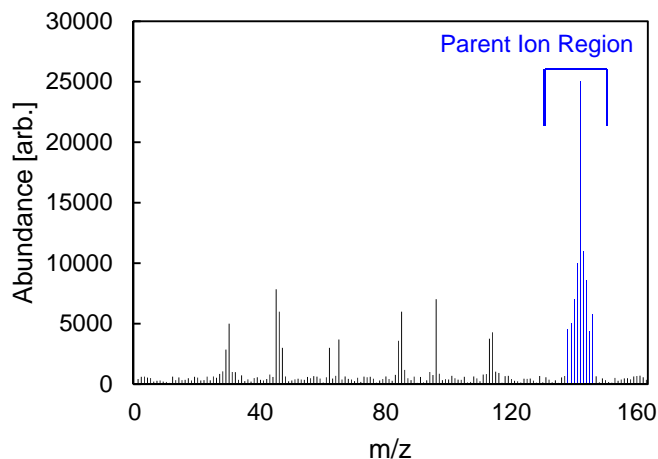
Figure 3.5 Example mass spectrum. The parent ion region (PIR) is highlighted in blue.

In the C^{13}-labeled fructose experiments, C^{13}-fructose was co-pyrolyzed with unlabeled (UL) levoglucosan. Products generated from co-pyrolysis are either fully labeled (all carbons C^{13}) or fully unlabeled (all carbons C^{12}). It is possible that carbon scrambling could occur (where a given product has some C^{12} and C^{13}), but in our experiments this is not observed. In order to determine the fraction of a single product that is labeled (with C^{13}), the relationship given in Paine et al is used.[68]

$$x = \frac{I_m + S_m}{S_{m,0} - S_m}$$ (3.3)

Where the parameters in (3) are defined as:

x = the mass fraction of the isotopically labeled (with C^{13}) portion of the analyte

m = the molecular weight of the labeled (C^{13}) analyte

m,0 = the molecular weight of the unlabeled analyte

I_m = the normalized intensity of peak m from the labeled/unlabeled mixture

S_m = the normalized intensity of peak m (all carbons C^{13}) from unlabeled reference

$S_{m,0}$ = the normalized intensity of peak m,0 (all carbons C^{12}) from unlabeled reference

3.4 Deuterium Labeling Studies

To investigate the LGA decomposition mechanism, co-pyrolysis experiments were repeated with deuterated glucose (all 12 positions) and unlabeled LGA to determine if hydrogen exchange plays a role in decomposition of the anhydrosugar. The mass spectra of four all six-carbon products were then analyzed and the number of hydrogens/deuteriums (H/D) exchanged was calculated to compare LGA deoxygenation and H/D exchange rates (see supporting section for details). Figure 3.4B reveals that DHMP and ADGH show significant H/D exchange. Additionally, data points in Figure 3.4B show that on average about 20% of hydrogens are exchanged in these products (compared to <4% for unreacted LGA) while the two anhydrosugars products (DAGP and AGF) exhibit relatively little H/D exchange (4 and 6%, respectively). Our findings indicate that H/D exchange plays an important role in elimination reactions but not in all deoxygenation processes (e.g., cyclization of LGA to form DAGP or AGF). Additional co-pyrolysis experiments indicate that both pyrans (ADGH and DHMP) exhibit H/D exchange for partially deuterated glucose (D7; all C-H bonds modified to C-D but O-H unchanged) albeit not to the same extent as for co-pyrolysis with fully deuterated (D12) sugars (Figure 3.6). This result shows that that both carbon-bound (C-H) and oxygen-bound (O-H) hydrogens participate in H/D exchange. Co-pyrolysis experiments with deuterated glucose reveal that extramolecular hydrogen exchange (through free protons, free radicals or Brønsted acids) is involved in LGA deoxygenation via elimination.
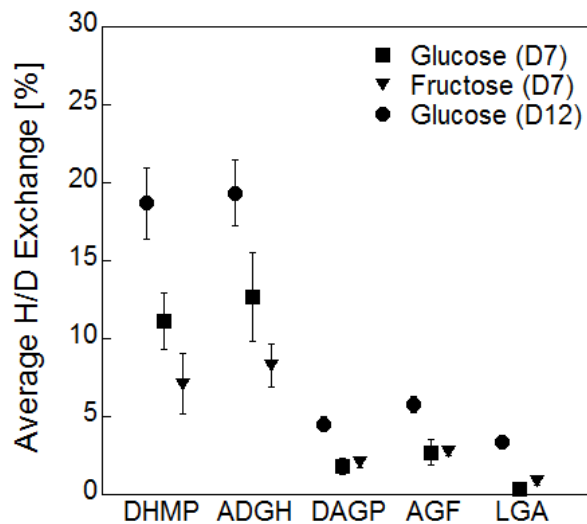
Figure 3.6 Average hydrogen exchange of co-pyrolyzed products. Levoglucosan powder was co-pyrolyzed with glucose (D7, all C-H replaced with C-D), glucose (D12, all C-H and O-H replaced C-D and O-D), and fructose (D7, all C-H replaced with C-D). The average percentage of hydrogen atoms exchanged for deuterium atoms is calculated for five products of co-pyrolysis. The reaction temperature was 500 °C. Error bars indicate 90% confidence intervals.

Figure 3.7 shows how these secondary pyrolysis pathways can be integrated into a cellulose pyrolysis mechanism. After the solid-liquid phase transformation, depolymerized cellulose oligomers breakdown to form furan, light oxygenates, char, permanent gases and LGA. LGA can then volatilize to the gas-phase or undergo condensed-phase secondary pyrolysis chemistry to form pyrans and light oxygenates.
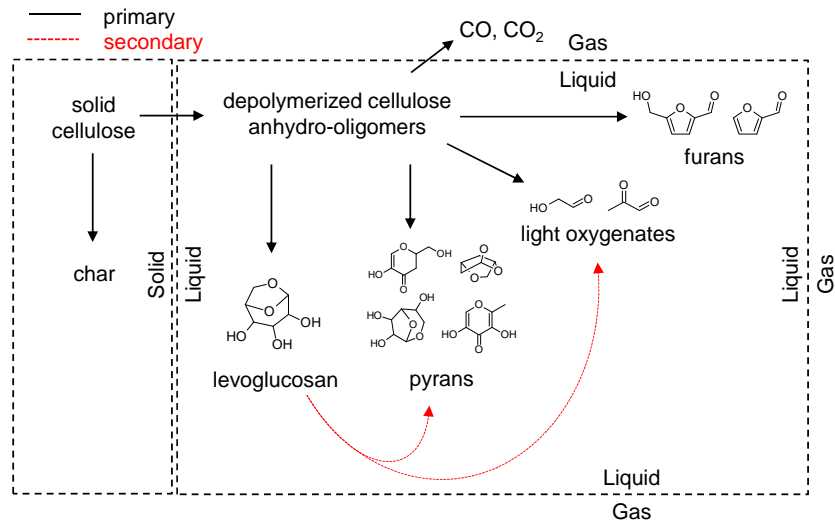
Figure 3.7 Primary and secondary pathways in cellulose pyrolysis. Secondary pathways (identified in this work) are shown for levoglucosan conversion to pyrans and light oxygenates.

Hydrogen exchange experiments were conducted with labeled glucose (D12 or D7) or labeled fructose (D12) and unlabeled levoglucosan. Deuterated fructose (D7, C-H positions only) was obtained from Omicron Biochemicals with CP=99.9% and IP=98%; deuterated glucose (D7, C-H positions only) was obtained from Cambridge Isotope laboratory at CP≥98% and IP=98%; and deuterated glucose (D12, C-H and O-H positions) was obtained from Isotec at CP=99% and IP=97%. During co-pyrolysis, products of interest are produced by both labeled glucose and levoglucosan pyrolysis. For a given analyte, various isotopes exist which are unlabeled (all hydrogens with molecular weight of one), fully deuterated, or partially deuterated. This results in a spectrum of isotopes with multiple peaks in the mass spectrum of the parent ion region (PIR), as can be seen in Figure 3.8D. A single MS peak m/z=i at a given m/z has contributions not only from the isotope with m/z=i, but also from nearby isotopes (m/z≠i) which also fragment to generate peaks at m/z=i. Contributions to isotope i from nearby isotopes (with m/z≠i) must be subtracted out to get the actual amount of isotope i for a given analyte.

The parent ion in a given mass spectra is encompassed by smaller ions as seen in Figure 3.8A-B. Upon examination of Figure 3.8C, we see significant peaks between the deuterated (MW=107) and unlabeled (MW=104, true MW of this analyte) primary ions. In order to

determine the percentage of this analyte that is deuterated, we first collect spectra for analytes

produced from separate (single component) pyrolysis of unlabeled and labeled (D12) glucose

pyrolysis (Figure 3.8A-B). During co-pyrolysis, single component pyrolysis spectra will

contribute to the overall co-pyrolysis spectra. To determine the amount of hydrogen exchange in

a co-pyrolysis run, the interactive effects (hydrogen exchange) must be separated from spectra

produced from single component pyrolysis (non-interacting). In order to subtract single

component effects from the co-pyrolysis spectra, we first average the two single component

spectra. We use a weighted average based on the product yield from deuterated and unlabeled

glucose pyrolysis. If this is done with the example spectra for the case where deuterated and

unlabeled glucose generate the same yield of a given analyte, we obtain the Spectra shown in

Figure 3.8C. The averaged spectrum (defined in the equation below) is used as a reference to

analyze hydrogen exchange in co-pyrolysis of deuterated glucose and unlabeled levoglucosan.

$$C4 = \frac{A4 + B4}{2}$$

(3.4)

Figure 3.8D shows that several shifted ions form in the parent ion region during isotopic

co-pyrolysis. In Figure 3.8E, a hypothetical spectrum for "non-interacting" co-pyrolysis is shown.

This spectrum shows that when no hydrogen exchange occurs, the average (of single component)

spectrum illustrated in Figure 3.8C is generated. Returning to Figure 3.8D, this spectrum needs to

be amended to subtract out contributions to this spectrum from the labeled sample (we want to

only study hydrogen exchange in the labeled sample). We must also account for the effects of

small ions surrounding the primary ion. In Figure 3.8A, we see two small peaks (A3 and A5)

next to the primary ion A4. An analogous spectrum is produced for the labeled sample shown in

Figure 3.8B. This will be true for any shift of the parent ion. The minor peaks must then be

subtracted from each isotope in Figure 3.8D-E to produce an "adjusted spectra", shown in Figure

3.8F-G. This analysis is described using the following equation:

$$S_m^{act} = S_m - \sum_{i=0}^{n} S_{m+i} \frac{S'_{m-i+i}}{S'_{m,0}}$$

(3.5)

Where,

S_m^{act} = the adjusted normalized intensity of peak m

S_m = the normalized intensity of peak m from the co-pyrolysis spectrum

S_{m+i} = the normalized intensity of peak m+i from the co-pyrolysis spectrum

S'_{m-i+1} = the normalized intensity of peak m-i+1 from the averaged reference spectrum

$S'_{m,0}$ = the normalized intensity of the primary ion peak from the averaged reference spectrum

i = runs from zero to the total number of hydrogens in the compound

The relative intensity of peak F5 is calculated from the co-pyrolysis spectrum given in Figure 3.8D in the following way:

$$F5 = D5 - D4\frac{C4}{C4} - D6\frac{C3}{C4} - D7\frac{C2}{C4}$$

(3.6)

Or

$$0.23 = 0.25 - 0.45\frac{0.02}{0.46} - 0.02\frac{0.02}{0.46} - 0.15\frac{0.00}{0.46}$$

(3.7)

The above analysis is repeated for every isotope in the spectrum (i.e., peaks: m, m+1, m+2, etc.). The final adjusted peaks are then used to determine the percent of labeling (or deuteration). To perform this calculation, peaks F4 and F5 in Figure 3.8F are normalized by the sum of all labeled peaks, where X is the percent of the analyte that is 1x deuterated.

$$X = 100\% \left(\frac{F5}{F4 + F5 + F6 + F7} \right)$$

(3.8)
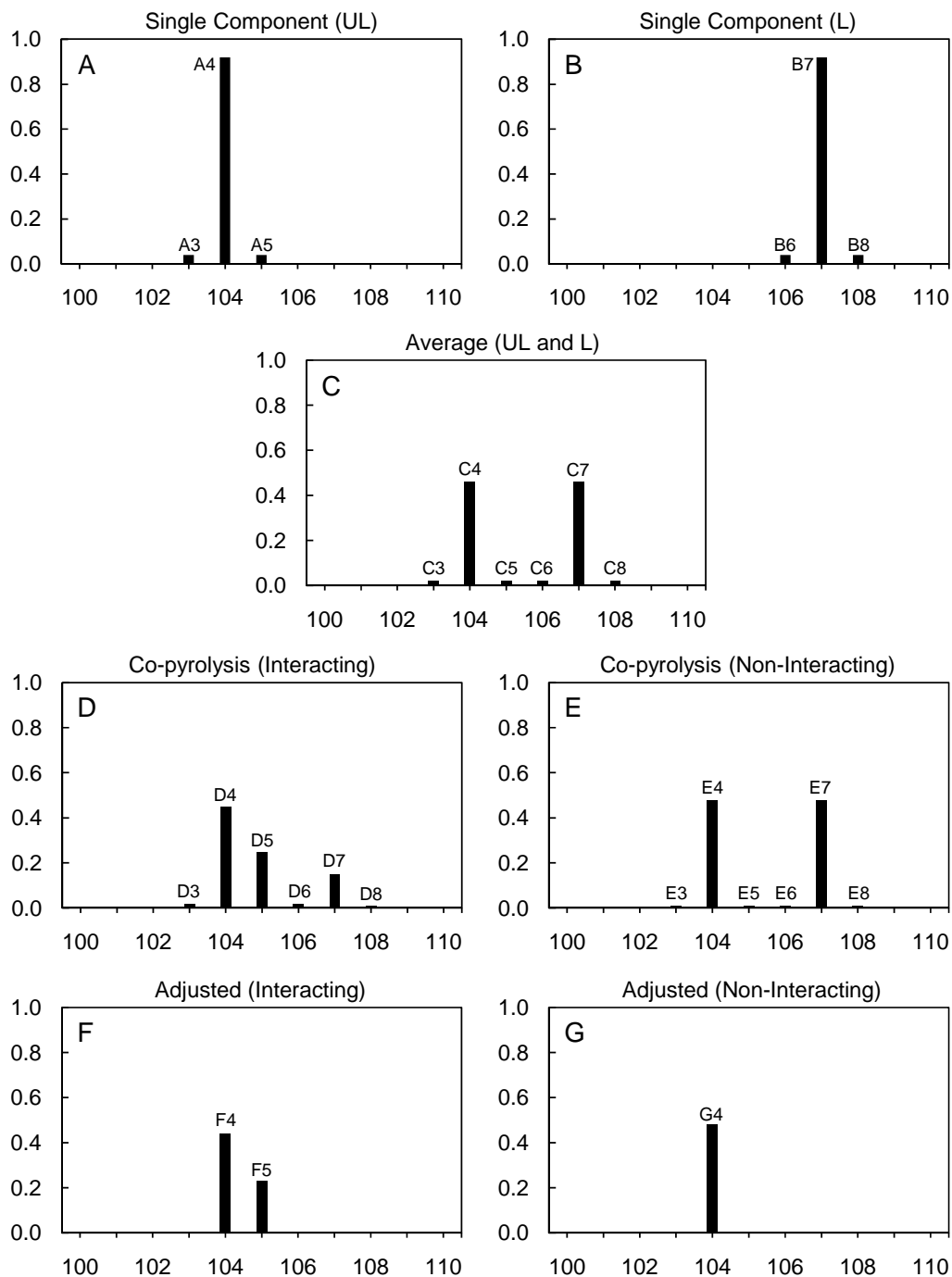
Figure 3.8 Methodology for calculating hydrogen exchange (interacting) between deuterated (L) glucose and unlabeled (UL) levoglucosan. For all plots (A-G), y-axis is the relative response and the x-axis the mass over charge ratio (m/z). Peak labeles run from A1 to A8 starting with m/z = 101 and ending with m/z = 108. The mass spectra portray an imaginary compound with 3 Hydrogens and a molecular weight of 104.

3.5 Conclusions

In summary, our work utilizes novel co-pyrolysis experiments with isotopically-labeled biomass-derived compounds to show for the first time that LGA can react within the intermediate liquid through elimination and cyclization chemistry. Furthermore, these secondary products have also been observed in cellulose pyrolysis and have higher energy contents than the LGA precursor. Finally, secondary reactions within the condensed phase facilitate biomass deoxygenation during pyrolysis, while retaining carbon-carbon bonds, and generate a bio oil product more suitable for upgrade to transportation fuels. These reaction pathways provide fundamental understanding of fast pyrolysis and make a significant step forward in developing detailed mechanisms for optimizing pyrolysis reactors in biorefineries.

CHAPTER 4

TEMPERATURE AND LENGTH SCALE EFFECTS ON CELLULOSE PYROLYSIS

4.1 Introduction

Lignocellulosic biomass consists primarily of three components: cellulose, hemicellulose, and lignin. These biomass building blocks possess significant oxygen functionality making fundamental understanding of the underlying chemical processes difficult. Due to the complexity of biomass structure and chemistry, empirical models describing the decomposition of lignocellulosic biomass are largely oversimplified and apparatus-specific.[53, 54, 61, 62, 70-73] In an effort to simplify the reacting system, prior work has focused on cellulose since it is the most abundant and least complex of the three major components of biomass. Previous efforts investigating cellulose pyrolysis have identified and quantified products as well as developed lumped kinetic models.[26, 27, 32, 50, 66, 70, 74-82] The most commonly cited lumped model for cellulose is the Broido-Shafizadeh mechanism[54, 61], which postulates the depolymerization of cellulose to an undescribed 'active cellulose' intermediate which in turn is further converted to vapors (bio-oil) or char and gases via competing pathways. In the Broido-Shafizadeh mechanism, researchers utilize thermogravimetric analysis (TGA) to empirically determine experimental rate constants. This technique, while able to accurately predict mass volatilization rates for cellulose, employs low temperature ramps (typically in the range of $1 - 150\ °C/min$), which are too slow to heat solid biomass up to pyrolysis reaction temperatures (400-600 °C) before it reacts.[27] The shortcomings of this experimental technique inhibit the collection of molecular-level information and result in the adoption of lumped kinetic models that are conditions specific. In such simple kinetic description, the chemistry of the reactants (lignocellulose), intermediates, and products are grouped by phase; i.e., vapors, gases and char. The lack of detailed descriptions of molecular

level processes in biomass pyrolysis imposes a barrier to reactor optimization and commercial adoption of the technology.

In an effort to provide fundamental descriptions of pyrolysis chemistries, we recently combined isothermal pyrolysis with first principles simulations to produce the first molecular-level insights into the formation of the 5-membered furan ring and light oxygenates directly from cellulose.[27] Additionally, we have revealed the effect of chain length in cellulose pyrolysis[74] as well as shown that secondary reactions within the intermediate liquid convert levoglucosan (the most abundant cellulose pyrolysis product) to pyrans and anhydrosugars.[83] In the present work, we reveal insights into the formation and stability of the 5-membered furan ring. We also reveal the significant effect of transport limitations on product yields in cellulose pyrolysis where larger powder samples have different product yields (e.g., higher levoglucosan) compared to thin-films. Additionally, we show the effect of reaction temperature on product yields for thin-film pyrolysis and thereby construct a library of kinetically-limited, isothermal data for use in developing molecular-level kinetic models.

4.2 The Effect of Temperature on Thin-Film Pyrolysis of Cellulose

The yields of cellulose thin-film pyrolysis products at five temperatures ranging from 350 °C to 550 °C are summarized in Table 4.1. In Figure 4.1A we show the effect of pyrolysis temperature on the yield of bio-oil and several classes of products. Bio-oil yield increases from 61% at 350 °C to nearly 80% at 450 °C before decreasing to 70% at 550 °C. Figure 4.1B shows the carbon-to-oxygen ratio (C/O) of bio-oil, which quantifies the energy content of fuels, does not change with temperature in cellulose pyrolysis (true for both powder and thin-film pyrolysis). However, the average carbon number of bio-oil decreases with increased reaction temperature, which is true for both powder and thin-film pyrolysis.

Table 4.1 Compounds (28) identified in cellulose thin-film pyrolysis experimentsa

Compound (Yield, %C)	350 °C	400 °C	450 °C	500 °C[b]	550 °C
Anhydrosugars					
levoglucosan	28	29	30	27	22
1,6 anhydroglucofuranose*	2.0	1.9	1.5	1.4	1.00
Levoglucosenone	0.89	0.31	0.25	0.46	0.13
dianhydroglucopyranose*	2.2	2.0	2.0	2.2	1.3
Pyrans					
ADGH*	2.5	2.5	2.2	3.2	1.5
DHMDHP*	0.80	0.68	0.71	0.50	0.55
Furans					
hydroxymethylfurfural	4.5	4.3	4.2	3.7	3.3
furfural	1.6	1.6	1.7	1.6	1.6
5-methyl furfural	0.48	0.49	0.56	0.75	0.58
2-furanmethanol	1.4	0.75	0.70	0.62	0.51
2,5 dimethyl furan	0.36	0.44	0.64	0.78	0.68
2-methyl furan	0.28	0.37	0.41	0.33	0.37
furan	0.085	0.31	0.46	0.29	0.53
furanone, 2(5H)	0.78	0.70	0.85	0.56	0.83
Light Oxygenates					
methyl glyoxal	3.2	4.6	6.2	6.7	6.8
glycolaldehyde	4.2	6.9	8.2	7.9	6.7
formaldehyde	0.0	1.1	4.8	2.6	6.0
hydroxyacetone	2.3	2.1	2.0	2.6	2.0
acetic acid	0.51	0.34	0.53	0.56	0.54
2,3 butanedione	0.24	0.50	0.75	0.76	0.90
formic acid	3.7	4.4	7.0	10.2	8.6
glyoxal	0.000	1.5	2.2	1.2	2.4
Permanent Gases					
carbon dioxide	1.3	3.3	3.9	3.4	4.9
carbon monoxide	0.63	2.1	3.0	3.1	5.1
Other					
CPHM*	0.14	0.19	0.26	0.27	0.25
1,2-cyclopentanedione*	0.60	0.51	0.67	0.59	0.69
catechol	0.53	0.59	0.76	0.33	0.70
char	20	16	13	12	10
Total	83	89	99	96	90

[a] Approximate yields (in percent of initial carbon) are presented for five pyrolysis temperatures. Error is presented as a 90% mean confidence interval. [b] Yields reported in previous work. * Confirmed by mass spectra only; pure standard unavailable. Abbreviations: ADGH, 1,5-anhydro-4-deoxy-D-glycero-hex-1-en-3-ulose; DHMDHP, 2,3-dihydro-3,5-dihydroxy-6-methyl-4H-Pyran-4-one; CPHM, 2-hydroxy-3-methyl-2-cyclopenten-1-one

Yields of individual cellulose thin-film pyrolysis products are presented in Figure 4.2A-F as a function of pyrolysis temperature. Levoglucosan (LGA), dianhydroglucopyranose (DAGP), and 1,6 anhydroglucofuranose (AGF) yields at different temperatures are shown in Figure 4.2A.

The yield of LGA (the most abundant cellulose pyrolysis product) remains relatively constant at 29% from 350 °C to 500 °C, but then decreases at 550 °C to 22%. This decrease in LGA is concomitant with a decrease in total anhydrosugar yield (Figure 4.1A). Yields of both DAGP and AGF decrease consistently (by approximately 1 percentage point over the whole temperature range) as the reaction temperature is increased. The yield of five individual furans and the yield of total furan rings are plotted in Figure 4.2B-C. The yields of hydroxymethylfurfural (HMF) (the most abundant furan) and furan methanol decrease as reaction temperature increases. In contrast, furfural (the second most abundant furan) remains at a constant yield as temperature increases, while the yields of deoxygenated furans (furan and dimethyl furan) increase with reaction temperature and the yield of total furan rings remains constant. Light oxygenates, permanent gas, and char yields are shown in Figure 4.2D-F. Light oxygenates yields generally increase as the reaction temperature increases, which includes the most abundant light oxygenate products formic acid, formaldehyde, glycolaldehyde, and methyl glyoxal. Hydroxyacetone (Figure 4.2D) is an exception to this increase in product yield with its yield remaining constant at approximately 2.3%. The yield of permanent gas products, CO and CO_2, both increase from 1% at 350 °C to 5% 550 °C. Differing from permanent gases and light oxygenates, char yields decrease from 20% at 350 °C to 10% at 550 °C.

4.3 Effect of Sample Dimension: Thin-Film versus Powder Pyrolysis

Figure 4.3A-D compares product yields between thin-film (isothermal) and powder (transport-limited) pyrolysis for four selected products: levoglucosan (LGA), anhydroglucofuranose (AGF), hydroxymethylfurfural (HMF), and methyl glyoxal. Over the temperature ranges investigated here, HMF is the only product (of the four in Figure 4.3) that produces statistically-equal amounts between thin-film and powder pyrolysis. In contrast, LGA and AGF are more abundant in powder experiments while the lower molecular weight product, methyl glyoxal, is more prevalent in thin-film experiments.

33

Temperature dependence of LGA and AGF differs between thin-film and powder pyrolysis; in powder pyrolysis, LGA and AGF yields remain constant over the temperature range investigated here (i.e., 400-600 °C), whereas a reduction in LGA and AGF is observed at higher temperatures (i.e., 550 $^{\circ}$C) in thin-film experiments. HMF does not change in a statistically meaningful way for both thin-film and powder experiments, which is at least partially due to the large experimental error for this product (which in turn is due to difficulties in quantifying this product because of its reactivity). Finally, both thin-film and powder experiments exhibited greater yields of methyl glyoxal with increasing reaction temperature (Figure 4.3D).

4.4 The Effect of Temperature on Bio-oil Yield and Quality

One broad performance metric for pyrolysis processes is bio-oil yield per unit feedstock. Previous work in the literature has shown that the maximum bio-oil yield occurs between 400 and 550 °C, depending on biomass type and size.[84-86] Specific to cellulose pyrolysis, Hoekstra et al. found the maximum bio-oil yield to be 84% at 450 °C,[84] which is similar to our work that shows maximum bio-oil yield (79%) at 450 °C. In addition to the yield of bio-oil, quality is also a concern. Our work shows that the average carbon number of bio-oil decreases (Figure 4.1B) from five carbon atoms (350 °C) to three carbon atoms (550 °C), which leads to a bio-oil composed of lighter molecular weight compounds. Interestingly, despite decreasing the average carbon number, increasing temperature has no effect on the carbon-to-oxygen (C/O) ratio of bio-oil, demonstrating that temperature cannot be used to tune the C/O ratio of bio-oil, but can be used to optimize the bio-oil yield or change the bio-oil's product distribution (which is true for both thin-film and powder samples).
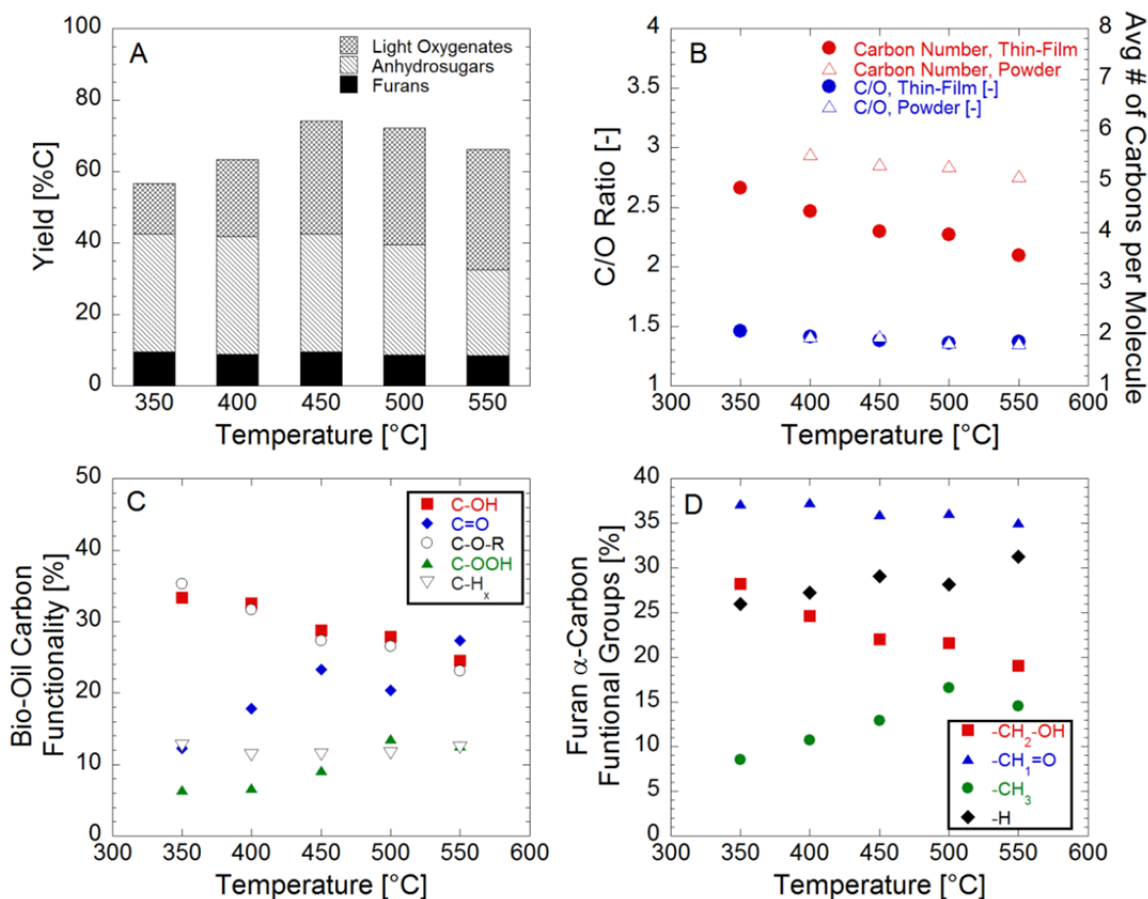
Figure 4.1 Yield of product classes, product functionality, carbon number, and carbon-to-oxygen ratio *vs.* temperature for thin-film pyrolysis of cellulose. (A) Yields of major product classes and total bio-oil are shown as a function of pyrolysis temperature. (B) The carbon-to-oxygen ratio and the average carbon number in the liquid bio-oil and permanent gases are shown as a function of pyrolysis temperature. (C) The functionality of every carbon in the bio-oil is plotted as a function of temperature; here C-OH represents alcohols, C=O represents aldehydes and ketones, C-O-R represents ether linkages, C-OOH represents carboxylic acids, and C-H$_x$ represents carbons with no oxygen functionality. (D) The functionality of the α-carbons for all furans are plotted as a function of temperature; here -CH$_2$-OH, -CH$_1$=O, -CH$_3$, or –H are the possible functional groups attached to the furan α-carbons.

4.5 Furan Ring Stability

Figure 4.2C shows that the total yield of furan rings (5-membered ring with four sp^2 carbon atoms and one oxygen atom) remains nearly constant when the reaction temperature is increased. The yields of hydroxymethylfurfural (HMF) (the most abundant furan) and furan methanol decrease as reaction temperature increases (Figure 4.2B) indicating that furan side

groups containing oxygen are unstable at higher reaction temperatures. While oxygenated furans decrease with increasing temperature, the yields of deoxygenated furans (furan and dimethyl furan) increase with increasing reaction temperature. This evidence indicates that the furan ring itself is very stable while oxygenated side groups (especially alcohols) are readily cleaved.

Figure 4.1D shows that furan alcohol groups ($-CH_2-OH$) decrease with increasing temperature, while deoxygenated furan groups ($-CH_3$) increase, suggesting that furan-alcohols are cleaved via hydrogenolysis to yield methyl group substituents on the α carbons. This deoxygenation reaction requires additional (extramolecular) hydrogen (by stoichiometry), which must be provided by *in situ* hydrogen transfer. One potential source for hydrogen is oxidation of alcohols to aldehydes/ketones ($H-C-OH \rightarrow C=O + H_2$). As shown in Figure 4.1C, the fraction of alcohol groups in pyrolysis vapors decreases with increasing temperature, while the fraction of aldehyde groups increases, thus providing a potential *in situ* hydrogen source. This suggests that promoting these types of reactions, which donate hydrogen during pyrolysis, may be able to reduce the oxygen content of bio-oil.

These results are consistent with previous work by the authors which found a mechanism for furan ring formation from cellulose without an anhydrosugar intermediate.[83] Our experimental evidence presented here shows that furan and anhydrosugar production has different temperature dependence which indicates that these pyrolysis products have parallel (rather than serial) formation mechanisms. This contrasts with the prevailing theory in the literature, which has postulated that the 5-membered furan ring forms via secondary reactions of anhydrosugars.[50]
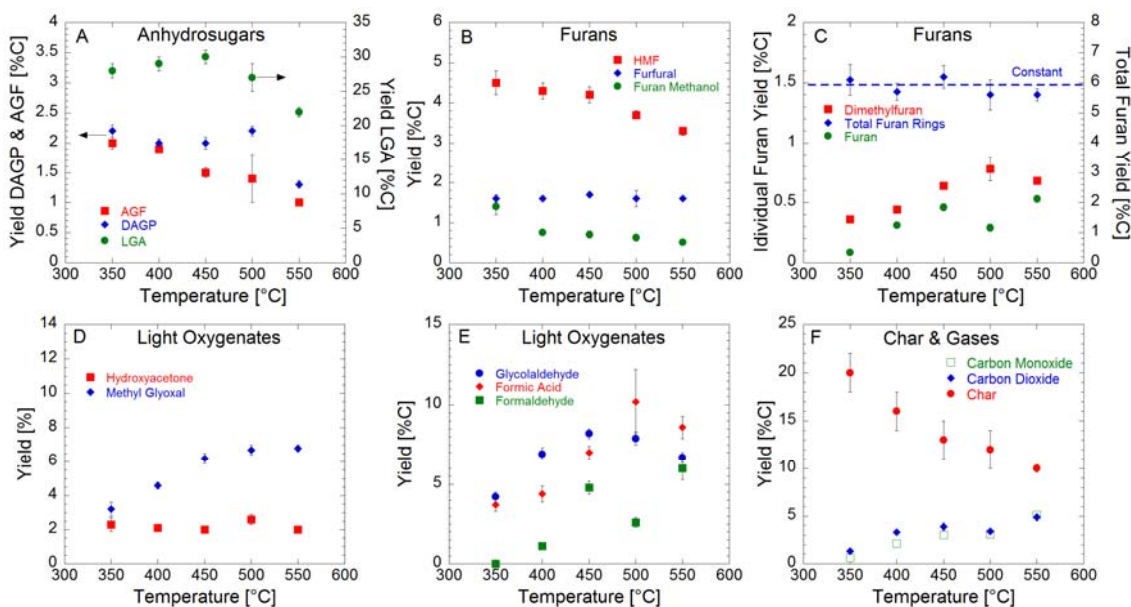
Figure 4.2 Yield of select thin-film cellulose pyrolysis products as a function of temperature. Yield is shown for (A) anhydrosugars, (B-C) furans, (D-E) light oxygenates, and (F) gases/char. Error bars represent a 90% confidence interval and are not shown if smaller than the width of symbols. Abbreviations: LGA – levoglucosan; AGF – 1,6 anhydroglucofuranose; DAGP – dianhydroglucopyranose; HMF – hydroxymethylfurfural.

4.6 The Effect of Temperature on Linear Oxygenate Formation

On a carbon basis, bio-oil production competes with gas (CO and CO_2) and char (solid carbon) production. As the pyrolysis temperature increases, char yield decreases due to products volatilizing prior to char formation. Higher pyrolysis temperatures (500 to 550 °C) also result in increased gas yields as carbon-carbon bond cleavage is more prevalent. Of the gaseous products, both CO and CO_2 yields increase in near lockstep from 350 °C to 550 °C, despite the fact that they have been shown to form through different reaction mechanisms.[27, 87] Similarly, formaldehyde yield also increases (from 0% to 6%) in conjunction with CO as pyrolysis temperature increases, indicating their mechanisms may be related. This supports previous work by our group[27] and others[87] that has shown formaldehyde and CO can form through the same reaction mechanism (i.e., they have a common intermediate) with formaldehyde derived from the C_1 carbon and CO derived from the C_2 carbon.[27] Formic acid yield also increases as temperature increases. However, it appears that formic acid yield reaches a maximum at 500 °C, which

37

suggests that formic acid may be an intermediate to a lighter pyrolysis product. This is consistent with our previous work which shows that formic acid is formed directly from the cellulose chain (C_1 carbon), and then dehydrogenates to form CO_2.[27]

4.7 The Role of Sample Length Scale on Product Yields

Previously, we have shown that levoglucosan (LGA) yields from powder and thin-film cellulose pyrolysis differ significantly (48% powder, 27% thin-film) at 500 °C.[27] We proposed this could be the result of different reaction temperatures, where average temperature in powder samples is lower due to the existence of thermal gradients. In contrast, the temperature within a micron-scale thin-film is uniform throughout[27] (Figure 2.2A). Figure 4.3A shows the difference in LGA yield between thin-film and powder at multiple temperatures. For the temperature range investigated here LGA yield is never statistically-equal between thin-film and powder pyrolysis, even if we compare results from the two techniques at different temperatures (e.g., compare LGA yield from thin-film at 350 °C to powder at 550 °C). This suggests that different average reaction temperatures alone are not responsible for yield differences between thin-film and powder pyrolysis techniques.

LGA is likely a primary product of cellulose pyrolysis that forms when an individual monomer from the cellulose chain breaks away.[50] After LGA forms it can volatilize or undergo secondary reactions within the intermediate liquid to form other anhydrosugars, pyrans, and light oxygenates.[83] As we have shown previously, LGA breaks down via secondary reactions within powder samples, but not in thin-film samples.[83] Therefore secondary reactions cannot account for the decreased yield of LGA in thin-film pyrolysis when compared to powder pyrolysis, and the phenomena responsible for higher LGA yield in powder pyrolysis remain unknown.
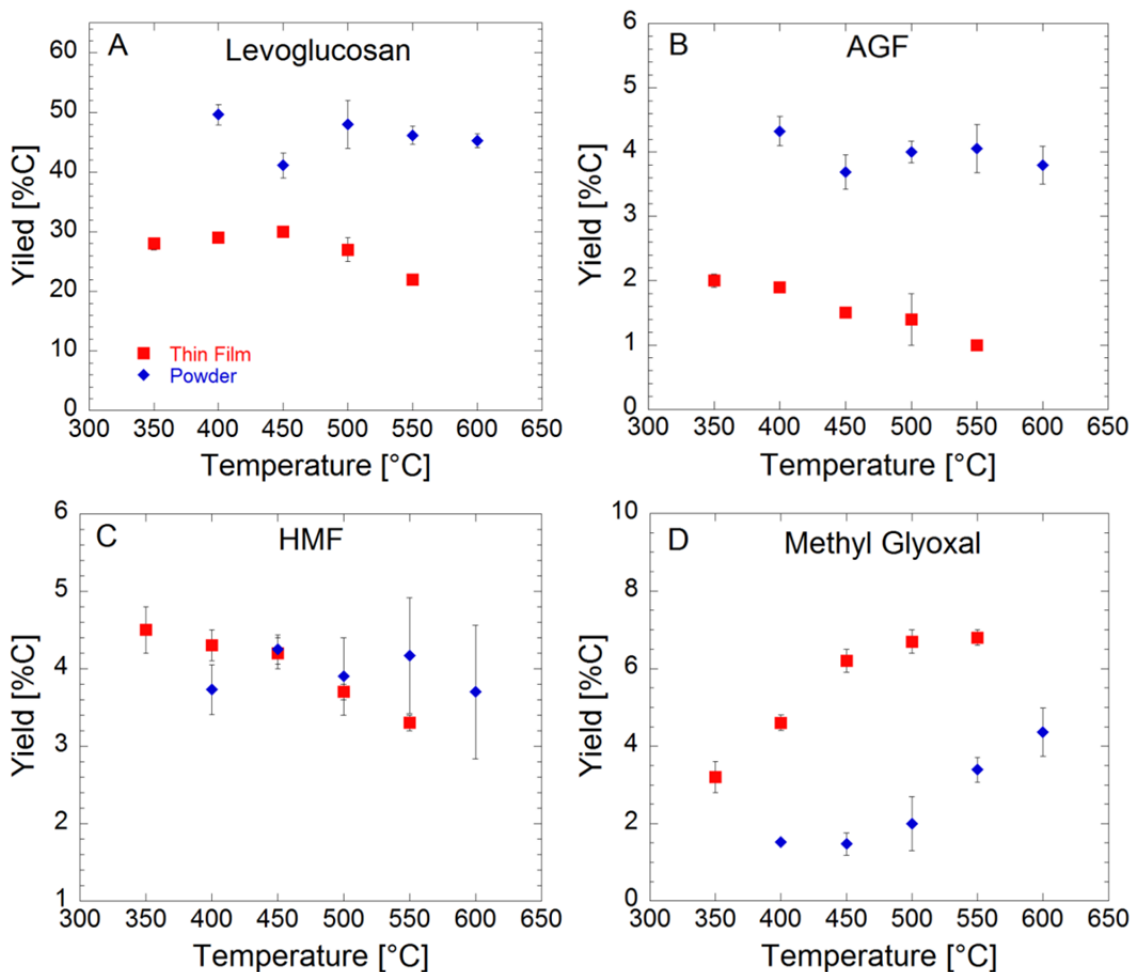
Figure 4.3 Comparison of product yields for micron and millimeter scale samples. Thin-Film results (red squares). Powder results (blue diamonds). Yields of major cellulose pyrolysis products are compared for thin-film (micron-scale) and powder (millimeter scale) experiments as a function of pyrolysis temperature. Error bars represent a 90% confidence interval and are not shown if smaller than the width of symbols.

Thin-film pyrolysis also produces substantially more light oxygenates than powder pyrolysis. Since light oxygenates have been shown to form directly from the cellulose chain,[27] it is likely that the relative rate of formation of light oxygenates (through primary pathways) increases (in thin-film experiments) in comparison to the relative rate of formation of LGA. Figure 4.3D shows the methyl glyoxal yield from powder experiments at 550 °C is about the same as the thin-film at 350 °C, suggesting that different temperature profiles may be the reason for disparate yields.

The difference between thin-film and powder experiments indicates the need to account for sample dimension when attempting to obtain kinetically-limited information. In samples that are too large (such as the powder samples in Figure 2.3C-F), the primary products of pyrolysis (such as LGA) can undergo secondary reactions within the liquid intermediate during powder pyrolysis.[83, 88] In fact, the yield of LGA has been shown to be a function of sample mass and therefore sample dimension,[88] indicating that sample dimension affects the interplay of transport and kinetics on product yields. In addition, any kinetic parameters derived from powder experiments will not reflect the intrinsic kinetics of cellulose pyrolysis, but rather heat and mass transfer limitations. Recently, a mechanism-generation approach to model fast pyrolysis of glucose-based carbohydrates (such as cellulose) was used to develop a kinetically-limited model.[89] However, experimental data obtained via powder pyrolysis (similar to the samples shown in Figure 2.3C-F, which are thermally and mass transfer limited) were employed to fit parameters of the model. This is possibly the reason why the model was unable to predict formic acid and glycolaldehyde yields, which the authors attributed to secondary reactions (characteristic of a thermally or mass transport limited system). With increasing focus on biomass pyrolysis, it is important to account for thermal and mass transfer limitations in biomass pyrolysis.

4.8 Conclusions

In this work, the effect of pyrolysis temperature and sample dimensions on the yield of individual products from cellulose pyrolysis has been examined. To reveal the effect of temperature, we employ a kinetically-limited, isothermal technique that utilizes thin-film samples of cellulose (which eliminates heat and mass transfer effects during cellulose pyrolysis). Our work presents evidence that furans (such as furfural and HMF) likely do not form via anhydrosugars but rather directly from the cellulose chain. We also show that once the 5-membered furan ring is formed, it does not break down; rather, larger molecular weight furan alcohols (such as HMF and 2-furanmethanol) are deoxygenated to form lighter molecular weight

furans (such as dimethylfuran). The data also suggests that alcohols (such as furan methanol) are more reactive than aldehydes (such as furfural). Furthermore, we link the formation of formaldehyde and CO as co-products of the same mechanism and present evidence that formic acid is an intermediate in the formation of CO_2. Additionally, by comparing product yields for powder (non-isothermal) and thin-film (isothermal) pyrolysis, we show that sample dimension drastically affects reaction pathways. We postulate that differences in product yields between conventional millimeter-scale powder samples and micron-scale thin-films are likely the result of mass transport effects rather than temperature gradients within powder samples.

CHAPTER 5

TUNING CELLULOSE PYROLYSIS CHEMISTRY VIA HETEROGENEOUS

CATALYST IMPREGNATION

5.1 Introduction

While the benefits of pyrolysis are significant, broad commercialization is hindered by several barriers, the most cited being the instability of the pyrolysis oil (or bio-oil) product.[90] Pyrolysis oil stabilization is commonly accomplished through catalytic hydrodeoxygenation which requires a large amount of hydrogen (relative to petroleum processes) and sacrifices yield to meet fuel quality specifications.[41, 91, 92] Technologies capable of reducing the hydrogen requirement, while improving pyrolysis oil stability and maintaining yield, would help bring pyrolytic biofuels to market.

The stability of pyrolysis oils is related to a number of chemical attributes, such as pH, oxygen content, and chemical composition. Furans are a major component of pyrolysis oil (5-20%)[27, 32, 50, 54, 74] and, while desirable as fuels (due to high energy density and research octane number)[57] and building block chemicals (due to having both nucleophilic and electrophilic centers)[93], they polymerize readily in the presence of sunlight or acidic substances. Aldehydic furans, such as 5-hydroxymethylfurfural (HMF) and furfural, are thought to be particularly prone to polymerization though acid-catalyzed aldol-condensation reactions.[94] This chemistry should be minimized during (1) primary pyrolysis in the intermediate liquid and (2) transportation and storage of the pyrolysis oil. In the case of biomass-derived furans (e.g., HMF and furfural), the aldehyde group is beta to the ring oxygen and can readily react with other ketones via aldol-condensation or with other nearby unsaturated carbons. This predisposition for polymerization makes aldehydic furans an undesirable product and minimizing their yield in favor of less

reactive furans (e.g., furan, methyl furan, dimethyl furan) would produce a more stable (and thus more transportable) pyrolysis oil.

5.2 Catalyst Impregnation Methods

In this work, we present a process wherein solid biomass is impregnated with decarbonylation catalysts (e.g., palladium on carbon, Pd/C) to convert oxygenated furans (e.g., HMF, furfural) to decarbonylated analogues (e.g., furan, methyl furan) within the intermediate liquid (Figure 5.1). By directly impregnating biomass with decarbonylation catalysts, we produce a deoxygenated pyrolysis oil with fewer aldehydic furans that is less prone to polymerization.
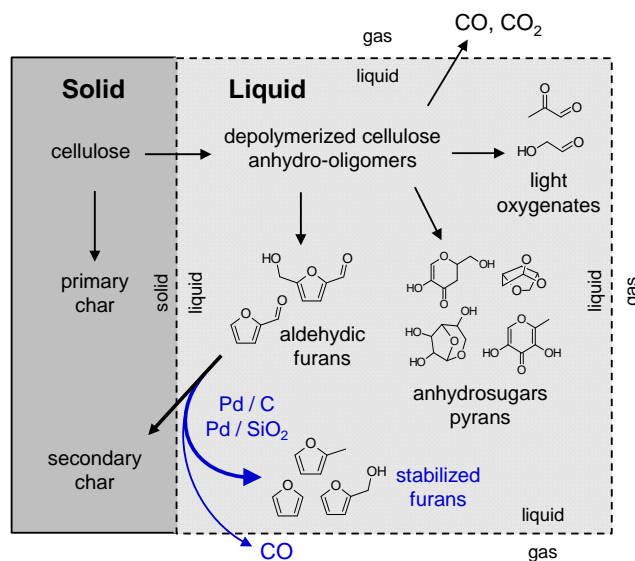
Figure 5.1 Solid- and liquid-phase cellulose pyrolysis chemistry. Decarbonylation catalysts can redirect liquid phase chemistry to improve pyrolysis oil quality while maintaining yield.

Previous work impregnating biomass with inorganic materials has focused largely on understanding naturally occurring materials in biomass, such as metal oxides and silica,[66] with the idea that inorganics, detrimental to pyrolysis oil quality, should selectively be removed. Here, we test the potential benefits for impregnating solid biomass prior to pyrolysis, an approach that has been largely unexamined in the literature. Scale-up issues (difficulty in impregnating solid

biomass and concerns about catalyst recovery and regeneration) not-withstanding, our work addresses for the first time whether this approach should be investigated in future research.

Catalytic co-pyrolysis experiments were conducted by combining cellulose and catalysts to form a solid mixture that is then pyrolyzed in a short contact time reactor.[26, 27, 29, 74] The cellulose-catalyst powder mixture has a characteristic length of ~2 mm making conversion limited by internal heat transfer[27]. Previous work in our group has utilized thin films to overcome heat transfer limitations for study of fundamental thermolysis chemistry. However, in this work, larger samples representative of the length scales of biomass particles seen in fast pyrolysis reactors are subjected to catalyst impregnation, allowing oxygenates to interact with active sites prior to evaporation from the cellulose melt.

Catalytic pyrolysis experiments were conducted by pyrolyzing solid mixtures of cellulose and supports or supported metal catalysts with 20 wt % support + metal and 80 wt % cellulose. For most experiments, the metal surface area to cellulose (m^2-metal / g-cellulose) was constant at 0.75 m^2-metal / g-cellulose in order to distinguish the difference between different metals. Solid mixtures of catalyst and cellulose were pyrolyzed in a batch micropyrolysis reactor (Frontier 2020 micropyrolyzer) under a helium atmosphere (total pressure of 3 bar) and a typical pyrolysis reaction temperature (500 °C). The reactor is capable of matching the heating rates seen in fast pyrolysis.[27] Catalytic and non-catalytic pyrolysis experiments produced very similar product species, albeit in different amounts. Permanent gases (CO and CO_2) and volatile oxygenates were characterized in a gas chromatograph-mass spectrometer (GC-MS), as reported in previous work by the authors [26, 27, 74]. Solid char was quantified using a post-reaction burn off step wherein oxygen was injected into the reactor and CO and CO_2 were measured by GC-TCD. Catalyst metal surface areas were determined by hydrogen (Pt catalysts) or CO (Pd, Ni, Co catalysts) chemisorption (see Table 5.1).

Table 5.1 Metal surface area for supported metal catalysts. Measurements were conducted using chemisoption with CO as the titration gas for Pd, Ni, and Co and H2 for Pt.

Catalyst	Surface Area [m^2/g]	Dispersion [%]
1.7 Pt/Alumina	2.70	64
10Pd/Alumina	6.24	14
5Pt/Carbon	5.16	42
10Pd/Carbon	6.19	14
5Pt/Silica	1.27	10
10Ni/Alumina	2.51	3.8
10Co/Alumina	1.11	1.6
5Pd/Silica	1.95	4.4

5.3 The Effects of Metal Impregnation on Cellulose Pyrolysis

Figure 5.2 shows pyrolysis oil yield as a function of percent decarbonylated furans for a number of catalysts. The obvious operational objective of any pyrolysis reactor designed for biofuels production is to maximize pyrolysis oil yield while improving stability and quality (e.g., energy density, C-to-O ratio). Here, our objective is to produce the same or better pyrolysis oil yield as in the non-catalytic case (blue square in Figure 5.2) while achieving 100% decarbonylated furans in the product mixture. We find that supported palladium catalysts (Pd/C, Pd/SiO$_2$) largely achieve this goal with Pd/C being the best (at constant metal surface area (0.75 m^2 / g-cellulose). Figure 5.2 shows that when Pd/C is impregnated within cellulose, the percentage of decarbonylated furans increases from 23% (no catalyst case) up to 88% (1.5 m^2/g-cel.) while pyrolysis oil yield is only slightly reduced from 77 %C (catalyst free case) to 68 %C. Further evidence for decarbonylation chemistry (rather than dehydration) is the sharp increase in CO yield from 1.4 %C to 9.0 %C (0.75 m^2/g-cel.) and then 17.9 %C for the highest catalyst load (1.5 m^2/g-cel.; see Table 5.2).

Table 5.2 Yields from catalytic pyrolysis of cellulose at 500 °C. Samples were pyrolyzed as solid mixtures with a cellulose-to-catalyst ratio of 80:20 (mass basis). All experiments were run in triplicate and generally 90% confidence intervals were <20% of the values reported below. Metal surface areas were measured using H2 or CO chemisorption. Carbon balance is pyrolysis oil components [27], CO, CO2 and char (quantified via burn off).

Catalyst	Metal Catalyst Load [m^2 / g-cel.]	Metal Surface Area [m^2 / g-cat.]	Yield, Total Furans [%C]	Decarbonylated Furans [% of total furans]	Yield, Pyrolysis Oil [%C]	Yield, CO [%C]	Carbon Balance [%C]
No Catalyst	-	-	7.8	23.0	77.3	1.4	89.7
C	-	-	9.9	26.4	80.0	1.8	83.7
SiO_2	-	-	8.4	28.6	71.8	2.8	85.2
Al_2O_3	-	-	13.5	17.0	69.0	2.1	76.7
Pd / C	0.28	6.19	6.6	46.6	72	4.2	78.6
Pd / C	0.75	6.19	6.1	71.8	74.4	9	85.1
Pd / C	1.5	6.19	8.0	88.4	69.6	17.9	89.4
Pt / C	0.28	5.16	5.2	57.1	75.9	7.6	85.8
Pt / C	0.75	5.16	5.1	66.8	51.5	29.2	84.4
Pt / C	1.5	5.16	4.9	76.5	37	41.8	83.4
Pd / SiO_2	0.75	1.95	5.3	57.8	78.7	6.7	90.4
Pt / SiO_2	0.75	1.27	5.3	50.3	68	6.3	84.9
Pd / Al_2O_3	0.75	6.24	12.3	30.8	68.3	6	82.3
Pt / Al_2O_3	0.75	2.7	11.2	22.4	72.8	4.9	83.5
Ni / Al_2O_3	0.75	2.51	11.4	19.7	74	3.7	86.2
Co / Al_2O_3	0.75	1.11	14.4	17.3	73.6	3.2	83.1

In addition to Pd, Pt also showed activity for decarbonylation and was tested on three supports (carbon, Al_2O_3 and SiO_2). Pt/C was found to be the most active for decarbonylation but the least selective (in terms of pyrolysis oil yield). At a constant surface area (0.75 m^2/g-cel.), decarbonylated furans increase from 23% (no catalyst) to 67% when Pt/C is added. However, in addition to being active for decarbonylation, Pt catalysts reduce pyrolysis oil yield (from 77% to 51% for Pt/C) due to increased C-C bond cleavage. This limits the utility of Pt catalyst for decarbonylation of pyrolysis products. Ni and Co supported metals were also tested, but they were largely inactive (Figure 5.2).
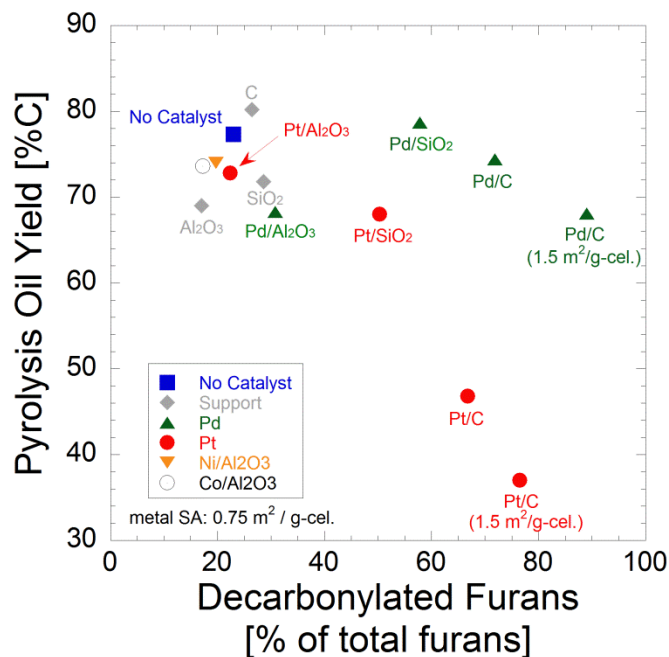
Figure 5.2 Pyrolysis oil yield versus decarbonylation selectivity for various supported metal catalysts. Supports and supported metal catalysts were co-pyrolyzed with cellulose powder at 500°C. Solid mixtures were 80 wt% cellulose and 20 wt% catalyst (support + metal). Metal surface area was constant at 0.75 m^2-metal / g-cellulose, except as indicated in parentheses.

Figure 5.3 shows a detailed breakdown of furan yields for the catalyst-free, C only, Pd/C, and Pt/C cases. Addition of the carbon support increased total furan yield compared to the catalyst-free case (+2.1 %C on total C basis). The slight change in product distribution is statistically significant (90% confidence interval is 0.5 %C) and could be due to the mild acidity of the carbon support or to changes in the temperature profile throughout the cellulose/catalyst mixture when the carbon is added (since the powder experiment is heat transfer limited)[27]. When the Pd catalyst is added to the carbon support at 1.5 m^2-Pd / g-cellulose, the total furan yield decreases from 9.9 %C to 7.5 %C. This decrease in total furan yield is near the expected stoichiometric carbon loss for a single decarbonylation of furfural and a double decarbonylation of HMF (-1.8 %C based on the difference in yields between support only and Pd/C experiments). This supports the hypothesis that Pd/C is selectively converting aldehydic furans through decarbonylation chemistry (rather than alkylation or hydrogenation).

47

Figure 5.3 also shows that the most abundant aldehydic furan molecules are HMF and furfural whereas the dominant decarbonylated furans are methyl furan and furan. This is also consistent with decarbonylation stoichiometry of aldehydic furans since methyl furan and furan are the products of HMF and furfural decarbonylation, respectively. In the catalyst-free reference case, the methyl furan-to-HMF ratio is 0.05, whereas for the Pd/C high catalyst load case (1.5 m^2-Pd / g-cel.) the ratio is 5.5, a 100-fold increase. Pd does not only act as an excellent decarbonylation catalyst but is also capable of hydrodeoxygenating side groups of furans to saturation. Interestingly, the ratio of furan methanol (another product of HMF decarbonylation) to HMF changes less with the addition of Pd/C (from 0.1 to 1.1) indicating that the $C_6 CH_2OH$ group of HMF does not undergo decarbonylation to the same extent as the C_1=O group since decarbonylation (C-C bond scission) is promoted upon dehydrogenation of a species.[95] It is important to note that since no external hydrogen is provided, hydrogenation occurs through hydrogen-transfer between liquid-phase species (with char being the likely by-product for the species losing the hydrogen).
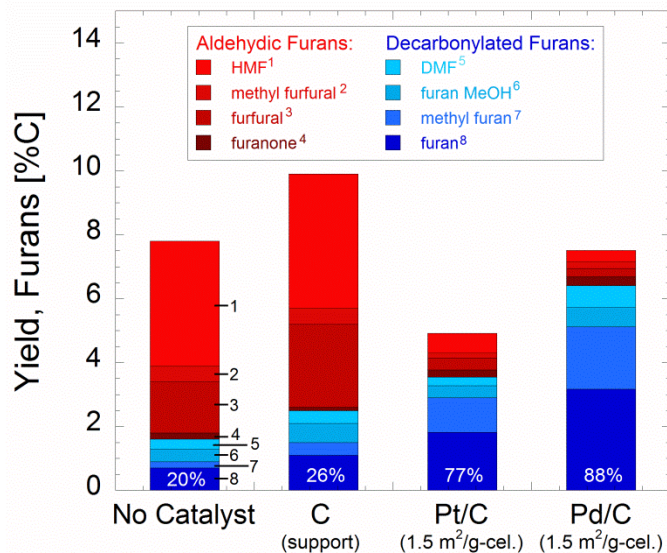
Figure 5.3 Furan yields for Pt/C and Pd/C catalysts. Supports and supported metal catalysts were co-pyrolyzed with cellulose powder at 500°C. Metal surface area per gram cellulose is indicated in parentheses. Superscripts in the legend correspond to numbers on leftmost bar. Percent decarbonylated furans (out of total furans) is shown in white text at the bottom of each bar.

Figure 5.4 shows the effect of catalyst loading (in the form of metal surface area) on furan yields for Pd/C and Pt/C. Pd/C and Pt/C have very different functionalities with increasing surface area. The yield of decarbonylated furans (blue bars; furan, methyl furan, dimethyl furan, and furan methanol) increases with increasing surface area for both Pt/C and Pd/C. However, the catalysts exhibit different total furan yield with increasing surface area. Total furan yield is constant with increasing surface area for Pt/C while total furan yield is parabolic for Pd/C. Interestingly, Pd/C has a minimum total furan yield at intermediate catalyst loading. This indicates that at higher surface areas, Pd/C not only selectively decarbonylates furans but also promotes furan ring formation. This indicates that furan decarbonylation catalysts can potentially increase decarbonylated furans yield higher than the total furan yield of the catalyst-free case (See Tables 5.3 and 5.4 for complete all products yields).
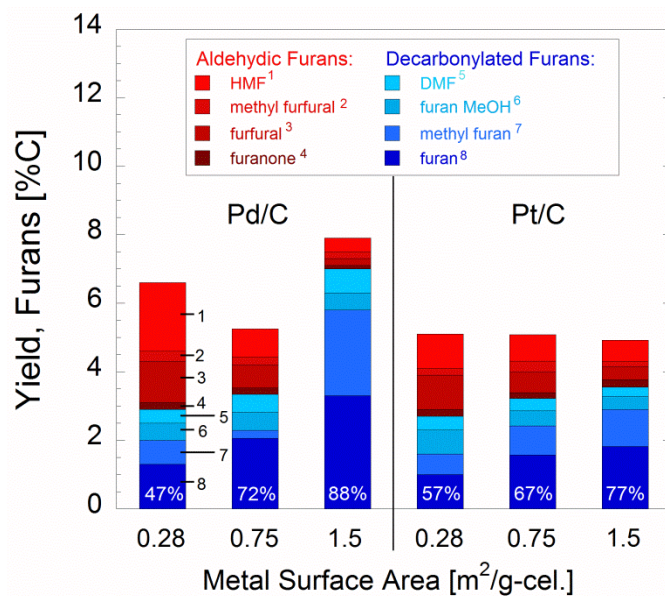
Figure 5.4 Furan yields as a function of surface area for Pd/C and Pt/C catalysts. Cellulose was co-pyrolyzed with catalyst at 500 °C. Superscripts in the legend correspond to numbers on leftmost bar. Percent decarbonylated furans (out of total furans) is shown in white text at the bottom of each bar.

Table 5.3 Twenty seven products were identified and quantified for cellulose co-pyrolysis with varying degrees of metal loading for 5Pt/Carbon and 10Pd/Carbon.

	5 Pt/Carbon (0.75 m^2/g-cel)	10Pd/Carbon (0.75 m^2/g-cel)	5 Pt/Carbon (1.5 m^2/g-cel)	10Pd/Carbon (1.5 m^2/g-cel)
Anhydrosugars				
Levoglucosan	27.86	48.85	16.01	43.7
AGF	1.90	4.31	1.05	5.0
DAGP	0.75	0.84	0.62	0.83
Levoglucosenone	0.52	0.60	0.56	1.2
Pyrans				
ADGH	0.33	2.44	0.37	1.8
Furans				
Hydroxymethylfurfural	0.77	0.82	0.62	0.4
Furfural	0.60	0.67	0.38	0.2
5-Methyl Furfural	0.32	0.23	0.15	0.2
2-Furanmethanol	0.44	0.53	0.38	0.5
2,5 Dimethyl Furan	0.36	0.52	0.27	0.7
2-Methyl Furan	0.85	1.11	1.08	2.5
Furan	1.57	2.06	1.82	3.3
2(5H) Furanone	0.17	0.19	0.22	0.1
Light Oxygenates				
Methyl Glyoxal	1.51	0.74	0.41	0.2
Glycolaldehyde	2.41	2.60	2.08	3.6
Formaldehyde	0.9	3.3	0.3	1.1
Hydroxyacetone	0.87	0.14	0.66	0.2
Acetic Acid	0.49	0.11	0.39	0.2
2,3 Butanedione	1.12	0.52	1.72	0.1
Formic Acid	2.56	1.77	2.53	1.4
Glyoxal	3.75	1.19	4.58	1.0
Permanent Gases				
Carbon Dioxide	3.71	1.69	4.56	1.9
Carbon Monoxide	29.15	9.02	41.83	17.9
Other				
CPHM	0.29	0.13	0.12	0.3
Catechol	0.45	0.16	0.42	0.0
1,2-Cyclopentanedione	0.43	0.24	0.17	0.5
Char	-	-	-	-
Total	84.4	85.1	83.4	89.1

Abbreviations: AGF, 1,6 Anhydroglucofuranose DAGP, dianhydroglucopyranose; ADGH, 1,5-anhydro-4-deoxy-D-glycero-hex-1-en-3-ulose; CPHM, 2-hydroxy-3-methyl-2-cyclopenten-1-one

Table 5.4 Twenty seven products were identified and quantified for cellulose co-pyrolysis Pt, Pd, Co, and Ni supported on silica and alumina.

	5 Pt/SiO$_2$ [0.75 m^2/g-cel]	10 Pd/ SiO$_2$ [0.75 m^2/g-cel]	1.7 Pt/Al$_2$O$_3$ [0.75 m^2/g-cel]	10 Pd/ Al$_2$O$_3$ [0.75 m^2/g-cel]	10 Ni/ Al$_2$O$_3$ [0.75 m^2/g-cel]	10 Co/ Al$_2$O$_3$ [0.75 m^2/g-cel]
Anhydrosugars						
Levoglucosan	32.95	52.80	39.26	34.77	40.71	33.98
AGF	1.94	4.31	2.48	2.14	2.84	2.12
DAGP	0.90	0.94	1.64	1.82	1.58	1.90
Levoglucosenone	0.17	0.23	0.69	0.27	0.58	1.55
Pyrans						
ADGH	0.57	3.16	3.08	2.82	2.52	2.32
Furans						
Hydroxymethylfurfural	0.81	0.81	4.77	4.47	4.88	6.30
Furfural	1.33	1.09	3.33	3.44	3.63	4.60
5-Methyl Furfural	0.51	0.35	0.59	0.60	0.68	1.00
2-Furanmethanol	0.51	0.62	0.43	0.46	0.42	0.43
2,5 Dimethyl Furan	0.52	0.25	0.13	0.29	0.18	0.35
2-Methyl Furan	0.34	0.60	0.56	0.77	0.49	0.55
Furan	0.79	1.50	1.28	2.13	1.04	1.01
2(5H) Furanone	0.51	0.12	0.11	0.14	0.13	0.13
Light Oxygenates						
Methyl Glyoxal	5.64	1.62	3.08	2.70	3.60	4.52
Glycolaldehyde	4.92	2.12	3.09	2.98	3.04	3.29
Formaldehyde	6.1	3.9	2.3	3.2	2.6	3.1
Hydroxyacetone	2.79	0.27	0.13	0.18	0.17	0.61
Acetic Acid	0.62	0.14	0.14	0.13	0.21	0.28
2,3 Butanedione	0.75	0.43	0.42	0.46	0.50	0.66
Formic Acid	1.92	2.21	3.60	2.58	2.50	2.51
Glyoxal	0.91	0.75	0.76	0.83	0.74	0.85
Permanent Gases						
Carbon Monoxide	4.46	1.69	1.77	1.87	2.39	2.92
Carbon Dioxide	6.28	6.69	4.90	6.01	3.73	3.20
Other						
CPHM	0.45	0.07	0.10	0.14	0.13	0.17
Catechol	0.62	0.14	0.21	0.27	0.21	0.23
1,2-Cyclopentanedione	0.81	0.15	0.24	0.33	0.25	0.32
Char	6.2	3.3	4.1	6.1	6.1	7.4
Total	84.9	90.4	83.5	82.3	86.2	83.1

5.4 Choosing a Support for Palladium

Supported metal catalysts are highly active and can be recovered post-pyrolysis. From a fundamental perspective, one challenge in discovering and effective catalyst is to distinguish between metal and support influences on cellulose pyrolysis chemistry. This is especially important if the support material has a negative effect on cellulose pyrolysis chemistry by promoting the formation of unstable oxygenated products. In order to compare various metal catalysts, inert support materials are desired. In this work, we identify supports that are inert during impregnated cellulose pyrolysis and can therefore be used to study the influence of various

metals on condensed-phase pyrolysis chemistry during catalyst-impregnated pyrolysis (CIP) of biomass.

Table 5.5 Eight support materials examined in impregnated pyrolysis of cellulose. BET surface area was measured using nitrogen adsorption. Particle size was measured using the Mastersizer 2000 and detailed plots of the particle size distribution for each support material are can be seen in Figure 5.5. R^2 values describe the variation between pyrolysis of cellulose with and without the support material and are also listed in Figure 5.6.

Support	BET Surface Area [m^2/g]	Particle Size [μm]	R^2
Aluminum Oxide	89	2.8	0.258
Titanium Dioxide	3.6	3.9	0.368
Zirconium Oxide	21	7.1	0.705
Magnesium Oxide	120	41	0.742
Tungsten Carbide	1.3	3.6	0.771
Calcium Oxide	7.9	60	0.879
Carbon	15	5.9	0.909
Silicon Dioxide	220	130	0.928

Support materials were tested by using a co-pyrolysis technique wherein a mixture of cellulose (80 wt%) and support (20 wt%) is pyrolyzed in a flash pyrolysis reactor (500 °C) and products are analyzed using GC-MS.[27] A total of eight support materials, listed and characterized in Table 5.5, were co-pyrolyzed with cellulose. Mixtures were created using a mortar-and-pestle technique to ensure complete mixing, after which, 1.5 ± 0.1 mg of the mixture was placed in a pyrolysis crucible. These sample sizes are indicative of powder pyrolysis, which is not kinetically limited,[27, 29] and were chosen intentionally in order to ensure adequate contact between the intermediate liquid cellulose and the support material. A burnoff technique was used to quantify char yield and was conducted in the manner described in previous work.[27, 29]

Support materials were tested by using a co-pyrolysis technique wherein a mixture of cellulose (80 wt%) and support (20 wt%) is pyrolyzed in a flash pyrolysis reactor (500 °C) and products are analyzed using GC-MS.[27] A total of eight support materials, listed and characterized in Table 5.5, were co-pyrolyzed with cellulose. Mixtures were created using a mortar-and-pestle technique to ensure complete mixing, after which, 1.5 ± 0.1 mg of the mixture was placed in a

pyrolysis crucible. These sample sizes are indicative of powder pyrolysis, which is not kinetically limited,[27, 29] and were chosen intentionally in order to ensure adequate contact between the intermediate liquid cellulose and the support material. A burnoff technique was used to quantify char yield and was conducted in the manner described in previous work.[27, 29]

Figure 5.5 Particle size distributions for eight support materials. Data was collected using a Mastersizer 2000 particle size analyzer.

Table 5.6 Twenty seven products were identified and quantified for cellulose co-pyrolysis with eight different support materials.

Support	No Support	Al$_2$O$_3$	TiO$_2$	MgO	ZrO$_2$	WC	CaO	C	SiO$_2$
Anhydrosugars									
Levoglucosan	48	32	43	46	41	42	40	49	42
AGF	4.0	2.2	3.3	2.9	3.4	3.6	2.6	4.3	3.6
DAGP	0.1	2.1	1.1	0.9	1.1	1.8	0.7	1.3	1.2
Levoglucosenone	0.3	0.8	0.2	0.1	0.4	0.6	0.1	0.4	0.4
Pyrans									
ADGH	3.8	4.0	4.7	1.8	3.5	4.4	2.8	3.6	4.6
Furans									
Hydroxymethylfurfural	3.9	5.9	6.7	3.9	4.1	2.3	4.1	4.2	3.7
Furfural	1.6	4.5	2.6	2.0	2.5	2.1	1.5	2.6	1.9
5-Methyl Furfural	0.5	0.8	0.5	0.4	0.4	0.5	0.4	0.5	0.4
2-Furanmethanol	0.4	0.2	0.2	0.1	0.2	0.3	0.2	0.6	0.1
2,5 Dimethyl Furan	0.3	0.6	0.8	0.7	0.6	0.6	0.5	0.4	0.5
2-Methyl Furan	0.2	0.5	0.5	0.3	0.4	0.5	0.3	0.4	0.5
Furan	0.6	0.8	0.9	0.5	1.0	1.4	0.5	1.1	1.0
2(5H) Furanone	0.2	0.3	0.3	0.3	0.3	0.3	0.3	0.1	0.3
Light Oxygenates									
Methyl Glyoxal	2.0	3.0	4.4	7.1	2.5	3.2	4.1	2.3	2.4
Glycolaldehyde	1.9	3.5	3.0	2.8	1.9	3.0	2.2	2.6	2.2
Formic Acid	2	0.9	2.4	2.2	1.7	4.3	2.4	1.7	1.3
Formaldehyde	4.4	4.2	3.7	4.4	3.4	3.8	2.8	3.2	3.4
Hydroxyacetone	0.5	0.1	0.5	1.1	0.3	0.6	0.9	0.1	0.1
Acetic Acid	0.3	0.3	0.5	0.5	0.4	0.5	0.4	0.2	0.2
2,3 Butanedione	0.4	0.3	0.5	0.6	0.4	0.5	0.4	0.5	0.4
Glyoxal	0.3	0.6	0.7	0.9	0.4	0.6	0.5	0.3	0.8
Permanent Gases									
Carbon Monoxide	1.4	2.1	2.4	2.0	2.1	2.5	1.9	1.8	2.8
Carbon Dioxide	2	2.0	2.8	3.4	2.3	2.3	2.4	2.0	2.4
Other									
CPHM	0.2	0.1	0.2	0.2	0.1	0.1	0.2	0.1	0.1
1,2-Cyclopentanedione	0.2	0.3	0.4	0.3	0.2	0.2	0.3	0.2	0.3
Char	9	3.5	3.5	10.6	5.4	15.1	11.3	0.0	8.1
Catechol	0.2	0.2	0.3	0.3	0.1	0.3	0.2	0.0	0.1
Total	90	77	90	97	81	97	85	84	85

Table 5.6 shows the yields of the top 28 products that are produced from cellulose co-pyrolysis (with eight different supports) and pure cellulose. In order to characterize the activity of a support, product yields of pure cellulose pyrolysis are plotted against those of cellulose/support co-pyrolysis for all eight supports. The resulting parity plots are shown in Figure 5.6 with each plot containing a parity line (y = x) upon which all data points will fall if a support is inert (i.e. the same yields for pure cellulose and cellulose co-pyrolysis). In addition, the 'coefficient of determination' (R^2: calculated using product yields of less than 10%) is included for each parity plot to quantify the inertness of each support material (a perfectly inert support will have an R^2 of one).

Visual examination of the plots and the R^2 values indicates that carbon and silicon dioxide have little effect on cellulose pyrolysis yields, while aluminum oxide and titanium dioxide strongly affect pyrolysis yields. Interestingly, the BET surface area (Table 5.5) of silicon dioxide (220 m^2/g) is significantly higher than that of more active materials such as aluminum oxide (89 m^2/g) and titanium dioxide (3.6 m^2/g) suggesting that silicon dioxide is truly inert and not simply active with limited available surface area. While carbon and silicon dioxide are both inert, silicon dioxide has the added advantage of being recoverable after char residue is burned off. Therefore, silicon dioxide fits both objectives of this work and is recommended as an inert support.
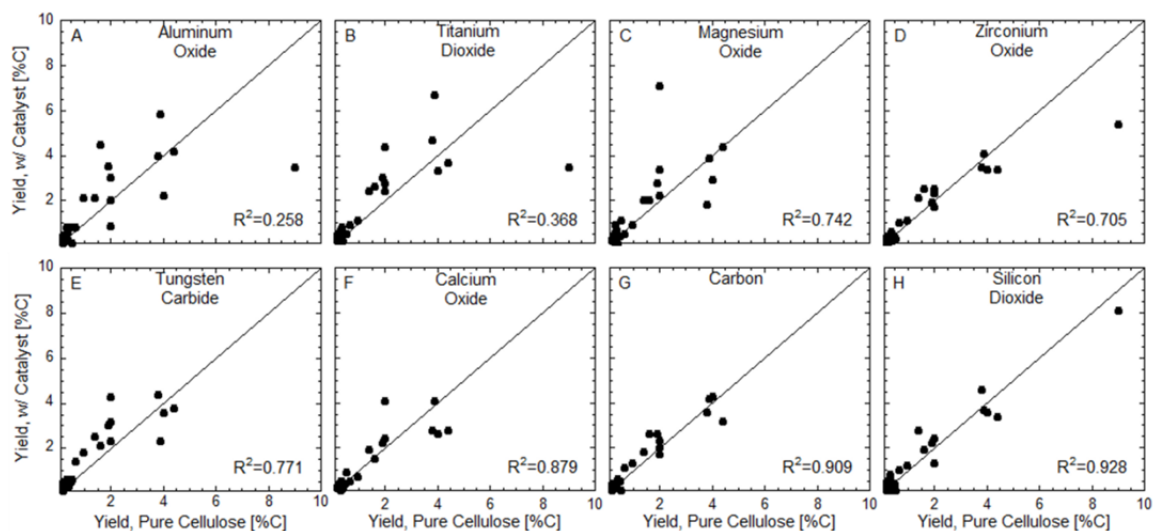
Figure 5.6 Parity plots comparing cellulose pyrolysis products with and without a catalyst support. All data points of an inert support fall on the parity line y = x. Included in each plot is the 'coefficient of determination' (R^2) value calculated using only yield values below 10%. A value of one represents a perfectly inert support.

Silicon dioxide was further co-pyrolyzed with four saccharides (glucose, fructose, cellobiose, and α-cyclodextrin) in order to confirm the inert nature of silicon dioxide for multiple applications as shown in Figure 5.7. Both cellobiose and α-cyclodextrin, chosen because they share the same glucose monomer with cellulose, are largely unaffected by the addition of silicon dioxide during pyrolysis ($R^2_{cellobiose} = 0.995$ and $R^2_{\alpha\text{-cyclodextrin}} = 0.964$). Similarly, when glucose, the monomer of cellulose, and fructose, a saccharide monomer that differs from glucose, are co-

pyrolyzed with silicon dioxide, the product distribution is again largely unaffected ($R^2_{glucose}$ =

0.972 and $R^2_{fructose}$ = 0.949). This suggests that silicon dioxide remains inert during the pyrolysis

of many different saccharides.
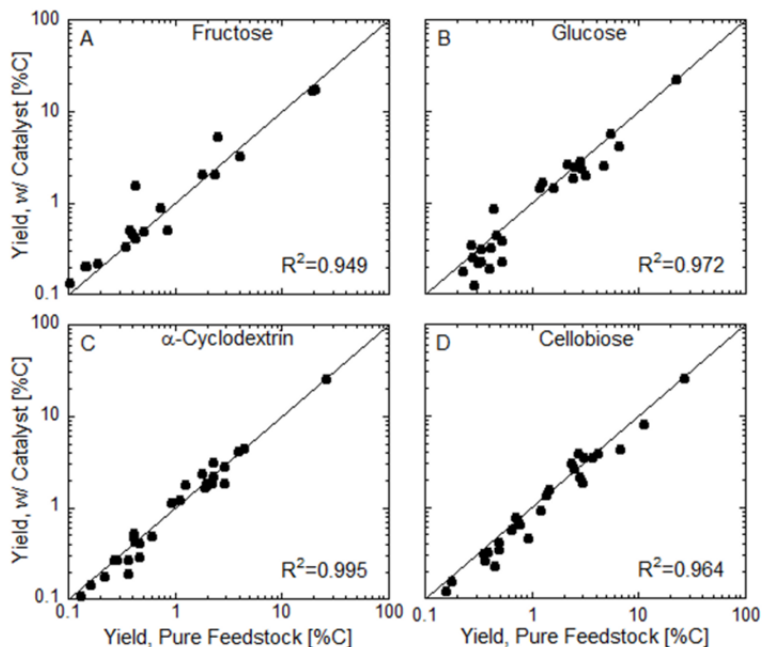
Figure 5.7 Parity plots comparing four different saccharides pyrolyzed with and without silicon dioxide. Included in each plot is the 'coefficient of determination' (R^2) value where a value of one represents a perfectly inert support.

While we have shown that silicon dioxide is inert during cellulose pyrolysis, it is

interesting to note that silicon dioxide also occurs naturally in biomass.[96] The presence of silicon

dioxide in plants is believed to play an important role in fighting diseases and pests, as well as in

providing structural integrity and mitigating metal toxicity.[97] Silicon dioxide is also the primary

component of ash within biomass feedstocks including switchgrass, rice straw, and poplar, and it

has been suggested that the silicon dioxide present in biomass does not affect cellulose

pyrolysis.[66] However, the activity of silicon dioxide in lignin or hemicellulose pyrolysis remains

to be investigated.

5.5 Conclusion

In summary, our work shows that decarbonylation catalysts can effect condensed-phase pyrolysis chemistry (Figure 5.1) and reduce aldehydic furan production to improve pyrolysis oil quality while maintaining pyrolysis oil yield. Additionally, we find that palladium catalysts, especially Pd/C, are selective towards decarbonylation of aldehydic furans within the pyrolytic intermediate liquid. Future work will focus on identifying other, less expensive heterogeneous catalysts of similar or higher decarbonylation activity and selectivity to help improve the economics of next-generation pyrolytic biofuels production processes.

CHAPTER 6

SPATIALLY AND TEMPORALLY RESOLVED SPECTROSCOPY

OF FAST PYROLYSIS

6.1 Introduction

Progress toward mechanistic understanding of fast pyrolysis is limited by the complexity

of the reaction environment.[98] Pyrolysis reactions occur in three distinct phases: solid virgin

biopolymers,[87, 99] gas-phase pyrolysis vapors, and a short-lived (<100 ms) liquid intermediate.[42, 43]

At the industrial scale, these phases exist within a multi-scale system consisting of atomic-scale

biopolymer/melt chemistry (10^{-10} to 10^{-9} m), particle/cellular heating and reaction (10^{-6} to 10^{-3} m),

and reactor conversion (10^{-1} to 10^{1} m).[98] A complete kinetic description of pyrolysis systems will

utilize a bottom-up approach, whereby biopolymer chemistry is integrated within

reaction/transport particle models, which are ultimately included in complex fluid bed reactor

models.

Understanding of molecular-scale chemistry of pyrolysis has rapidly progressed from

lumped-kinetic models of the past few decades. While initial lumped chemistries predicted the

rate of generation of gases, vapors and char,[54, 61] new experimental and computational techniques

are revealing the pathways, mechanisms and kinetics of cellulose and lignocellulose pyrolysis.

For example, development of the technique, 'thin-film pyrolysis' (TFP), has characterized the

first set of pyrolysis products produced by primary condensed-phase reactions absent heat and

mass transport limitations.[27] TFP has also led to the discovery of a chain-length effect in cellulose

pyrolysis[74] and the stability of the five-membered furan ring within the liquid intermediate.[29]

Additionally, secondary condensed-phase reactions of cellulose have been examined by another

experimental technique called, 'co-pyrolysis,' which has revealed the condensed-phase reactions

of levoglucosan to produce pyrans, anhydrosugars, and light oxygenates.[26] In parallel, the use of

ab initio molecular dynamics and DFT has described the high temperature behavior of cellulose,[100, 101] the mechanisms associated with glycosidic cleavage,[27, 102] and the formation of pyrolysis products including furans[27, 87, 103] and light oxygenates.[27, 103] These discoveries are rapidly leading to the development of molecular-level kinetic models of cellulose[89] and eventually lignocellulose pyrolysis.

Despite significant improvement in understanding molecular-level cellulose pyrolysis chemistry, progress towards the modeling of lignocellulose pyrolysis chemistry and transport phenomena within wood fibers during pyrolysis remains a challenge. Over the past few decades, it has been conclusively shown that heating rates of lignocellulosic particles/fibers in the range of 0.1-1.0 MW m^{-2} produces higher yields of bio-oil.[21, 22, 53, 54, 61] At these conditions, initial heating of a particle conducts thermal energy through the cellular structure of lignocellulosic biomass. In turn, the particles exhibit a propagating thermal front, consistent with high Biot numbers (Bi >>1) which drives pyrolysis chemistry in multiple zones[104] as depicted by the cutaway in Figure 6.1a. Leading this front is a drying zone, wherein moisture evaporates.[105] This is followed by the pyrolysis zone wherein the lignocellulosic biopolymers are depolymerized to form intermediate liquids, driving microstructural collapse (shrinkage) of biomass[98, 106] and producing vapors and aerosols.[43] As pyrolysis goes to completion, the resulting porous char zone (which will comprise the entire wood particle upon 100% conversion) conducts heat, transports volatiles, and traps aerosols produced earlier in pyrolysis.

Attempts to model the propagating pyrolysis reaction in wood particles have been confounded by the complexity of coupled reaction and transport phenomena models and the comparatively limited availability of reaction/transport parameters.[59] For example, reactions leading to local phase change between solid, liquid, and gas in the pyrolysis zone (Figure 6.1a) complicate prediction of intra-particle heat transfer, since model parameters including thermal conductivity, heat capacity, and latent heats associated with phase transition will change significantly in this region (which also exhibits the largest temperature gradient).[59, 98] All of these

parameters may be a strong function of composition/temperature and depend highly on the local cellular structure, which changes as particles shrink.[107, 108] Moreover, independent measurement of physical properties of the different materials/phases is currently extremely difficult, resulting in a wide range of estimated model parameters in the literature.[59] These limitations have led to a large number of reaction-transport models of particle pyrolysis which do not hold true outside of a narrow window of reaction conditions (initial composition, reaction temperature, particle size, etc.).

The experimental challenge of acquiring a detailed description of particle pyrolysis arises from the small size of wood fibers (1-2 mm), the fast time-scales of the reaction (1-5 seconds), and the compositional complexity of lignocellulose which is difficult to characterize. Existing experimental data sets of wood particle pyrolysis focus primarily on conversion time, reactant weight loss, and lumped-product yields,[59] which do not provide the spatiotemporally-resolved compositional data needed for validation of complex multi-scale models. Additionally, many experimental data sets of pyrolyzing particles, such as thermogravimetric analysis (TGA), utilize low heating rates with only moderate rates of temperature change ($1 - 150$ °C min^{-1}) not reflective of fast pyrolysis conditions ($>10^3$ °C min^{-1}). In contrast, spatially-resolved temperature profiles of wood particles have been collected (requiring particles as large as two-to-five centimeters), but they are unable to achieve sub-millimeter spatial resolutions necessary for tracking pyrolysis reaction zones.[109] A recent review of pyrolysis modeling by Di Blasi states that "significant effort, in both theoretical and experimental research activities, is still required to formulate and validate truly comprehensive models."[59] For this reason, overcoming the experimental challenges required to generate a data set of composition within reacting particles has recently been identified by us as one of the major fundamental challenges of biomass pyrolysis.[98]
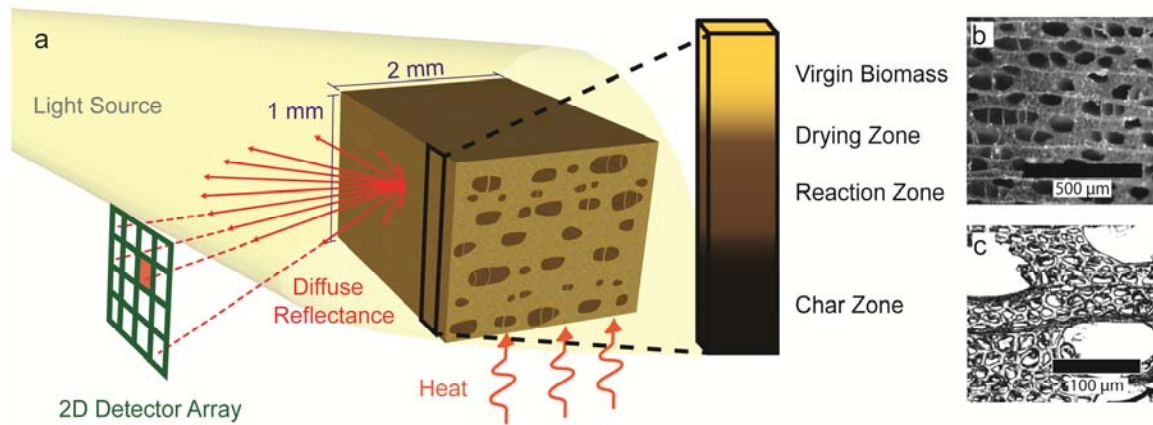
Figure 6.1 Diffuse Reflectance in situ Spectroscopy of Particles. (a) Fast pyrolysis experimental setup with a cutaway demonstrating the zones that exist during biomass pyrolysis at one moment in time, and bright field micrographs of yellow poplar structure (b) at 5x and (c) 50x magnification.

In this work, we introduce a robust wood fiber pyrolysis model based on data from a novel experimental reflectance technique capable of characterizing the carbohydrate fractions within a wood particle in both position and time at reaction conditions relevant to fast pyrolysis of biomass. The technique relies on experimental design (described in section 6.2) leading to one-dimensional heat transfer through yellow poplar (*Liriodendron tulipifera*) particles. In conventional fluidized bed reactors, wood particles are heated uniformly by gas convection such that the pyrolysis reaction front is not externally visible. However, the introduction of a heated surface for direct ablation of wood particles allows for significantly faster particle heating (relative to gas convection) which leads to one-dimensional heat transfer within the wood particle and a visible reaction front on the external particle surface as depicted in Figure 6.1a.

Direct observation of the pyrolysis reaction front on the external particle surface allows for compositional characterization by diffuse reflectance. Diffuse reflectance of visible and near infrared light (400 nm – 2500 nm) on particle surfaces has been used for characterization of woody biomass samples.[110-112] The characterization of wood chip composition, including initial lignin content and breakdown of sugars, has been demonstrated using only the 800-1100 nm spectrum.[113] Similarly, more general characterization of composition is available within the

visible spectrum region, where lignin (highly absorptive) and carbohydrates (highly reflective) are easily distinguished.[114, 115] The distinct absorptive differences between lignin, carbohydrates (five- and six-carbon sugar-based biopolymers), and char over a broad range in the visible spectrum allows for characterization of moving or reacting wood fibers with limited spectral filtering.[111]

In the technique introduced here (Figure 6.1), Spatiotemporally-Resolved Diffuse Reflectance in situ Spectroscopy of Particles (STR-DRiSP), visible light (maximum intensity at 900 nm) is applied to the external side surface of a yellow poplar wood particle (1.0 mm by 2.0 mm by 4.0 mm), and diffusely reflected light is captured using a high-speed, monochrome camera. The overlap of detector absorption range and incident light allows for spectroscopic characterization in the range of 400 – 1100 nm, where significant differences in absorption between lignin/char and carbohydrates are maximized. Rapid response time of the camera (1000 Hz) combined with the capability for focusing on a two-dimensional surface (in focus on the particle surface) allows for the compositional characterization of carbohydrates within reacting particles in both position (ten micron resolution) and time (one millisecond temporal resolution).

The spatio-temporally resolved compositional data set is compared with a robust model for wood fiber pyrolysis at industrial conditions. Carbohydrate compositions within yellow poplar are measured for both position and time over a range of ablative surface temperatures (500 – 700 °C). A reaction-transport model is developed by modifying the kinetic reaction model of Miller & Bellan[116] and combining it with a transport model developed for experiments described here.

6.2 Wood Particle Pyrolysis Experimental Design

Experiments used yellow poplar wood from the same source and cut into blocks 1 mm x 2 mm x 4 mm (height x depth x length) prepared by Forestville Builders & Supply.[117] Wood samples consist of pores (~10 μm in diameter) that run lengthwise through the particle (Figure

6.1c). The micrograph at 5x was collected by boiling the wood in water for one hour before cutting blocks of the desired size (1 mm x 2 mm x 4 mm) and allowing them to dry. This process preserved the structure of the pores at the freshly cut edge. Micrographs were then taken using an Olympus BX51 compound microscope and an Infinity 1 digital camera. Samples for the 50x image were prepared by incasing the wood sample in paraffin wax and using a microtome to cut ten micron thick slices of the wood. During ablative pyrolysis experiments, the wood particles were placed such that the pores were parallel to the heating apparatus and orthogonal to the imaging detector array. Yellow poplar was composed of cellulose (56.75%), hemicellulose (10.86%), and lignin (23.63%) with the remainder comprised primarily of water, ash, etc. (Table 6.1). Compositional characterization of the virgin biomass was conducted by V-Labs INC (Covington Louisiana). The density (573 kg m^{-3}) of the yellow poplar samples was determined by weighing the sample and measuring the volume using a caliper.

Table 6.1 Initial composition of the yellow poplar wood particle.

Compound	Weight Percent
Cellulose	56.75
Klason Lignin	18.38
Hemicellulose	10.86
Acid Soluble Lignin	5.25
Water	3.37
Nitrogen (as protein)	1.10
Ash	0.24
Other	4.05

Pyrolysis experiments were performed on a custom built ablative pyrolysis apparatus, which consisted of a cylindrical steel block (12.8 mm x 28.8 mm; height x diameter) that was heated by two cylindrical ceramic heating cartridges placed within the body of the steel cylinder (Figure 6.2a). To ensure pyrolysis (non-oxidative) conditions, a glass bell jar was suspended above the steel cylinder supplying a continuous flow of nitrogen (~13 L min^{-1}) over the steel

cylinder and wood particle. A high speed camera (Phantom V7/Miro) with long working distance optics was placed to focus on the wood particle surface and record the evolution of the pyrolysis reaction. The source of applied light was a high intensity halogen lamp (250 W, 120 V, 3300 K tungsten filament) which was directed towards the wood particle such that prior to pyrolysis, the wood particle reflected the light, saturating the detectors (white). The orientation of the halogen lamp (light source) is shown in Figure 6.2b and 6.2c. After pyrolysis, the wood sample was no longer reflective and resulted in a low sensor response (black).
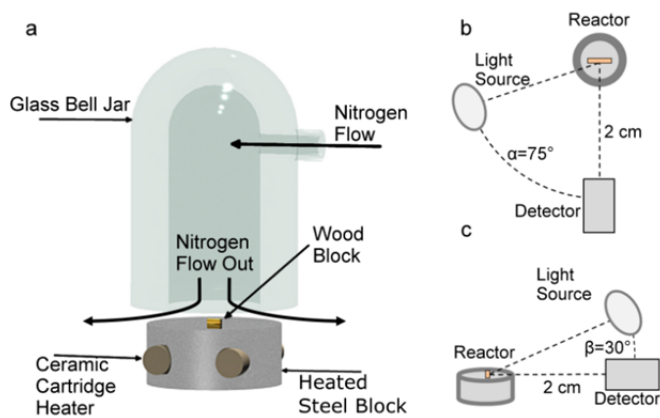
Figure 6.2 Fast pyrolysis experimental reactor design. (a) Front face view of the reactor setup. A steel block was heated using ceramic cartridge heaters, while nitrogen passed over the steel block inside a glass bell jar. Wood particles were placed on the heated steel surface at the start of the experiment, and the subsequent pyrolysis behavior was captured with spectroscopy. (b) Overhead view of the source/sample/detector arrangement. (c) Side view of the source/sample/detector arrangement.

Experiments were conducted by first heating the steel block to a constant reaction temperature (500, 600, 700 °C) while nitrogen was directed over the steel cylinder. Once the steel block reached the desired reaction temperature (monitored using a thermocouple imbedded within the steel cylinder), a wood particle was placed on the heated surface and the reaction was allowed to proceed to completion (i.e. until no change in height or reflectance intensity was observed). This resulted in a heating rate of approximately 0.2 MW m^{-2}, as determined by balancing the heat flux at the interface between the wood particle and the heated steel surface. Additionally, total weight loss caused by pyrolysis was determined by weighing each wood particle prior to and after

pyrolysis. In some cases, the wood particle moved on the surface from the convective flow of the nitrogen purge gas; these runs were discarded.

STR-DRiSP data sets were analyzed using the National Institute of Health (NIH) program ImageJ[118] by measuring the intensity of the light reflected from the face of the wood particle. The intensity of the reflected light ranged from 0 to 255 (arbitrary units) where 0 intensity corresponds to a completely black surface and 255 to white. Data were collected at one millisecond intervals and then analyzed at 200 millisecond increments until the wood particle reaction went to completion. Ten runs were performed for each considered temperature (500, 600, 700 °C). The resulting data were averaged by taking a selected vertical position relative to the surface on the wood particle and averaging the corresponding spectral intensity data for each of the ten experimental runs. The resulting spectral intensity data were then converted to percentage of unreacted carbohydrate using the methods described in section 6.3.

6.3 Diffuse Reflectance Measurements

Experimental conditions were designed to capture the compositional transition from carbohydrate-rich biomass feedstock (cellulose and hemicellulose) to carbon rich char. The technique employed here utilizes diffuse reflectance due to its relative ease in distinguishing between the key components in the visible and near infrared regions. Due to the Lambertian nature of wood fibers (surface roughness on the order of the wavelengths of light) it is appropriate to neglect the presence of specular reflectance and assume that all observed light is from diffuse reflectance.[119]

Figure 6.3a shows the percent of incident light that is reflected by the three dominant constituents of biomass (cellulose, hemicellulose, and lignin) and the primary solid pyrolysis product (char). Cellulose was purchased from Alfa Aesar (Part Number: A17730), xylose was purchased from Sigma Aldrich (Part Number: X1500), lignin was obtained from the Kraft process, and char was produced by pyrolyzing yellow poplar at 500 °C as described previously.

All diffuse reflectance measurements were conducted using a Shimadzu UV-3600 (UV-Vis-NIR spectrometer) with a Harrick Scientific Praying Mantis assembly for capturing diffusely reflected light. The baseline (100% reflectance) was measured using a spectrolon disk and the reflectance spectrum for each sample was obtained by lightly covering the spectrolon disk with the desired powder sample. All diffuse reflectance measurements were collected over the spectral range of 350 nm to 3200 nm and were conducted at room temperature in air.

Figure 6.3a presents the spectral range of the high-speed camera detector (detector specific data provided by Vison Research, an AMETEK company), demonstrating the selective detector response to excitement from incident light in the range of 9,000 - 25,000 cm^{-1} (400 – 1100 nm). The intensity of the 3300 K tungsten light source (a black body radiator) was calculated using Planck's Law and is represented in Figure 6.3a. From the overlap of these two curves, it is clear that the dominant detection region is between 9,000 - 25,000 cm^{-1} where the light source emits and the detector is sensitive to light. Figure 6.3a shows cellulose and xylose (an approximation of hemicellulose) as highly reflective within this dominant detection range, while lignin and char are highly absorptive, indicating the ability to use diffuse reflectance to differentiate the two classes of compounds.

This contrast between the carbohydrates and the char/lignin species is made even starker when examining the predicted spectral response of the camera to the different species. When light reflected from the wood particle reaches the detector, an electrical response is triggered and the relative response is sensitive to the wavelength of light, which is demonstrated by the spectral response curve (Figure 6.3a). The predicted detector response, R^λ, is the product of the spectral response of the detector, $R^\lambda_{spectral}$, (Figure 6.3b) and the incident power observed by the detector at a particular wavelength, P^λ_{in}, to give, $R^\lambda = R^\lambda_{spectral} * P^\lambda_{in}$. If it is assumed that the incoming power is proportional to the total incident light and the diffuse reflectance of a particular sample,

r^λ, then the electrical response of the detector can be described by Equation 6.1 where λ is the wavelength of light, h is Planck's constant, c is the speed of light, and k_B is Boltzmann's constant,

$$R^\lambda \propto \frac{R^\lambda_{spectral} r^\lambda}{\lambda^5 \exp\left(\frac{hc}{\lambda k_B T_{3300}}\right) - 1}$$ (6.1)

The detector response to cellulose, xylose, lignin and char are predicted using Equation 6.1 and shown graphically in Figure 6.3b. This data again shows that the predicted detector response by the STR-DRiSP technique due to carbohydrates is overwhelmingly dominant relative to the response of the highly absorptive lignin and char in the visible and near-IR regions.

The diffusely reflected light from STR-DRiSP can be directly converted into a carbohydrate composition by assuming that the observed reflected light is a linear combination of the individual components where r_i^λ is the diffuse reflectance and X_i is the mass fraction of species i respectively,

$$r^\lambda = r^\lambda_{cell} X_{cell} + r^\lambda_{hemi} X_{hemi} + r^\lambda_{lignin} X_{lignin} + r^\lambda_{char} X_{char} R^\lambda$$ (6.2)

This assumption is verified by calculating the predicted detector response of yellow poplar (Equation 6.1) from diffuse reflectance spectroscopic data obtained for ball milled yellow poplar ($r^\lambda = r^\lambda_{wood}$). This is directly compared against the linear approximation for the experimental system here by substituting Equation 6.2 into the detector response relationship (Equation 6.1), to obtain the theoretical predicted detector response for the sum of the components. Using the measured diffuse reflectance of cellulose, xylose, and lignin (Figure 6.3a) with the known mass fractions of each of the three components in the yellow poplar sample (Table 6.1), the actual and theoretical detector response for yellow poplar is shown in Figure 6.3c as a parity plot; this comparison demonstrates good agreement by accurately predicting the reflectance of a virgin wood sample. The linear combination of the component reflections are shown to approximate the

predicted detector response for the yellow poplar, validating the ability of the linear combination model to accurately describe the experimental system.
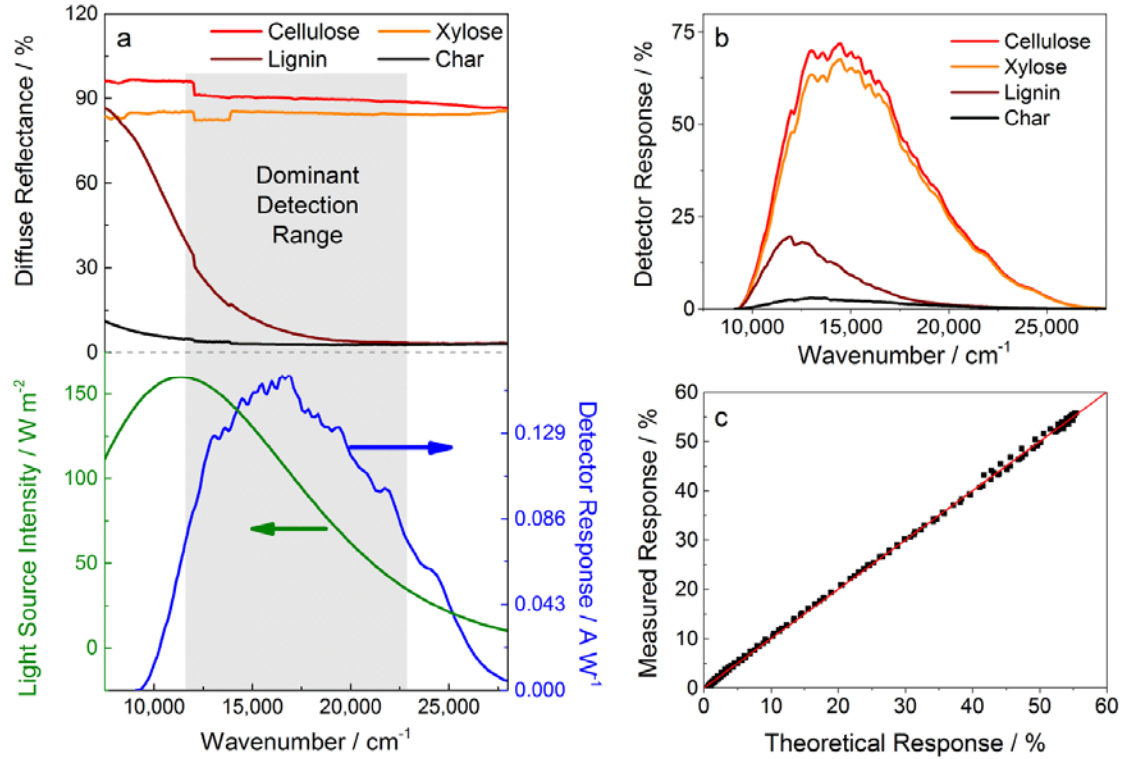
Figure 6.3 Diffuse reflectance spectroscopy. (a). Diffuse reflectivity of the components of wood shows a distinct difference in reflectivity within the range of the light source intensity, and the detector response. (b) Electrical response of the camera detector to different wood components and pyrolysis products shows a strong response to cellulose and xylose. (c) Parity plot demonstrating the effectiveness of modelling the reflectance of wood using a simple linear combination model of the components of wood.

Substituting Equation 6.2 into Equation 6.1 and integrating over all wavelengths for each pure component species data set ($X_{j=i} = 1, X_{j \neq i} = 0$) allows for the determination of a response factor (α_i) for each individual component i (i.e. cellulose, xylose, lignin, and char) to be calculated for the STR-DRiSP system,

$$\alpha_i = \int_0^\infty R^\lambda \, d\lambda \qquad (6.3)$$

Equation 6.3 can then be reduced to the total observed response at each pixel, R_t, (corresponding to the grayscale experimental pyrolysis data) by,

$$R_t = \alpha_{cell}X_{cell} + \alpha_{hemi}X_{hemi} + \alpha_{lignin}X_{lignin} + \alpha_{char}X_{char} \tag{6.4}$$

Utilizing this analysis, we are able to convert one-dimensional spatially resolved experimental data to carbohydrate mass fraction by using the following equation where I_{carb} is the Intensity measured at a specific position and time and I_{max} and I_{min} are the maximum and minimum observed intensities.

$$X_{carb} = \frac{I_{carb} - I_{min}}{I_{max} - I_{min}} \tag{6.5}$$

6.4 Computational Model

The pyrolysis experiments presented here were simulated using the computational fluid dynamics (CFD) software COMSOL Multiphysics[TM], version 4.2. The major simplifying assumptions made in modeling the system are: (a) the wood particle is treated as a non-porous solid;[120] (b) wood is in good thermal contact with the surrounding gas;[120] (c) there is instantaneous outflow of volatile and tar products;[120] (d) crack formation in the wood particle is not considered;[120] (e) the thermophysical properties of the wood particle vary linearly between virgin wood and char as the virgin wood is consumed and char is formed;[120] (f) reaction intermediates have the same properties as virgin wood;[116] (g) secondary tar cracking reactions are neglected due to high nitrogen flow rate.[116]

6.4.1 Transport Model

The experiment was modeled as a two-dimensional system consisting of three distinct domains: (1) a glass bell jar, (2) a nitrogen atmosphere, and (3) a shrinking wood particle with anisotropic material properties. The system geometry, dimensions, and nitrogen flow rate correspond to measurements of the experimental apparatus. Thermophysical properties for the

glass bell jar and nitrogen atmosphere were assigned from COMSOL's built-in material database as silica glass and nitrogen, respectively, and the properties of virgin wood and char are defined in Table 6.2. For consistency, the thermophysical properties for wood and char were gathered from Mehrabian et al.,[121] except for the density of yellow poplar (measured in this experiment), and the heat capacity of wood.[122] An expression different from that of Mehrabian et al. was assigned for the heat capacity of wood (see Table 6.2), because Mehrabian et al. neglect water content; and their value is based on a specific type of wood (spruce) with dissimilar properties to yellow poplar.

The transport model is defined by the following governing equations for energy, continuity, and motion (motion applies only in the nitrogen domain). The energy conservation equation is given as:

$$\rho C_p \frac{\partial T}{\partial t} + \rho C_p \bar{v} \cdot \nabla T = \nabla \cdot (k \nabla T) + Q \tag{6.6}$$

The first term represents the accumulation of energy; the second term is convective heat transfer (applies only in the nitrogen domain); the third term represents conductive heat transfer; and Q is a heat source term accounting for the heats of reaction and the heat of vaporization of water. For the glass and nitrogen domains $Q = 0$ as there is no reaction within these domains. Within the wood domain, Q is defined as:

$$Q = \frac{\rho}{m_{block}} \left[\Delta H_2 \left(-m_{Acell} k_2^C - m_{Ahemi} k_2^H - m_{Alig} k_2^L \right) \right. \\ \left. + \Delta H_3 \left(-m_{Acell} k_3^C - m_{Ahemi} k_3^H - m_{Alig} k_3^L \right) + \Delta H_{H_2O} \left(-m_{H_2O} k_{H_2O} \right) \right] \tag{6.7}$$

where the meaning of each kinetic and mass fraction parameter is described in section 2.6. The equation of continuity is:

$$\frac{\partial \rho}{\partial t} + \nabla \cdot (\rho \bar{v}) = 0 \tag{6.8}$$

71

The second term, representing the rate mass is added by convection, only applies to the nitrogen domain. The equation of motion, which also only applies in the nitrogen domain, is:

$$\rho\frac{\partial\bar{v}}{\partial t} + \rho(\bar{v}\cdot\nabla)\,\bar{v} = \nabla\cdot\left[-p\bar{I} + \mu\left(\nabla\bar{v} + (\nabla\bar{v})^{T}\right) - \frac{2}{3}\mu(\nabla\cdot\bar{v})\bar{I}\right] \qquad (6.9)$$

The first term represents the rate of increase in momentum; the second term is the rate momentum is added by convection; and the right hand side of the equation accounts for the rate momentum is added by molecular transport.

6.4.2 Boundary Conditions

The boundary conditions for Equations 6.6 through 6.9 are:

No slip on all solid surfaces:

$$\bar{v} = 0 \qquad (6.10)$$

Constant velocity at N_2 inlet:

$$\nabla_t \cdot \bar{v} = 0 \qquad (6.11)$$

Laminar flow at N_2 inlet:

$$L_{entr}\nabla\cdot\left[-p_{entr}\bar{I} + \mu\left(\nabla\bar{v} + (\nabla\bar{v})^{T}\right)\right] = p_{entr}\bar{n} \qquad (6.12)$$

Outlet condition:

$$p = p_0 \qquad (6.13)$$

Thermal insulation of gas inlet:

$$-\bar{n}\cdot(-k\nabla T) = 0 \qquad (6.14)$$

Convective cooling of bell jar in air:

$$-\bar{n}\cdot(-k\nabla T) = h_{air}(T_{ext} - T) \qquad (6.15)$$

To account for imperfect thermal contact at the interface between wood and the heated steel block the following heat flux boundary condition was applied along that interface:

$$-\bar{n} \cdot \left(-\bar{k}\nabla T\right) = h_{block}(T_{block} - T) \quad (6.16)$$

Di Blasi's review of pyrolysis modeling literature[59] provided a range of values for heat transfer coefficients used in modeling fast pyrolysis systems. To choose the heat transfer coefficient for our model, we examined the results of simulations with a steel block temperature of 600 ˚C and heat transfer coefficients within the range reported by Di Blasi (between 80 and 1000 W m^{-2} K^{-1}). A heat transfer coefficient of 400 W m^{-2} K^{-1} resulted in the best fit to experimental data and was used in all further simulations. Along all of the surfaces of the heated steel block exposed to nitrogen gas the boundary condition is:

$$T = T_{block} \quad (6.17)$$

The bell jar rests on two steel supports, which are in contact with the heated steel block, and these heat the bottom surface of the bell jar. The temperature at this surface was estimated to be 90% of the steel block temperature due to convective heat losses along the length of the supports.

$$T_{bell\ jar\ bottom} = 0.9T_{block} \quad (6.18)$$

These initial conditions apply to all domains in the system:

$$p_0 = 1\ atm \quad (6.19)$$

$$T_0 = 293.15\ K \quad (6.20)$$

The experimental technique used in this study allowed us to observe the shrinkage of the wood particle with time at each steel block temperature (Figure 6.4a). While many pyrolysis models in the literature ignore particle shrinkage, we chose to prescribe the experimentally observed shrinkage into the model geometry. This was accomplished by defining a moving mesh,

which adjusts the z-position of the top boundary of the wood domain with time according to an equation derived by fitting the experimentally observed shrinkage for each different steel block temperature.

6.4.3 Pyrolysis Kinetics Model

In choosing a set of published kinetic parameters for the model, we required that the selected reaction kinetics allow calculation of the mass fractions of each solid pseudo-component (cellulose, hemicellulose, and lignin) and char. Modeling the fractions of individual solid components allowed us to tie the model directly to experimental observations of the changing composition of solid carbohydrate. Unfortunately, most kinetic parameters reported in the literature for biomass pyrolysis are derived from TG or DTG curves, based on measurements of total sample mass, and therefore kinetic parameters can only be reported for the volatile fraction of each pseudo-component. These "devolatilization mechanisms" do not provide an accurate means of tracking the behavior of solid pseudo-components, although relations are usually provided for calculating the final yield of char.
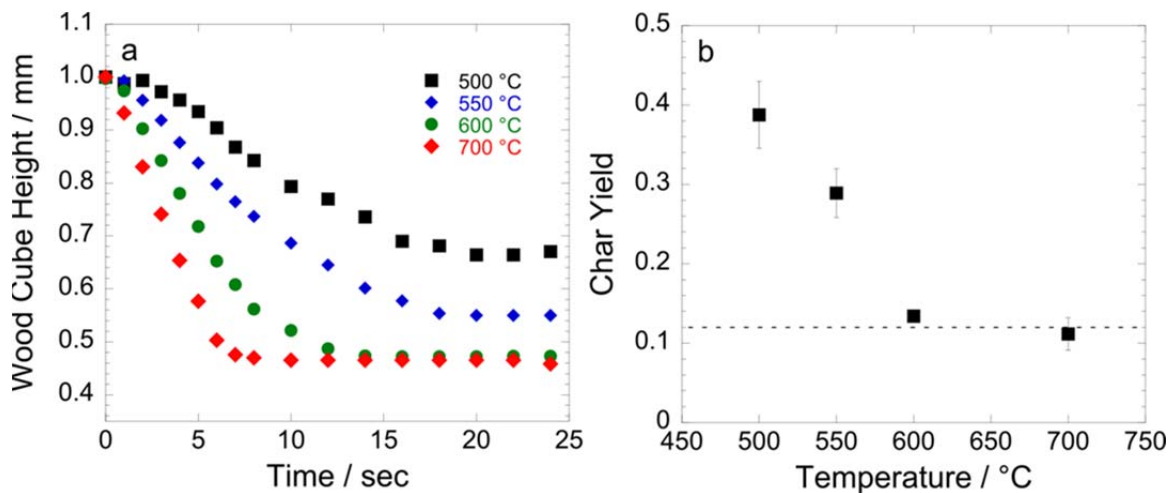
Figure 6.4 Particle shrinkage and mass loss. (a)The average yellow poplar particle height for varying reaction temperatures, and (b) the average fraction of the initial wood particle mass which remains as char and ash after completion of the pyrolysis reaction; this value reaches a plateau at approximately 0.12 (dashed line).

Table 6.2 Physical parameters used in the CFD simulation.

Density	Value	Units	Reference
Yellow poplar	573	[kg m^{-3}]	Expt
Char	200	[kg m^{-3}]	[121]

Thermal conductivity

Wood (z-axis)	$(0.129 - 0.049X_{H_2O})(1 + T[°C](0.986 + 2.695X_{H_2O})(2.05 + 4X_{H_2O}) \times 10^{-3})$	[W m^{-1} K^{-1}]	[121]
Wood (y-axis)	$2.5k_z$	[W m^{-1} K^{-1}]	[121]
Char	0.071	[W m^{-1} K^{-1}]	[121]

Heat capacity

Wood	$1000[(0.1031 + 0.003867T + 4.18X_{H_2O})(1 + X_{H_2O})^{-1} + X_{H_2O}(6.191 + 0.0236T - 0.0133X_{H_2O})]$	[J kg^{-1} K^{-1}]	[122]
Char	$420 + 2.09T + 6.85 \times 10^{-4}T^2$	[J kg^{-1} K^{-1}]	[121]

Heat transfer coefficient (wood-steel interface)

h	400	[W m^{-2} K^{-1}]	Fit

Heat of reaction

ΔH_1	0	[kJ kg^{-1}]	[116]
ΔH_2	255	[kJ kg^{-1}]	[116]
ΔH_3	-20	[kJ kg^{-1}]	[116]
ΔH_{H2O}	2440	[kJ kg^{-1}]	[123]

Reaction rate constants	A [s^{-1}]	E [kJ mol^{-1}]	
k_1^C	2.8×10^{19}	242.4	[116]
k_1^H	2.1×10^{16}	186.7	[116]
k_1^L	9.6×10^8	107.6	[116]
k_2^C	3.28×10^{14}	196.5	[116]
k_2^H	8.75×10^{15}	202.4	[116]
k_2^L	1.5×10^9	143.8	[116]
k_3^C	1.3×10^{10}	150.5	[116]
k_3^H	2.6×10^{11}	145.7	[116]
k_3^L	7.7×10^6	111.4	[116]
k_{H_2O}	5.13×10^{10}	88	[123]

Miller & Bellan published the most complete reaction scheme that allows calculation of the mass fractions of each solid pseudo-component.[116] Their scheme applies the skeleton of the well-known Broido-Shafizadeh model for cellulose pyrolysis to all three pseudo-components (cellulose, hemicellulose, and lignin). In this scheme, virgin pseudo-components react to form

"active intermediates" (Reaction 1), which decompose into tar (Reaction 2) or char plus non-condensable gases (Reaction 3). Two additional kinetic schemes[73, 124] were modeled but failed to reproduce the decomposition rates and times observed in our experimental results due to their lower rates of cellulose decomposition, so all simulation results presented are based on the scheme of Miller & Bellan. Reaction rate constants are determined using the Arrhenius equation with the values in Table 6.2.

$$k_i = A_i \exp\left[-\frac{E_i}{RT}\right] \tag{6.21}$$

The consumption of pseudo-components and formation of "active intermediates" is described by the following equations:

$$\frac{\partial m_i}{\partial t} = -k_1^s m_i \tag{6.22}$$

$$\frac{\partial m_j}{\partial t} = k_1^s m_i - k_2^s m_j - k_3^s m_j \tag{6.23}$$

where i = (cellulose, hemicellulose, lignin),

j = ($A_{cellulose}$, $A_{hemicellulose}$, A_{lignin}) in which A means "active"

s = (cellulose, hemicellulose, lignin) corresponding to the

rate constants in Table 6.2

All extractives are included in the mass of hemicellulose.[116, 125] Mass conservation equations for the three lumped products are:

$$\frac{\partial m_{char}}{\partial t} = 0.35k_3^C m_{Acell} + 0.6k_3^H m_{Ahemi} + 0.75k_3^L m_{Alig} \tag{6.24}$$

$$\frac{\partial m_{gas}}{\partial t} = 0.65k_3^C m_{Acell} + 0.4k_3^H m_{Ahemi} + 0.25k_3^L m_{Alig} \tag{6.25}$$

$$\frac{\partial m_{tar}}{\partial t} = k_2^C m_{Acell} + k_2^H m_{Ahemi} + k_2^L m_{Alig} \tag{6.26}$$

The importance of accounting for the evaporation of water during particle drying in comprehensive pyrolysis models has been demonstrated repeatedly[59, 120, 121, 125], therefore we added water as another reactant in our reaction scheme following the treatment of Bryden, Ragland, & Rutland.[123]

$$\frac{\partial m_{H_2O}}{\partial t} = k_{H_2O} m_{H_2O} \tag{6.27}$$

6.4.4 Solution Strategy

COMSOL uses the finite element method to solve the system of model equations based on a user-defined mesh. The final mesh was determined by shrinking the mesh element size in each domain until the solution at specific coordinates in the wood particle did not change significantly with further mesh refinement. This optimization was done for a steel block temperature of 700 °C to account for the simulation with the steepest temperature and concentration gradients. Complete simulations, covering 24 seconds of observed experimental time, took approximately six days each to run on a Linux workstation with two four core 2.27 GHz Intel® Xeon® E5607 processors and 5.7 GB of memory. Mass fractions along the two external faces of the simulated wood particle were averaged and compared with experimental data.

Additionally, a sensitivity analysis for the model was performed by varying the value of 20 different model parameters to explore which parameters had the greatest control on the results of the simulation. Rate constants were varied by one order of magnitude up (+) or down (-), and both the heats of reaction and char formation mass ratios were varied by 20%. Thermophysical parameters of wood and char span the range of published literature values. Parameter values were varied independently and used to run three seconds of the 600 ˚C steel block simulation, which was then compared to the "base case" at 600 ˚C. Sensitivity analysis simulations were limited to three seconds to avoid unnecessarily long computation times while still allowing the entire simulated wood particle to begin reacting. All parameters were varied except: (1) the heat transfer

coefficient between wood and the steel block, because it was used to fit the experimental data as described earlier; (2) the initial composition of the wood, because this was measured analytically; (3) the heat of vaporization of water, because its value is well established; and (4) the dimensions of the wood particle and experimental apparatus.

6.5 Particle Shrinkage

Figure 6.5 shows the evolution of a visible reaction front during the pyrolysis of a wood particle. Wood is completely reflective prior to the start of the reaction, but upon contact with the heated surface the base of the wood particle begins to darken (i.e. is no longer reflective). As the reaction progresses, the reaction front (defined as the transition from reflective to absorptive) travels from the base of the particle to the top. In addition to the loss of reflectivity, the particle also shrinks in size over the course of the reaction. However, the particle continues to shrink after the majority of the carbohydrates in the particle have reacted (true for all reaction temperatures), which implies that particle shrinkage is not driven completely by carbohydrate pyrolysis. Davidsson et al. has shown that at low temperatures (< 500 °C) shrinkage does not begin until after 60% of the biomass has been converted at which point much of the cellulose has been consumed.[126] Davidsson et al. goes on to postulate that the decomposition of the rigid structures formed around the microfibrils by lignin and hemicellulose char account for the shrinkage of biomass particles during pyrolysis.[126] In our work, we find that the wood particle's transition from reflective to absorptive is caused by the consumption of cellulose and hemicellulose (carbohydrates). Since the particle continues to shrink after all carbohydrates have been consumed, our work agrees with Davidsson et al. that carbohydrate conversion is not the sole cause of particle shrinkage. Rather, the breakdown of lignin, which has been shown to react slowly over a large range of temperatures,[70] likely contributes to the shrinkage phenomenon. As heat is transferred upward through the particle, the visible reaction front (loss of reflectivity)

78

would be accompanied by another reaction front, invisible to our STR-DRiSP technique, corresponding to the decomposition of lignin that would contribute to particle shrinkage.

Particle shrinkage has been tied to the collapse of the native structure within wood particles, which corresponds to breaking down of the solid biomass components as they react to form liquids and gases[126, 127]. Lignin is considered to be a key component in the structural integrity of biomass,[128] suggesting that lignin breakdown is an important aspect of particle shrinkage. Particle shrinkage is also related to the total non-volatilized mass/char yield of the particle (Figure 6.4b). As temperature increases, both total mass loss and total amount of shrinkage increase, while both shrinkage and weight loss reach a plateau at 600 °C. This implies that shrinkage is directly related to the fraction of initial biomass that reacts to form solid char (less char equals more shrinkage) and that there is a minimum yield of char (~12%, asymptotic value, Figure 6.4b) that cannot be decreased by continuing to increase reactor temperatures.
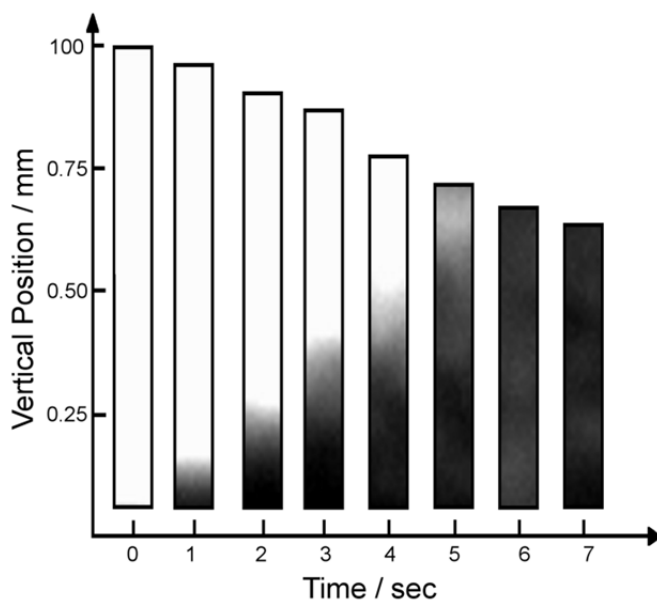
Figure 6.5 Spectral intensity of a reacting yellow poplar wood particle. Raw spectral intensity data collected for a cross section of a yellow poplar wood particle is shown during pyrolysis with a surface temperature of 600 °C at different times. The unreacted wood particle with complete cellulose/hemicellulose content exhibits high spectral intensity (0 seconds, white). A visible reaction front proceeds from the bottom to the top of the particle as it shrinks. After seven seconds, the particle is completely dark consistent with low carbohydrate content.

It is noteworthy that including particle shrinkage in our model is critical to achieving reasonable agreement with experimental data. This is because the high nitrogen flow rate over the wood surface dramatically slows the heating of the upper portion of the particle (because the nitrogen contacting the wood is at a lower temperature than the ablative surface), delaying initiation of the decomposition reactions. Simulations without shrinkage exhibit a lag in predicted carbohydrate consumption compared to the experiment. At short times (1-2 seconds), before the particle has shrunk appreciably, this lag is not observed, but the lag grows with time as the difference in particle height increases between the shrinking-disabled model and the experimentally observed particle. Complete decomposition of carbohydrates within the 24-second simulation time is not observed when shrinking is disabled. The lag described above is eliminated when shrinkage is included in the model, because the driving force for heat transfer increases as the wood shrinks, increasing the speed of the thermal front moving from the bottom to the top of the particle.

In our model, particle shrinkage was achieved by defining a moving mesh that compressed all mesh elements in the wood domain with each time step. Despite the observed accuracy of this coarse approach, there are physically unrealistic aspects of our assumption arising from the fact that lignin decomposition is not uniformly distributed in position or time within the wood particle. In future work it would be interesting to systematically allow shrinking of individual mesh elements, based for example on their lignin mass fraction, so that the entire particle shrinks and warps asymmetrically as observed in experiments. While possible in principle, it is yet unknown if the increased computational cost of the more detailed simulation would be prohibitive, but it is worth considering due to the fact that there are as yet no known predictive shrinkage models for wood particle pyrolysis.

6.6 Experimental Results versus Model Results

Initial reflectance of the wood particle is caused by the presence of the carbohydrates cellulose and hemicellulose. Figure 6.3a shows the highly reflective nature of both cellulose and xylose (a good approximation of hemicellulose), while also demonstrating the highly absorptive nature of lignin and char within the visible and near IR spectrum. The basis for this technique was this difference in reflectivity, which can be used to decouple carbohydrate content from lignin/char and be used to monitor the concentration of carbohydrates both spatially and temporally. Figure 6.3c substantiates this method and shows that the reflectance spectrum of a yellow poplar wood sample can be predicted accurately by a simple linear combination of the reflectance of the three constituents (cellulose, hemicellulose, and lignin) in their pure form.

We apply the above technique to the fast pyrolysis of yellow poplar in order to track the carbohydrate content of the wood particle (Figure 6.6) in both position and time. Figure 6.6 shows the results of applying this technique to the experimental results and compares it to the results of a computational model based on kinetics (gathered from TGA experiments) taken from Miller & Bellan.[116] The experimental and computational results show qualitative and quantitative agreement at short times (1-3 sec) and lower temperatures (500 °C and 600 °C). In all cases the basic trends are observed in the model, with minor discrepancies in the slope and shape of the model curves. However, at a few intermediate time steps, the model and experimental agreement is no longer as accurate. The pyrolysis zone is considerably broader (approximately 50%) in the experimental results when compared to the simulation results, especially at 700 °C. This difference may derive from the reaction kinetics used in the computational model, which were developed from experiments with a slow rate of temperature change (5-80 °C min^{-1}) or from inaccuracies in parameter estimation. This narrowing of the pyrolysis zone by simulation also occurs to a lesser extent for all of the data sets (i.e. the simulations react to completion more quickly than the experimental results). This discrepancy may be an indication that the low temperature kinetics over-predict the speed of pyrolysis reactions at high temperatures.
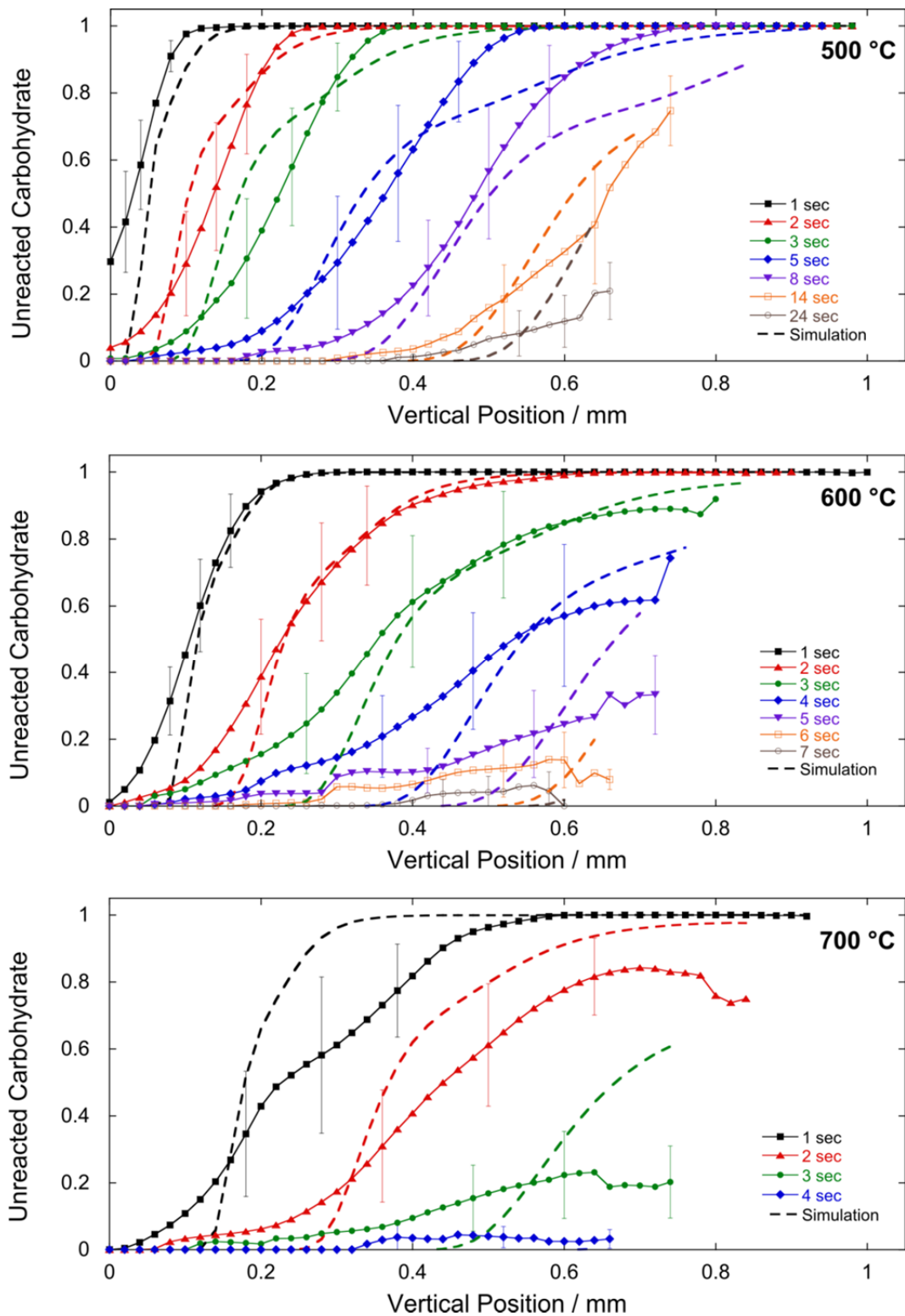
81

Figure 6.6 Spatio-temporally resolved carbohydrate composition profiles of pyrolyzing yellow poplar. Modeling and experimental results of the mass fraction of unreacted carbohydrate content as a function of time and position. Plots depict pyrolysis at 500 °C, 600 °C, and 700 °C.

Sensitivity analysis of the model of equations 5-26 shows that five parameters are important to know accurately, because variation in any of them changes the model results significantly. These parameters are the wood density, wood heat capacity, wood thermal conductivity, and the rate constants of the first reaction in both cellulose and hemicellulose decomposition. Our sensitivity analysis findings are in agreement with previously published work regarding the most important parameters.[59, 125, 129] In our case, all of these parameters except the wood density are general values for "wood" from literature, and are not specific to our yellow poplar. Determining species-specific certainty bounds on these five important parameters will be important for future modeling work, whereas accurate values for other model parameters are lower priority.

We made significant simplifying assumptions by neglecting the porosity of the wood sample and assuming instantaneous outflow of volatiles. Some researchers have chosen to account for the pressure variation due to volatile flow within wood's pores using the Darcy law, especially in less computationally expensive one-dimensional models.[120] Our assumption of a non-porous solid was made in order to reduce the time and computational expense of running such a complicated model. However, including the porosity of wood will become more important in future comprehensive models when particle shrinkage is based on physical mechanisms.
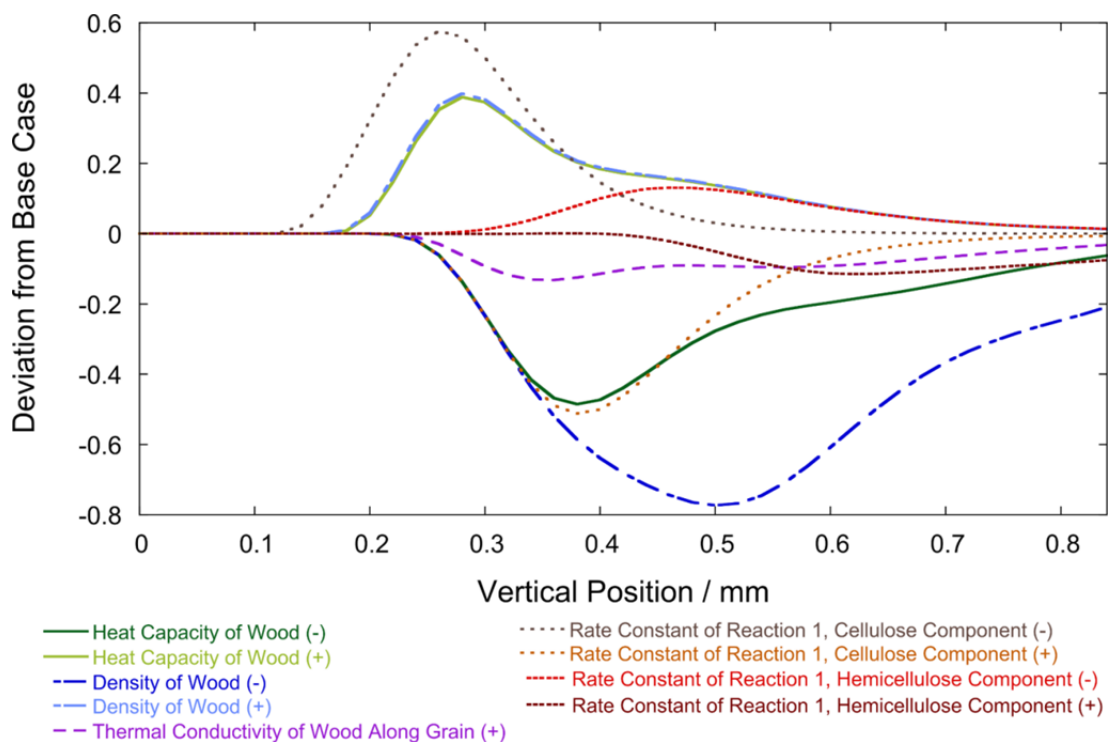
Figure 6.7 Reaction-Transport Model Sensitivity Analysis. Sensitivity of the 600 ˚C steel block simulation to the most important model parameters as a function of position (at three seconds). The deviation is defined as [carbohydrate mass fraction] – [carbohydrate mass fraction]base case.

6.7 Conclusions

We demonstrate and validate a new experimental technique (STR-DRiSP) capable of monitoring biomass composition during pyrolysis both temporally and spatially. Experimental design was provided for reaction of wood particles with one-millimeter thickness by direct ablation with a heated surface, such that heat transfer was overwhelmingly one-dimensional. For these thermal conditions, characterization of the particle surface by spectroscopy was indicative of compositional changes throughout the particle. Spectroscopic characterization of a light source and camera detector along with the reflective properties of lignin, char, cellulose, and xylose supported the method of compositional characterization of carbohydrates with high spatial (ten micron) and temporal (one millisecond) resolution. Carbohydrate compositional profiles were generated for pyrolyzing yellow poplar wood particles at 500, 600 and 700 °C, providing the first

spatio-temporally resolved compositional profiles of reacting biomass particles at industrial conditions.

A comprehensive two-dimensional reaction-transport model of a single particle was developed that presents the most accurate model for wood reaction-transport modeling of wood particles under relevant heating conditions using carbohydrate composition data measured with STR-DRiSP. At lower temperatures the model results are in good agreement with experimental data; discrepancy at higher temperatures was due to the use of lumped kinetic reaction parameters for biomass fast pyrolysis. Given that only two parameters were fit in this pyrolysis model (the heat transfer coefficient and the shrinkage rate), it has utility in a predictive capacity for systems where the shrinkage rate is known or can be estimated. The combination of experimental STR-DRiSP and reaction-transport modeling lays the groundwork for addressing several longstanding challenges in the development of fast pyrolysis technology for biomass: (1) poor understanding of fast pyrolysis transport and reaction kinetics; (2) uncertainty about the mechanisms of particle shrinkage during fast pyrolysis; and (3) high variability in fast pyrolysis reaction-transport models

CHAPTER 7

CONCLUSIONS

7.1 Summary

This thesis investigated the chemistry and mass transport of biomass fast pyrolysis. A wide variety of techniques were used, including thin-film pyrolysis, co-pyrolysis, isotopic labeling, and catalyst-impregnated pyrolysis. Additionally a new spectroscopic technique (STR-DRiSP) capable of monitoring the cellulosic content of a biomass particle under fast pyrolysis conditions was developed in this work.

It was shown that achieving kinetically-limited conditions in biomass fast pyrolysis requires significantly smaller length scales than has been typically used in the literature. Simply using small amounts of material (100 μg) is insufficient as such a sample cannot meet the necessary heating rate required to operate a kinetically-limited pyrolysis reaction. Instead, a new technique is needed to reduce the sample length scale. Thin-film sample preparation addresses this issue by depositing as much as 250 μg of cellulose in a film approximately three microns thick, which falls within the kinetically-limited regime up to 550 °C.

Additionally, secondary reactions (defined as a primary product reacting to produce other products while still in the liquid phase) within liquid intermediate cellulose were investigated. The breakdown of levoglucosan was chosen because it is the most abundant product (as much as 60%) of cellulose pyrolysis. Co-pyrolysis and isotopic labeling studies were conducted which showed that levoglucosan breaks down within the liquid intermediate to form anhydrosugars, pyrans, and light oxygenates by upwards of a factor of six in the case of pyrans. These secondary

reactions are likely present in cellulose pyrolysis as the products formed are also observed in cellulose pyrolysis. It was also shown that hydrogen exchange likely plays an important role in the formation of elimination products from levoglucosan.

Taking advantage of the kinetically-limited nature of thin-film pyrolysis, the effect of reaction temperature on the products of cellulose pyrolysis was studied. It was shown that temperature does not affect the overall yield of furanosic compounds, which suggests that furans are not formed through a secondary levoglucosan breakdown pathway. Rather, furans likely are formed directly from the decomposition of the cellulose chain. Once the 5-membered furan ring is formed, it does not break down; rather, larger molecular weight furan alcohols (such as HMF and 2-furanmethanol) are deoxygenated to form lighter molecular weight furans (such as dimethylfuran). It is also postulated that formaldehyde and CO are co-products of the same mechanism and formic acid is an intermediate in the formation of CO_2, while the differences in product yields between conventional millimeter-scale powder samples and micron-scale thin-films are likely the result of mass transport effects rather than temperature gradients within powder samples.

Since the 5-membered furan ring is stable while its functional groups readily cleaved, the promotion of this chemistry was investigated. Supported metal catalysts were used to influence liquid intermediate cellulose chemistry with a focus on eliminating aldehyde functional group in order to improve bio-oil stability. It was found that palladium catalysts (especially Pd/C) are selective towards decarbonylation of aldehydic furans within the pyrolytic intermediate liquid. It was also determined that silicon dioxide and carbon are suitably inert metal supports with silicon dioxide (silica) as the ideal support for catalyst-impregnated pyrolysis due to its recoverability.

The final part of this thesis a new spectroscopic technique (STR-DRiSP) is developed to monitor cellulosic composition of a biomass particle during fast pyrolysis reactions. STR-DRiSP utilizes a custom built reactor for the direct ablation of a biomass particle with a heated surface, such that heat transfer is overwhelmingly one-dimensional. Using a detector to measure diffuse light reflecting off the particle surface, the compositional of carbohydrates was characterized with high spatial (ten micron) and temporal (one millisecond) resolution. The technique was validated at 500, 600, and 700 °C using an independent model with only two fitting parameter. STR-DRiSP makes it possible to monitor the composition of fast pyrolysis reactions for the first time.

7.2 Future Work

The goal of biomass pyrolysis research is economically competitive biofuels and chemicals derived from lignocellulosic biomass. Developing a greater understanding of the molecular level reaction mechanisms of biomass pyrolysis is required to better optimize industrial pyrolysis reactors. Beyond the work done in this thesis, future work is needed to understand the complex reaction environment within liquid intermediate cellulose, as well within the gas phase and on catalyst surfaces. Additionally, while this thesis focuses on cellulose pyrolysis, hemicellulose and lignin pyrolysis is even less well understood.

The techniques used in this thesis, namely thin-film pyrolysis and isotopiclly-labeled co-pyrolysis, can be utilized to study the reaction mechanisms of hemicellulose and lignin pyrolysis. There remain difficulties in isolating lignin and hemicellulose from woody biomass. Multiple processes exist for isolating lignin; however, these processes yield lignin fractions with varying properties. It is also important to understand the interactions that may take place between

cellulose, hemicellulose, lignin, and their products within in the liquid intermediate. Such studies will require creating samples that accurately mimic the structure of biomass, possibly using 3-D printing techniques, and the ability to generate kinetically-limited (3 – 10 µm) samples from woody biomass.

Understanding the decomposition of biomass to the liquid intermediate is very difficult. Liquid intermediate cellulose/biomass only exists under reaction conditions for 1 – 2 seconds, making characterization of the melt very difficult. *In situ* techniques utilizing IR and UV spectroscopy can monitor the presence of certain functional groups, such as aldehydes or alcohols. However, full characterization of liquid intermediate cellulose will likely require halting the reaction prior to completion and using off-line analysis techniques such as LCMS or H-NMR. This will require extensive engineering work in order to achieve the necessary cooling rates (100 – 500 ms)

In addition to the primary constituents of biomass, there exist trace amounts of inorganics that strongly affect pyrolysis product yields. Understanding how these inorganics directly or indirectly affect pyrolysis chemistry is a crucial step. Such knowledge will be crucial in developing pyrolysis reactors capable of maximizing bio-oil quality and yield as well as in designing pyrolysis catalysts to tune bio-oil properties.

Altering condensed-phase biomass chemistry is a relatively unexplored field. This thesis proves that it is possible to do so using supported metal catalysts. Heterogeneous catalysts offer the ability to reduce oxygen content, reduce bio-oil acidity and instability, increase bio-oil yield, or direct production towards desirable compounds. However, there remain significant hurdles, including catalyst stability, recyclability, identification, and impregnation.

APPENDIX

IDENTIFICATION OF PYROLYSIS PRODUCTS

This appendix present a summary of the methods used to identify the products produced in the previous chapters. Compounds were identified through gas chromatography retention time analysis, mass spectroscopy and by comparison to pyrolysis products reported in previous work. Many compounds, such as furan, levoglucosan, and glycolaldehyde, are straightforward to identify since they have been reported in previous work,[32, 48] produce a clean mass spectrum that compares favorably to established benchmarks and are commercially available. While identification is straightforward for some pyrolysis products, other analytes are more challenging since one or more of these characterization methods is unavailable.

One major component which was challenging to identify is methyl glyoxal. Table S2 shows that methyl glyoxal can be up to six percent of the total product yield. The mass spectrum for the analyte (methyl glyoxal) has three major ions: 72, 56 and 44 mass-to-charge ratio (m/z) with the parent ion (72) indicating the molecular weight. Because of the atomic composition of the biomass starting material, this compound can only contain carbon, hydrogen, and oxygen and the chemical formula must be $C_3H_4O_2$ or $C_4H_8O_2$. The response at 56 m/z likely corresponds to a loss of an oxygen atom (-16 Daltons) while the 44 ion is probably due to a loss of a CO (-28 Daltons). From these ions, it was deduced that the analyte likely has at least one carbonyl group. With an early retention time of 10.5 minutes, the analyte eluted in the range of linear oxygenates. Because all other identified linear oxygenates contained two oxygen atoms, we hypothesized that the unknown compound is a straight chain oxygenate with the formula $C_3H_4O_2$. Using the NIST Mass Spectral Library, compounds with formulas $C_3H_4O_2$ and $C_4H_4O_2$ were examined to find
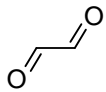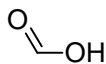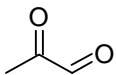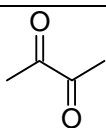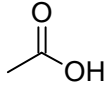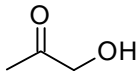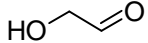
90

possible matches to the unknown compound. From this analysis, a list of possible chemicals was constructed. After testing all compounds on the list, we found that methyl glyoxal had a retention time identical to the analyte. Further evidence is that the mass spectrum for pure methyl glyoxal contains the same major mass spectra ions (72, 56, and 44) as the analyte. Based on this information, the unknown peak at 10.5 minutes was assigned to methyl glyoxal.
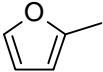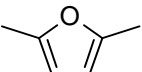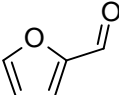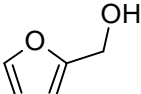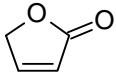
Not all compounds are commercially available for retention time testing and therefore identification relied on mass spectrometry. Three compounds, as indicated in Table S2, were identified through the use of mass spectrometry only. Of these three, two had been identified in previous work: 1,6-anhydroglucopyranose (AGP) and 1,4;3,6-dianhydro-α-D-glucopyranose (DGP).[32, 48] These compounds were easily confirmed with our mass spectrometer. The third compound (retention time of 44.6 minutes) was identified using Mass Spectrometry as 1,2-cyclopentanedione (CPD). The mass spectra for this analyte contained several ions which can easily be produced by CPD fragmentation. The loss of a CHO from CPD results in an ion of 69 Daltons, which we observe. We also observe an ion of 55 Daltons, which could be produced from the loss of a C_2H_3O. Furthermore, the NIST library search program presented CPD as a strong match for the unknown peak over six separate pyrolysis runs. Finally, CPD has a similar structure to 2-hydroxy-3-methyl-2-cyclopenten-1-one (CPD has one less methyl group), a pyrolysis product identified via mass spectrometry and retention time analysis. Based on this evidence, we identify this analyte as CPD.
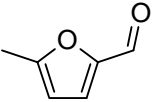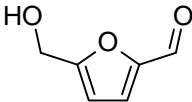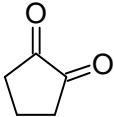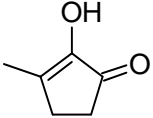
One peak was identified without a strong NIST Mass Spectral Library match or a retention time comparison. This peak, shown in Table S2 (retention time of 69.0 minutes), produces no exact match to the NIST library but analysis of the mass spectra indicates that the
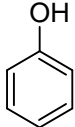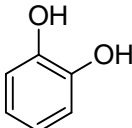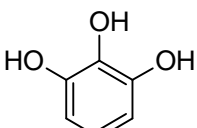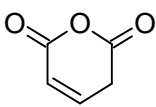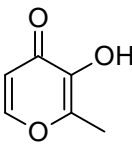
analyte has a molecular weight of 144. Additionally, responses were observed at 126,113,97, 87, 69, and 57 m/z. Shafizadeh and co-workers identify a major product from cellulose pyrolysis as 1,5-anhydro-4-deoxy-D-glycero-hex-1-en-3-ulose (ADGH) using a combination of techniques (H-NMR, IR spectrometry, UV spectrometry, and mass spectrometry).[48] Shafizadeh and co-workers show that ADGH has a molecular weight of 144 Daltons and elutes between levoglucosan and 1,4;3,6-dianhydro-α-D-glucopyranose. ADGH is a six member ring that is similar to glucose except that two water molecules (-36 Daltons) have been removed via dehydration. In our mass spectrometry measurements, we observe several ions which can easily be produced from ADGH fragmentation. From ADGH, the loss of a CH_3O results in an ion of 113 Daltons (which we observe). The loss of a CH_3O and an oxygen results in an ion of 97 Daltons, which we also observe. Finally, we observe an ion of 126 Daltons, which could be produced by ADGH dehydration (-H_2O). The analytes' retention time relative to levoglucosan and 1,4;3,6-dianhydro-α-D-glucopyranose (DGP), coupled with analysis of the mass spectra and the previous work of Shafizadeh, indicates that our analyte is ADGH.
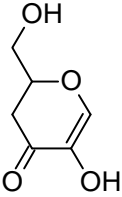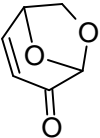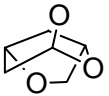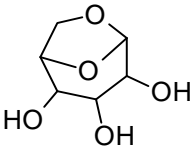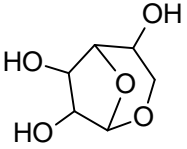
Table A.1 Summary of identified pyrolysis products in powder and/or thin film pyrolysis experiments at 500 $^\circ$C.

Compound	Structure	Ref.	Molar Mass	Major Ion Fragments			Yield [% C]
Permanent Gases							
carbon monoxide	C≡O	-	28				0– 5.6
carbon dioxide	O=C=O	-	44				0.4 – 6.8
Linear Oxygenates							
glyoxal		-	58	Ion	Relative Height	Fragment Lost	0 – 0.2
				58	999	—	
				56	845	- H_2 (-2)	
formic acid		32	46	Ion	Relative Height	Fragment Lost	0.2 – 13.7
				46	999	—	
				45	753	- H (-1)	
methylglyoxal		-	72	Ion	Relative Height	Fragment Lost	1.0 – 6.0
				72	999	—	
				56	389	- O (-16)	
				44	487	- CO (-28)	
2,3 butanedione		-	86	Ion	Relative Height	Fragment Lost	0.1 – 1.3
				86	999	—	
acetic acid		32	60	Ion	Relative Height	Fragment Lost	0.1 – 0.6
				60	734	—	
				45	999	-CH_3 (-15)	
hydroxyacetone		32	74	Ion	Relative Height	Fragment Lost	0 – 2.9
				74	999	—	
				45	293	CHO (-29)	
glycoaldehyde		32	60	Ion	Relative Height	Fragment Lost	0 – 11.5
				60	999	—	
				58	290	- H_2 (-2)	
				56	157	- H_4 (-4)	

Furans							
furan		32	68	Ion	Relative Height	Fragment Lost	0 – 0.6
				68	999	—	
2-methyl furan		32	82	Ion	Relative Height	Fragment Lost	0.2 – 0.7
				82	999	—	
				81	589	- H (-1)	
				53	613	-CHO (-29)	
2,5 dimethyl furan		-	96	Ion	Relative Height	Fragment Lost	0.2 – 1.1
				96	999	—	
				95	946	- H (-1)	
				81	326	-CH$_3$ (-15)	
				53	553	-C$_2$H$_3$O (-43)	
furfural		32	96	Ion	Relative Height	Fragment Lost	0.7 – 2.4
				96	999	—	
				95	953	- H (-1)	
2-furanmethanol		32	98	Ion	Relative Height	Fragment Lost	0.5 – 1.3
				98	999	—	
				97	614	- H (-1)	
				81	747	-OH (-17)	
				69	553	-CHO (-29)	
				53	796	(-45)$^\beta$	
2(5H) furanone		-	84	Ion	Relative Height	Fragment Lost	0.1 – 0.7
				84	507	—	
				55	999	-CHO (-29)	
				54	267	-CH$_2$O (-30)	

				Ion	Relative Height	Fragment Lost	
5-methyl furfural		32	110	110	999	—	0.3 – 0.7
				109	814	- H (-1)	
				57	470	$(-53)^{\beta}$	
				55	389	$(-55)^{\beta}$	
				53	608	$(-57)^{\beta}$	
5-hydroxymethyl-furfural (HMF)		32, 48	126	Ion	Relative Height	Fragment Lost	2.1 – 4.1
				126	593	—	
				125	99	- H (-1)	
				97	999	-CHO (-29)	
				69	327	$(-57)^{\beta}$	
				53	194	$(-73)^{\beta}$	
Cyclopentanes							
1,2-cyclopentanedione$^{\gamma}$		-	98	Ion	Relative Height	Fragment Lost	0.1 – 0.8
				98	999	—	
				69	300	-CHO (-29)	
				55	655	$-C_2H_3O$ (-43)	
2-cyclopenten-1-one, 2-hydroxy-3-methyl		32	112	Ion	Relative Height	Fragment Lost	0.1 – 0.4
				112	999	—	
				83	291	-CHO (-29)	
				69	481	$-C_2H_3O$ (-43)	
				55	473	$(-57)^{\beta}$	

95

Aromatics							
phenol		-	94	Ion	Relative Height	Fragment Lost	0^{α}
				94	999	—	
				66	352	-CO (-28)	
				65	226	-CHO (-29)	
catechol		-	110	Ion	Relative Height	Fragment Lost	0.1 – 0.9
				110	999	—	
				92	111	-H_2O (-18)	
				81	132	-CHO (-29)	
				64	299	(-46)$^{\beta}$	
pyrogallol		-	126	Ion	Relative Height	Fragment Lost	0^{α}
				126	999	—	
				108	259	H_2O (-18)	
				80	305	(-46)$^{\beta}$	
				52	285	(-74)$^{\beta}$	
Pyrans							
2H-pyran-2,6(3H)-dione$^{\gamma}$		-	112	Ion	Relative Height	Fragment Lost	0^{α}
				112	690	—	
				84	707	-CO (-28)	
				56	279	(-56)$^{\beta}$	
				55	999	(-57)$^{\beta}$	
maltol		-	126	Ion	Relative Height	Fragment Lost	0 – 0.6
				126	999	—	
				97	196	-CHO (-29)	
				71	360	(-55)$^{\beta}$	
				55	204	(-71)$^{\beta}$	

Compound	Structure		Ion	Relative Height	Fragment Lost	
1,5-anhydro-4-deoxy-D-glycero-hex-1-en-3-ulose[δ]		48	144	144	846	—	0 – 5.5
				113	217	-CH$_3$O (-31)	
				97	678	(-47)[β]	
				87	999	(-57)[β]	
				69	384	(-75)[β]	
				57	576	(-87)[β]	

Anhydrosugars

Compound	Structure			Ion	Relative Height	Fragment Lost	
levoglucosenone		32	126	98	259	-CO (-28)	0.1 – 3.0
				68	999	(-58)[β]	
				53	946	(-73)[β]	
				51	430	(-75)[β]	
				50	588	(-76)[β]	
1,4;3,6-dianhydro-α-D-glucopyranose[γ]		32, 48	144	144	—	—	0.4 – 2.9
				114	286	-C$_2$HO (-30)	
				70	269	(-74)[β]	
				69	999	(-75)[β]	
				57	453	(-87)[β]	
levoglucosan		32, 48	162	144	—	-H$_2$O (-18)	3 – 56.6
				73	362	(-89)[β]	
				60	999	(102)[β]	
				57	427	(105)[β]	
1,6 Anhydroglucofuranose[γ]		32, 48	162	73	999	(-89)[β]	0.4 – 6.7
				69	309	(-93)[β]	
				61	208	(-101)[β]	
				45	209	(-117)[β]	

[α] Only trace amounts were detected, and do not contribute to the overall carbon balance

[β] Ion fragments could be represented by multiple chemical formulas

[γ] Compund indentified using only mass spec; no pure sample is commercially available

BIBLIOGRAPHY

1.   J. Chow, R. J. Kopp and P. R. Portney, *Science*, 2003, **302**, 1528-1531.
2.   S. Shafiee and E. Topal, *Energy Policy*, 2009, **37**, 181-189.
3.   N. A. Owen, O. R. Inderwildi and D. A. King, *Energy Policy*, 2010, **38**, 4743-4749.
4.   E. I. A. (US), *International Energy Outlook 2013 With Projections to 2040*, Government Printing Office, 2013.
5.   P. M. Cox, R. A. Betts, C. D. Jones, S. A. Spall and I. J. Totterdell, *Nature*, 2000, **408**, 750-750.
6.   K. Caldeira and M. E. Wickett, *Nature*, 2003, **425**, 365-365.
7.   T. P. Hughes, A. H. Baird, D. R. Bellwood, M. Card, S. R. Connolly, C. Folke, R. Grosberg, O. Hoegh-Guldberg, J. B. C. Jackson, J. Kleypas, J. M. Lough, P. Marshall, M. Nystrom, S. R. Palumbi, J. M. Pandolfi, B. Rosen and J. Roughgarden, *Science*, 2003, **301**, 929-933.
8.   M. Eberhard and M. Tarpenning, *Tesla Motors Inc*, **6**, 2006.
9.   A. J. Ragauskas, C. K. Williams, B. H. Davison, G. Britovsek, J. Cairney, C. A. Eckert, W. J. Frederick, J. P. Hallett, D. J. Leak, C. L. Liotta, J. R. Mielenz, R. Murphy, R. Templer and T. Tschaplinski, *Science*, 2006, **311**, 484-489.
10.   K. Sanderson, *Nature*, 2006, **444**, 673-676.
11.   R. D. Perlack, L. L. Wright, A. F. Turhollow, R. L. Graham, B. J. Stokes and D. C. Erbach, Oak Ridge National Laboratory, Oak Ridge, TN, 2005.
12.   R. D. Perlack and B. J. Stokes, Oak Ridge National Laboratory, Oak Ridge, TN, 2011.
13.   R. J. Bothast and M. A. Schlicher, *Applied Microbiology and Biotechnology*, 2005, **67**, 19-25.
14.   J. Hill, E. Nelson, D. Tilman, S. Polasky and D. Tiffany, *Proceedings of the National Academy of Sciences of the United States of America*, 2006, **103**, 11206-11210.
15.   Y. Sun and J. Y. Cheng, *Bioresource Technology*, 2002, **83**, 1-11.
16.   L. R. Lynd, J. H. Cushman, R. J. Nichols and C. E. Wyman, *Science*, 1991, **251**, 1318-1323.
17.   A. Graf and T. Koehler, *An evaluation of the potential for eth-anol production in Oregon using cellulose-based feedstocks. report prepared by the Oregon Of-fce of Energy. Portland, Oregon, USA*, 2000.
18.   M. Wright and R. C. Brown, *Biofuels Bioproducts & Biorefining-Biofpr*, 2007, **1**, 191-200.
19.   J. Koppejan and S. Van Loo, *The handbook of biomass combustion and co-firing*, Routledge, 2012.
20.   A. A. Khan, W. de Jong, P. J. Jansens and H. Spliethoff, *Fuel Processing Technology*, 2009, **90**, 21-50.
21.   J. L. Colby, P. J. Dauenhauer, B. C. Michael, A. Bhan and L. D. Schmidt, *Green Chemistry*, 2010, **12**, 378-380.
22.   P. J. Dauenhauer, B. J. Dreyer, N. J. Degenstein and L. D. Schmidt, *Angewandte Chemie-International Edition*, 2007, **46**, 5864-5867.
23.   J. L. Colby, P. J. Dauenhauer and L. D. Schmidt, *Green Chemistry*, 2008, **10**, 773-783.
24.   S. Rapagna, N. Jand, A. Kiennemann and P. U. Foscolo, *Biomass & Bioenergy*, 2000, **19**, 187-197.

25.	M. J. A. Tijmensen, A. P. C. Faaij, C. N. Hamelinck and M. R. M. van Hardeveld, *Biomass & Bioenergy*, 2002, **23**, 129-152.
26.	M. S. Mettler, A. D. Paulsen, D. G. Vlachos and P. J. Dauenhauer, *Energy & Environmental Science*, 2012, **5**, 7864-7868.
27.	M. S. Mettler, S. H. Mushrif, A. D. Paulsen, A. D. Javadekar, D. G. Vlachos and P. J. Dauenhauer, *Energy & Environmental Science*, 2012, **5**, 5414-5424.
28.	M. S. Mettler, D. G. Vlachos and P. J. Dauenhauer, *submitted*, 2012.
29.	A. D. Paulsen, M. S. Mettler and P. J. Dauenhauer, *Energy & Fuels*, 2013, **27**, 2126-2134.
30.	J. G. Brammer, M. Lauer and A. V. Bridgwater, *Energy Policy*, 2006, **34**.
31.	G. W. Huber, S. Iborra and A. Corma, *Chemical Reviews*, 2006, **106**, 4044-4098.
32.	P. R. Patwardhan, J. A. Satrio, R. C. Brown and B. H. Shanks, *Journal of Analytical and Applied Pyrolysis*, 2009, **86**, 323-330.
33.	J. Lehmann, *Nature*, 2007, **447**, 143-144.
34.	J. A. Mathews, *Energy Policy*, 2008, **36**, 940-945.
35.	C. E. Noon and M. J. Daly, *Biomass & Bioenergy*, 1996, **10**, 101-109.
36.	J. H. Turnbull, *Biomass & Bioenergy*, 1996, **10**, 93-100.
37.	D. Voivontas, D. Assimacopoulos and E. G. Koukios, *Biomass & Bioenergy*, 2001, **20**, 101-112.
38.	A. Demirbas, *Progress in Energy and Combustion Science*, 2004, **30**, 219-230.
39.	A. V. Bridgwater, D. Meier and D. Radlein, *Organic Geochemistry*, 1999, **30**, 1479-1493.
40.	S. Czernik and A. V. Bridgwater, *Energy & Fuels*, 2004, **18**, 590-598.
41.	T. P. Vispute, H. Y. Zhang, A. Sanna, R. Xiao and G. W. Huber, *Science*, 2010, **330**, 1222-1227.
42.	P. J. Dauenhauer, J. L. Colby, C. M. Balonek, W. J. Suszynski and L. D. Schmidt, *Green Chemistry*, 2009, **11**, 1555-1561.
43.	A. R. Teixeira, K. G. Mooney, J. S. Kruger, C. L. Williams, W. J. Suszynski, L. D. Schmidt, D. P. Schmidt and P. J. Dauenhauer, *Energy & Environmental Science*, 2011, **4**, 4306-4321.
44.	O. Boutin, M. Ferrer and J. Lede, *Journal of Analytical and Applied Pyrolysis*, 1998, **47**, 13-31.
45.	F. Shafizadeh, *Advances in Chemistry Series*, 1984, 491-529.
46.	T. R. Carlson, T. R. Vispute and G. W. Huber, *Chemsuschem*, 2008, **1**, 397-400.
47.	D. Mohan, C. U. Pittman, Jr. and P. H. Steele, *Energy & Fuels*, 2006, **20**, 848-889.
48.	F. Shafizadeh, T. T. Stevenson, T. G. Cochran and R. H. Furneaux, *Carbohydrate Research*, 1978, **67**, 433-447.
49.	G. W. Huber and A. Corma, *Angewandte Chemie-International Edition*, 2007, **46**, 7184-7201.
50.	Y. C. Lin, J. Cho, G. A. Tompsett, P. R. Westmoreland and G. W. Huber, *Journal of Physical Chemistry C*, 2009, **113**, 20097-20107.
51.	K. Papadikis, S. Gu and A. V. Bridgwater, *Fuel Processing Technology*, 2010, **91**, 68-79.
52.	C. DiBlasi, *Industrial & Engineering Chemistry Research*, 1996, **35**, 37-46.
53.	G. Varhegyi, E. Jakab and M. J. Antal, *Energy & Fuels*, 1994, **8**, 1345-1352.

54. A. G. W. Bradbury, Y. Sakai and F. Shafizadeh, *Journal of Applied Polymer Science*, 1979, **23**, 3271-3280.
55. N. S. Kaisare, S. R. Deshmukh and D. G. Vlachos, *Chemical Engineering Science*, 2008, **63**.
56. , eds. J. Conti and P. Holtberg, U.S. Energy Information Administration, 2011.
57. Y. Roman-Leshkov, C. J. Barrett, Z. Y. Liu and J. A. Dumesic, *Nature*, 2007, **447**.
58. M. Moliner, Y. Roman-Leshkov and M. E. Davis, *Proceedings of the National Academy of Sciences of the United States of America*, 2010, **107**, 6164-6168.
59. C. Di Blasi, *Progress in Energy and Combustion Science*, 2008, **34**, 47-90.
60. S. L. Madorsky, V. E. Hart and S. Straus, *Journal of Research of the National Bureau of Standards*, 1956, **56**, 343-354.
61. A. Broido and M. A. Nelson, *Combustion and Flame*, 1975, **24**, 263-268.
62. J. P. Diebold, *Biomass & Bioenergy*, 1994, **7**, 75-85.
63. M. J. Antal, *Industrial & Engineering Chemistry Product Research and Development*, 1983, **22**, 366-375.
64. H. Kawamoto, M. Murayama and S. Saka, *Journal of Wood Science*, 2003, **49**, 469-473.
65. T. Hosoya, H. Kawamoto and S. Saka, *Journal of analytical and applied pyrolysis*, 2008, **83**, 64-70.
66. P. R. Patwardhan, J. A. Satrio, R. C. Brown and B. H. Shanks, *Bioresource Technology*, 2010, **101**, 4646-4655.
67. J. B. Paine, III, Y. B. Pithawalla and J. D. Naworal, *Journal of Analytical and Applied Pyrolysis*, 2008, **82**, 42-69.
68. J. B. Paine, III, Y. B. Pithawalla and J. D. Naworal, *Journal of Analytical and Applied Pyrolysis*, 2008, **82**, 10-41.
69. J. B. Paine, III, Y. B. Pithawalla and J. D. Naworal, *Journal of Analytical and Applied Pyrolysis*, 2008, **83**, 37-63.
70. M. J. Antal and G. Varhegyi, *Industrial & Engineering Chemistry Research*, 1995, **34**, 703-717.
71. M. Gronli, M. J. Antal and G. Varhegyi, *Industrial & Engineering Chemistry Research*, 1999, **38**, 2238-2244.
72. M. G. Gronli, G. Varhegyi and C. Di Blasi, *Industrial & Engineering Chemistry Research*, 2002, **41**, 4201-4208.
73. C. Branca, A. Albano and C. Di Blasi, *Thermochimica Acta*, 2005, **429**, 133-141.
74. M. S. Mettler, A. D. Paulsen, D. G. Vlachos and P. J. Dauenhauer, *Green Chemistry*, 2012, **14**, 1284-1288.
75. P. R. Patwardhan, D. L. Dalluge, B. H. Shanks and R. C. Brown, *Bioresource Technology*, 2011, **102**, 5265-5269.
76. J. L. Banyasz, S. Li, J. L. Lyons-Hart and K. H. Shafer, *Journal of Analytical and Applied Pyrolysis*, 2001, **57**, 223-248.
77. J. L. Banyasz, S. Li, J. Lyons-Hart and K. H. Shafer, *Fuel*, 2001, **80**, 1757-1763.
78. R. K. Agrawal, *Canadian Journal of Chemical Engineering*, 1988, **66**, 403-412.
79. R. K. Agrawal, *Canadian Journal of Chemical Engineering*, 1988, **66**, 413-418.

80. J. Piskorz, D. Radlein and D. S. Scott, *Journal of Analytical and Applied Pyrolysis*, 1986, **9**, 121-137.
81. J. Piskorz, P. Majerski, D. Radlein, A. Vladars-Usas and D. S. Scott, *Journal of Analytical and Applied Pyrolysis*, 2000, **56**, 145-166.
82. D. S. Scott, J. Piskorz, M. A. Bergougnou, R. Graham and R. P. Overend, *Industrial & Engineering Chemistry Research*, 1988, **27**, 8-15.
83. M. S. Mettler, A. D. Paulsen, D. G. Vlachos and P. J. Dauenhauer, *Energy & Environmental Science*, 2012.
84. E. Hoekstra, W. P. M. Van Swaaij, S. R. A. Kersten and K. J. A. Hogendoorn, *Chemical Engineering Journal*, 2012, **187**, 172-184.
85. A. V. Bridgwater, *Biomass & Bioenergy*, 2012, **38**, 68-94.
86. R. J. M. Westerhof, D. W. F. Brilman, W. P. M. van Swaaij and S. R. A. Kersten, *Industrial & Engineering Chemistry Research*, 2010, **49**, 1160-1168.
87. V. Agarwal, P. J. Dauenhauer, G. W. Huber and S. M. Auerbach, *Journal of the American Chemical Society*, 2012, **134**.
88. P. J. X. Bai, R.C. Brown, *Journal of Analytical and Applied Pyrolysis*, 2012.
89. R. Vinu and L. J. Broadbelt, *Energy & Environmental Science*, 2012.
90. M. E. Boucher, A. Chaala, H. Pakdel and C. Roy, *Biomass & Bioenergy*, 2000, **19**.
91. S. Crossley, J. Faria, M. Shen and D. E. Resasco, *Science*, 2010, **327**, 68-72.
92. C. Zhao, J. Y. He, A. A. Lemonidou, X. B. Li and J. A. Lercher, *Journal of Catalysis*, 2011, **280**, 8-16.
93. C. L. Williams, C. C. Chang, P. Do, N. Nikbin, S. Caratzoulas, D. G. Vlachos, R. F. Lobo, W. Fan and P. J. Dauenhauer, *Acs Catalysis*, 2012, **2**, 935-939.
94. S. K. R. Patil and C. R. F. Lund, *Energy & Fuels*, 2011, **25**, 4745-4755.
95. M. Salciccioli and D. G. Vlachos, *Acs Catalysis*, 2011, **1**, 1246-1256.
96. F. C. Lanning, B. W. X. Ponnaiya and C. F. Crumpton, *Plant Physiology*, 1958, **33**.
97. E. Epstein, *Annals of Applied Biology*, 2009, **155**, 155-160.
98. M. S. Mettler, D. G. Vlachos and P. J. Dauenhauer, *Energy & Environmental Science*, 2012, **5**, 7797-7809.
99. J. Cho, S. Chu, P. J. Dauenhauer and G. W. Huber, *Green Chemistry*, 2012, **14**, 428-439.
100. J. F. Matthews, M. Bergenstrahle, G. T. Beckham, M. E. Himmel, M. R. Nimlos, J. W. Brady and M. F. Crowley, *Journal of Physical Chemistry B*, 2011, **115**, 2155-2166.
101. V. Agarwal, G. W. Huber, W. C. Conner, Jr. and S. M. Auerbach, *Journal of Chemical Physics*, 2011, **135**.
102. H. B. Mayes and L. J. Broadbelt, *Journal of Physical Chemistry A*, 2012, **116**, 7098-7106.
103. V. Seshadri and P. R. Westmoreland, *Journal of Physical Chemistry A*, 2012, **116**, 11997-12013.
104. D. L. Pyle and C. A. Zaror, *Chemical Engineering Science*, 1984, **39**, 147-158.
105. K. M. Bryden and M. J. Hagge, *Fuel*, 2003, **82**, 1633-1644.
106. V. Mamleev, S. Bourbigot, M. Le Bras and J. Yvon, *Journal of Analytical and Applied Pyrolysis*, 2009, **84**, 1-17.

107. D. Y. Kim, Y. Nishiyama, M. Wada and S. S. Kuga, Syracuse, New York, 2000.
108. M. Bellais, K. O. Davidsson, T. Liliedahl, K. Sjostrom and J. B. C. Pettersson, *Fuel*, 2003, **82**, 1541-1548.
109. J. Cho, J. M. Davis and G. W. Huber, *Chemsuschem*, 2010, **3**, 1162-1165.
110. J. Soukupova, B. N. Rock and J. Albrechtova, *International Journal of Remote Sensing*, 2002, **23**, 3039-3055.
111. M. A. Sanderson, F. Agblevor, M. Collins and D. K. Johnson, *Biomass & Bioenergy*, 1996, **11**, 365-370.
112. S. S. Kelley, T. G. Rials, R. Snell, L. H. Groom and A. Sluiter, *Wood Science and Technology*, 2004, **38**, 257-276.
113. L. Axrup, K. Markides and T. Nilsson, *Journal of Chemometrics*, 2000, **14**, 561-572.
114. R. Bilbao, A. Millera and M. B. Murillo, *Industrial & Engineering Chemistry Research*, 1993, **32**, 1811-1817.
115. P. Malkavaara and R. Alen, *Chemometrics and Intelligent Laboratory Systems*, 1998, **44**, 287-292.
116. R. Miller and J. Bellan, *Combustion Science and Technology*, 1997, **126**, 97-137.
117. Forestville Builders & Supply, http://forestvillebuilders.com/, Accessed July 30, 2013.
118. W. S. Rasband, ImageJ, http://imagej.nih.gov/ij/, Accessed July 30, 2013.
119. M. Jackson, D. Yang and R. Parkin, *Proceedings of the Institution of Mechanical Engineers Part I-Journal of Systems and Control Engineering*, 2007, **221**, 1091-1099.
120. B. Moghtaderi, *Fire and Materials*, 2006, **30**, 1-34.
121. R. Mehrabian, S. Zahirovic, R. Scharler, I. Obernberger, S. Kleditzsch, S. Wirtz, V. Scherer, H. Lu and L. L. Baxter, *Fuel Processing Technology*, 2012, **95**, 96-108.
122. L. F. Products and S. F. Products, *Wood handbook: wood as an engineering material*, Forest Products Society, Madison, Wis., 2011.
123. K. M. Bryden, K. W. Ragland and C. J. Rutland, *Biomass & Bioenergy*, 2002, **22**, 41-53.
124. S. M. Ward and J. Braslaw, *Combustion and Flame*, 1985, **61**, 261-269.
125. H. Lu, in *Chemical Engineering*, Brigham Young University, 2006, p. 192.
126. K. O. Davidsson and J. B. C. Pettersson, *Fuel*, 2002, **81**, 263-270.
127. C. DiBlasi, *Chemical Engineering Science*, 1996, **51**, 1121-1132.
128. R. Vanholme, B. Demedts, K. Morreel, J. Ralph and W. Boerjan, *Plant Physiology*, 2010, **153**, 895-905.
129. M. G. Gronli and M. C. Melaaen, *Energy & Fuels*, 2000, **14**, 791-800.